論文 / 著書情報
Article / Book Information

題目(和文)	
Title(English)	New frameworks of high resolution schemes for Euler equations
著者(和文)	SunZiyao
Author(English)	Ziyao Sun
出典(和文)	学位:博士(理学), 学位授与機関:東京工業大学, 報告番号:甲第10429号, 授与年月日:2017年3月26日, 学位の種別:課程博士, 審査員:肖 鋒,青木 尊之,奥野 喜裕,末包 哲也,長﨑 孝夫
Citation(English)	Degree:Doctor (Science), Conferring organization: Tokyo Institute of Technology, Report number:甲第10429号, Conferred date:2017/3/26, Degree Type:Course doctor, Examiner:,,,,
学位種別(和文)	博士論文
Type(English)	Doctoral Thesis

TOKYO INSTITUTE OF TECHNOLOGY

DOCTORAL THESIS

New frameworks of high resolution schemes for Euler equations

Author:

Ziyao SUN

Supervisor:

Dr. Feng XIAO

A thesis submitted in partial fulfilment of the requirements

for the degree of Doctor of Science

in the

February 2017

Abstract

Godunov-type method has been well-accepted as the main-stream numerical approach to solve Euler equations. The reconstruction is the core issue for the development of the new numerical schemes. For existing Godunov-type methods, the numerical dissipation and numerical oscillations brought from reconstruction errors are two critical problems in the computation of Euler equations. In this thesis, we have made following efforts to solve the above problems.

1. We proposed a new guideline to construct high-resolution Godunov type schemes to resolve both smooth and discontinuous solutions. The basic idea, so-called BVD (boundary variation diminishing), is to reconstruct the solution functions so that the jumps at cell boundaries are minimized, which effectively reduces the numerical dissipation in the resulting schemes. We have implemented the BVD algorithm with the existing schemes as the building-block schemes, i.e. WENO (Weighted Essentially Non-Oscillatory) /TENO (Targeted Essentially Non-Oscillatory) and THINC (Tangent of Hyperbola INterface Capturing) schemes. Excellent numerical results have been obtained for both scalar and Euler conservation laws, which show a substantial improvement in comparison with the existing methods including the high-order and less-dissipative methods.

2. We developed a new WENO-type limiter for MCV3 (3-point Multi-moment Constrained finite Volume) scheme under MMC-FR (Multi-Moment Constrained Flux Reconstruction) framework. The new scheme, so-called MCV-WENO4 (MCV with WENO limiter of 4th order) scheme, distinguishes itself from the previous schemes by using the sub-grid information in the WENO reconstruction, which is better suited for the local high-order reconstruction schemes. Also, the present scheme has much less numerical dissipation, and thus doesn't use the ad hoc TVB (Total Variation Bounded) criterion needed in nearly all-existing schemes.

Furthermore, the present scheme is algorithmically simple and computationally efficient. The numerical results of the widely-used benchmark tests have verified that our scheme can get expected convergence rate and high quality solutions for both discontinuities and smooth profiles.

3. We devised a novel WENO limiter for CIP/MM FVM (Constrained Interpolation Profile/Multi-Moment Finite Volume Method), which leads to a new scheme, so-called CIP-CSL-WENO4 (Constrained Interpolation Profile-Conservative Semi-Lagrangian scheme with WENO limiter of 4th order). The new WENO limiter uses the local DOFs (Degrees of Freedom) available in the target cell and its immediate neighboring cells, which minimizes the WENO interpolation stencil. The proposed scheme is free of the ad hoc TVB criterion that is needed in nearly all-existing schemes to control excessive numerical dissipation. The semi-Lagrangian formulation is more accurate and of better computational efficiency in comparison with the Eulerian scheme. The numerical results indicate that our scheme is capable of resolving the sharp jump discontinuity while essentially eliminating numerical oscillations.

4. We proposed a new version of BVD algorithm that can use the HLR (High order numerical method with Local Reconstructions) as the building-block scheme. We extended the BVD concept to the difference of the derivatives at cell interfaces, where the reconstruction minimizes the BV of both PV and derivative values, which is compatible with the reconstructions in the multi-moment method and other HLR methods. We implemented the new BVD scheme using MCV-WENO4 scheme and THINC reconstruction as the building block schemes. The resulting scheme, BVD-MCV-WENO4 scheme, shows the possibility of implementing the BVD reconstruction under the HLR formulation. The numerical results demonstrate that the new BVD algorithm is capable of minimizing the numerical dissipation near the discontinuous solutions.

As mentioned above, the presented numerical formulations have been verified and validated by a wide range of benchmark tests, including analysis of errors and convergence rates as well as evaluation of robustness and computational cost. We have obtained expected numerical results for all the proposed schemes.

Acknowledgements

During the finish of this thesis, many people have given great help. Without them, I can hardly complete my Ph.d thesis. I always believe that it is important to have a thankful heart. That is my motivation for this acknowledgement. However, due to the limitation of the space, I can't thank them all here, but the names will always be kept in my heart.

Foremost, I want to give my special thanks to my advisor, Prof. Xiao. Without his help and instructions, I have no possibility to finish this thesis. Prof. Xiao is one of the most integrity and kindest persons I have met. His serious attitude towards the research has a great influence on me. His care for his students is sincere and without any selfishness. He takes the responsibility for not only the research of his students but also their future development. As a foreign student in Japan , I have received more than I can imagine from Prof. Xiao. He teaches me the rules of life in Japan with patients and provides me with the chance to meet some famous professors. The most important thing is that he has provided a good model for me to be an upright man. Thank Prof. Xiao again for his instructions.

Then, I want to thank my associate advisor, Prof. Aoki for providing me kind advice on my Ph.d research and my career plan. Because of the help from Prof. Aoki, I get the chance to join his seminar every week. The seminar of Prof. Aoki is very stimulating and inspired, and full with the novel ideas and fresh minds. I am glad that I have the chance to get the instructions directly from Prof. Aoki.

In addition, I want to thank Prof. Okuno, Prof. Nagasaki and Prof. Suekane to be the reader of my thesis. Prof. Suekane has helped me a lot in dealing with the troubles in my student life. He has also served as the instructor of the course "Fundamentals for Energy and Environment" where I have gained indispensible knowlegde for my Ph.d research. As the instructor of the course "Fundamentals for Energy Conversion", Prof. Okuno has taught me the essential knowledge about the energy conversion which I have

not learned in my undergraduate study. Prof. Nagasaki is my instructor of the course "Numerical Simulations for Fluid Dynamics", and his teachings provided me with the basic knowledge for the research of Computational Fluid Dynamics. Also, there are some others professors at Tokyo Institute of Technology giving me help and support. I express my sincere gratitude for them all.

Despite, I want to thank my labmates, Xie, Abe, Ikebata, Che, Deng, Inaba, Nakayama, Jin Peng, Jin Jonghoon, Wang, Tsubone, Kondo, Saito and Hashiguchi. During the finish of this thesis, they all provide me with kind supports on both the research and daily life. Especially, I express my gratitude for Dr. Xie. He helped me solve many problems in my research, and every time I have trouble with my program, I can get the solution from him. Also, I want to show my special thanks to Mr. Inaba. His work has made great contributions to the development of BVD scheme presented in this thesis.

Finally, I will say that without the support of my family, I can't finish my Ph.d thesis such smoothly. My father is very concerned about my study and my future career. When I feel depressed, he can always give me enough motivation. I strive to try my best in order not to disappoint him. My mother cares about my health more than anyone else. Under her suggestions, I start to workout everyday. She lets me know the importance of health. Because of his urge, I have transferred from an infirm boy to a quite strong man during my stay in Japan. Also, my grandfather and grandmother has supported me with their love and care. Thank my family again for their constant support.

Contents

List of Figures

List of Tables

Abbreviations

CFD	**C**omputation **F**luid **D**ynamics
FVM	**F**inite **V**olume **M**ethod
IVP	**I**nitial **V**alue **P**roblem
PDE	**P**artial **D**ifferential **E**quation
IC	**I**nitial **C**ondition
VIA	**V**olume-**I**ntegrated **A**verage
PV	**P**oint **V**alue
MUSCL	**M**onotonic **U**pstream-**C**entered **S**cheme for **C**onservation **L**aws
PPM	**P**iecewise **P**arabolic **M**ethod
ENO	**E**ssentially **N**on-**O**scillatory
WENO	**W**eighted **E**ssentially **N**on-**O**scillatory
DOF	**D**egree **O**f **F**reedom
RKDG	**R**unge-**K**utta **D**iscontinuous **G**alerkin
SV	**S**pectral **V**olume
SD	**S**pectral **D**ifference
FR	**F**lux **R**econstruction
CRP	**C**orrection **P**rocedure via **R**econstruction
HLL	**H**arten **L**ax van**L**eer
HLLC	**H**arten **L**ax van**L**eer **C**ontact
FCT	**F**lux-**C**orrected **T**ransport
TVD	**T**otal **V**ariation **D**iminishing

HLR	**H**igh order numerical method with **L**ocal **R**econstructions
DG	**D**iscontinuous **G**alerkin
SG	**S**taggered **G**rid
MCV	**M**ulti-moment **C**ontrained finite **V**olume
MMC-FR	**M**ulti-**M**oment **C**ontrained **F**lux **R**econstruction
CIP	**C**onstrained **I**nterpolation **P**rofile
CIP-CSL	**CIP**-**C**onservative **S**emi-**L**agrangian
IDO	**I**nterpolated **D**ifferential **O**perator
SLSI	**S**emi-**L**agrangian **S**emi-**I**mplicit
TV	**T**otal **V**ariation
TVB	**T**otal **V**ariation **B**ounded
HWENO	**H**ermite-type **WENO**
THINC	**T**angent of **H**yperbola for **IN**terface **C**apturing
VOF	**V**olume **O**f **F**luid
MTHINC	**M**ultidimensional **THINC**
BVD	**B**oundary **V**ariation **D**iminishing
MCV-WENO4	**M**ulti-moment **C**onstrained finite **V**olume with **WENO** limiter of **4**th order
CIP/MM FVM	**CIP**/**M**ulti-**M**oment **F**inite **V**olume **M**ethod
CIP-CSL3	**CIP-CSL** with **3**rd order polynomial function
MCV-SC	3-point **MCV** scheme with **S**lope **C**onstraint
CIP-CSL-WENO4	**CIP-CSL** with **WENO** limiter of **4**th order
BV	**B**oundary **V**ariation
TBV	**T**otal **B**oundary **V**ariation
END	**E**ffective **N**umerical **D**issipation
TENO5	**5**th order **T**argeted **ENO**
EOS	**E**quation **O**f **S**tate
SSP	**S**trong **S**tability **P**reserving
SSPRK	**SSP R**unge-**K**utta

MCV-SC4	**MCV-SC** of **4**th order
ODE	**O**rdinary **D**ifferential **E**quation
CFL	**C**ourant-**F**riedrich-**L**ewy

To my family

Chapter 1

Introduction

1.1 Background

Compressible flow is a kind of fluid which moves as Mach number is significantly larger than zero where the compressibility of the fluid can't be ignored. Compressible flow occurs in a wide spectrum of mechanical and aerospace engineering practices. The application of compressible flow mostly lies in design of high-speed aircraft, while in some devices such as gas turbine, stream turbine, reciprocating engine, natural gas transmission line and combustion chamber, the compressibility effect is so significant that the knowledge of compressible fluid flow is required [57].

To analysis the compressible flow, traditionally we can choose either theoretical or experimental approach [2]. However, for the theoretical approach, it can be virtually impossible to mathematically analyze the problem including both supersonic and subsonic area because of the change in mathematical behavior of governing equation [2]. About the experimental approach, normally the wind tunnel has limited functions that make the simulation of the conditions with both very high Mach number and high flow field temperature happened in transatmospheric vehicle impossible. Due to the above reasons, computational fluid dynamics (CFD) is needed as a growingly important tool to solve fluid mechanic problems in scientific research and engineering applications that

can't be solved by theoretical or experimental approach, especially for the ones including compressible flow [2]. CFD started with some pioneer works of Richardson around early 1900s, and has experienced a rapid growth with the advancement of computer technology since the middle of last century. After near one century of development, with high speed super computers and various of numerical methods, CFD has been so far widely used in compressible flow simulation.

The core issue of CFD is to devise reliable numerical algorithms with high efficiency. Recently, high-order numerical methods have been accepted as the favorable methods in fluid simulation [90]. Compared with low order methods (Second order or below), high order methods are more efficient in solving the physical problems with complicated structured regions [2]. For example, the simulation of delta wing vertical flows shows that high order accuracy schemes can yield better resolution of the vortices with lower grid resolution compared with low order schemes [22]. Exploring new numerical schemes of high accuracy and high efficiency is one of the current trends in CFD research. Our thesis mainly focuses on the development of novel high order numerical schemes in the compressible flow simulation. In the following sections, we introduce the current status of the development in high order numerical methods, along with the unsolved problems that we are going to tackle in this thesis.

1.2 Euler equations

The Euler equations are the system of non-linear hyperbolic conservation laws that govern the compressible flows without viscosity and heat transfer effect [84]. In compressible flow simulation, the key problem is to get proper numerical solutions to the Euler equations because of the complexity in the numerical computation of Euler equations.

The 1D Euler equations for ideal gas are given by

$$\mathbf{U}_t + \mathbf{F}(\mathbf{U})_x = 0, \tag{1.1}$$

where

$$\mathbf{U} = \begin{pmatrix} u^{(1)} \\ u^{(2)} \\ u^{(3)} \end{pmatrix} = \begin{pmatrix} \rho \\ \rho v \\ E \end{pmatrix}, \quad \mathbf{F}(\mathbf{U}) = \begin{pmatrix} f^{(1)} \\ f^{(2)} \\ f^{(3)} \end{pmatrix} = \begin{pmatrix} \rho v \\ \rho v^2 + p \\ v(E+p) \end{pmatrix}. \tag{1.2}$$

Here ρ is density, v velocity, p pressure and E total energy. We use the equation of state (EOS) of ideal gas, i.e.

$$E = \frac{p}{\gamma - 1} + \frac{1}{2}\rho v^2, \tag{1.3}$$

where $\gamma = 1.4$. Due to the hyperbolic characteristic of Euler equations, the interaction between the characteristic lines generates shock waves, which are the small transition layers of very rapid changes of physical quantities such as pressure, density and temperature. Mostly, the width of shock wave is the same order of mean-free path of the molecules, which is about 10^{-7} m. This property makes the simulation of shock wave an difficult task, therefore it is important to find the mathematical replacement for these waves. Despite, wave-steepening and rarefaction wave is other distinguished features for hyperbolic systems like Euler equations, which adds difficulties to the numerical simulation of Euler equations.

The Euler equations with the ideal-gas EOS satisfy the homogeneity property. Thus it can be quasi-linearized into the following form [84]

$$\mathbf{U}_t + \mathbf{A}(\mathbf{U})\mathbf{U}_x = 0, \tag{1.4}$$

where $\mathbf{A}(\mathbf{U})$ is the Jacobian matrix whose eigenvalues are the characteristic speed of the Euler equations. The definition of $\mathbf{A}(\mathbf{U})$ is given in the Appendix B.

1.3 Godunov-type method

The high-resolution shock capturing schemes, which are now well-accepted as the main-stream numerical approach to solve Euler equations for compressible gas dynamics, can trace back to Godunov's scheme [25]. The original Godunov scheme is a conservative finite-volume method (FVM) with piece-wise constant reconstruction, and the fluxes at the cell boundaries are computed by solving the exact Riemann problem from the piece-wise constant reconstruction of the physical fields in two neighboring cells, which usually results in a jump at the cell boundaries. In general, Godunov schemes are consist of two essential steps in solution procedure, i.e. (I) reconstruct the physical fields to find the values at the left- and right- sides of cell boundaries, and (II) evaluate the numerical fluxes at cell boundaries that are needed in the FVM formulation to update the cell-integrated values to next time step. We introduce these two parts separately in the following subsections.

1.3.1 Reconstruction

Firstly, we consider the initial value problem (IVP) that consists of a partial differential equation (PDE) together with the initial condition (IC) as follows

$$\begin{cases} PDEs : \mathbf{U}_t + \mathbf{F}_x = 0, -\infty < x < \infty, t > 0 \\ IC : \mathbf{U}(x,0) = \mathbf{U}_0(x). \end{cases} \tag{1.5}$$

The spatial domain $[a,b]$ is discretized into N control volumes or finite volume as $I_i = [x_{i-\frac{1}{2}}, x_{i+\frac{1}{2}}], i = 1,2,\ldots,N$ and the size of each cell Δx_i is give by $\Delta x_i = x_{i+\frac{1}{2}} - x_{i-\frac{1}{2}} = \frac{b-a}{N}$. Inside each cell, we define the volume integrated average (VIA) of the control volume as

$$\bar{\mathbf{U}}_i^n = \frac{1}{\Delta x_i} \int_{x_{i-\frac{1}{2}}}^{x_{i+\frac{1}{2}}} \mathbf{U}(x,t^n) dx \tag{1.6}$$

Thus, we have the piecewise constant distribution of solution at $t = t^n$ spanning the whole computational domain. Integrating the PDE in (1.5) over x in cell $I_i =$

$[x_{i-\frac{1}{2}}, x_{i+\frac{1}{2}}]$ gives

$$\frac{d\bar{\mathbf{U}}_i}{dt} = -\frac{(\tilde{f}(\mathbf{U}_{i+\frac{1}{2}}) - \tilde{f}(\mathbf{U}_{i-\frac{1}{2}}))}{\Delta x}. \tag{1.7}$$

and further we integrate above equation over time from $t = t^n$ to $t = t^{n+1}$, which gives the finite volume formulation for conservation law as

$$\bar{\mathbf{U}}_i^{n+1} = \bar{\mathbf{U}}_i^n - \frac{\Delta t}{\Delta x}(\tilde{f}(\mathbf{U}_{i+\frac{1}{2}}) - \tilde{f}(\mathbf{U}_{i-\frac{1}{2}})). \tag{1.8}$$

It shows that the piece-wise constant can be updated to next time step by using the numerical fluxes calculated at cell boundary. For original Godunov method, the point value (PV) at the cell interface is reconstructed using the piece-wise constant value, i.e.

$$\mathbf{U}^-_{i+\frac{1}{2}} = \bar{\mathbf{U}}_i,\ \mathbf{U}^+_{i+\frac{1}{2}} = \bar{\mathbf{U}}_{i+1}. \tag{1.9}$$

which assumes a discontinuity at the cell boundary. The interaction between adjacent cells can be resolved by solving the Riemann problem exactly or approximately at each cell interface. Some successive works of Godunov-type method still follow this manner by assuming the discontinuity at cell boundary, while Riemann problem is solved along each cell interface to guarantee the upwind property of wave propagation. However, the reconstruction is not limited to the piece-wise constant but extended to higher order reconstructions such as monotonic upstream-centered scheme for conservation laws (MUSCL) [87, 88] of linear reconstruction, piecewise parabolic method (PPM) [18] of parabolic reconstruction, essentially non-oscillatory (ENO) [23, 31, 73, 74] as well as weighted essentially non-oscillatory (WENO) [45, 53, 72] scheme of 5th order or higher reconstruction. Apart from the single degree of freedom (DOF) method (namely the traditional FVM formulation), the reconstruction can also be conducted locally by using multi-moments inside each cell, such as Runge-Kutta Discontinuous Galerkin (RKDG) method [13–15, 17], spectral volume (SV) [89, 92, 93] /difference (SD) method [90] and flux econstruction (FR) [37–39]/ correction procedure via reconstruction (CPR) method [91].

1.3.2 Riemann solver

As mentioned above, to obtain the numerical flux at the cell boundary, the following Riemann problem needs to be solved

$$\begin{aligned} &PDE : \mathbf{U}_t + \mathbf{A}\mathbf{U}_x = 0,\ -\infty < x < \infty,\ t > 0 \\ &IC : \mathbf{U}(x,0) = \begin{cases} \mathbf{U}_L,\ x < 0, \\ \mathbf{U}_R,\ x > 0. \end{cases} \end{aligned} \tag{1.10}$$

For scalar conservation law, it is trivial to get the solution of above Riemann problem by simply selecting the upwind side according to the wave speed at the cell boundary. For example, the numerical flux for advection equation $u_t + au_x = 0$ can be written as

$$\hat{f}_{i+\frac{1}{2}} = \frac{1}{2}\left(f(u^L_{i+\frac{1}{2}}) + f(u^R_{i+\frac{1}{2}})\right) - \frac{1}{2}|a_{i+\frac{1}{2}}|\left(u^R_{i+\frac{1}{2}} - u^L_{i+\frac{1}{2}}\right) \tag{1.11}$$

The first term of the right hand side represents the central difference while the second term represents the numerical dissipation that is essential for yielding the upwind property. We can see that the magnitude of the numerical dissipation term is connected with the difference of the PV reconstructed from left and right side of the cell boundary.

For Euler equations, the original Godunov scheme uses exact solutions of Riemann problem to acquire the numerical flux, which is usually time consuming. Several approximated Riemann solvers are presented in the literature to reduce the computational cost. Some widely used approximate Riemann solvers include the Roe's Riemann solver, Osher's Riemann solver, Harten, Lax and Van Leer (HLL)-type Riemann solver [84] and Constact HLL (HLLC) developed by Toro *et al* [84].

It should be noticed here that even though Riemann solver is an essential part for Godunov-type method to resolve the interaction between neighboring cells, the reconstruction is still the core problem for the development of new numerical schemes, for it can fundamentally influence the numerical property of the resulting scheme. As a consequence, we focus on the reconstruction part and investigate several possibilities in the development of new numerical scheme in this thesis.

1.3.3 Conventional finite volume method (FVM)

In FVM, the computational domain is discretized into several non-overlapping control volumes, and the construction of FV scheme is based on the cell-averaged value of each control volume. Just as mentioned in the previous section, Godunov-type method with single DOF for each cell is actually equivalent to FVM.

The great advantage of FVM is that conservative discretization is automatically satisfied because of the direct discretization of the integral form of the conservation laws. Despite, FVM is easy to be implemented to arbitrary meshes, where several options are open for the definition of control volume. In fact, FVM is the most widely used method in CFD society. The original Godunov method introduced in the previous section is belonging to FVM.

Instead of the piece-wise constant approximation which leads to a first-order scheme, higher order polynomials have been used to improve the accuracy (convergence rate for smooth solution). In order to get around the so-called Godunov barrier for linear schemes which states that any monotonic linear scheme can be of only first order, non-linear numerical dissipation has been introduced to high-order schemes to suppress the spurious oscillations in the vicinity of discontinuities. The non-linear numerical dissipation has been devised in different forms seen in the literature as either flux limiters in flux-corrected transport (FCT) scheme [7, 111] and total variation diminishing (TVD) scheme [30, 81] or the slope limiters in MUSCL scheme [87, 88]. The later gives a more straightforward interpretation of the polynomial-based reconstruction for high-order schemes, and shows a clear path to design high-resolution schemes using modified high-order polynomials. Representative schemes of this kind are PPM method [18], ENO [23, 31, 73, 74] and WENO scheme [45, 53, 72]. WENO concept provides a general framework to develop high-resolution schemes that are able to reach the highest possible order of accuracy over a given mesh stencil for smooth solution, and effectively stablize the numerical solutions which include discontinuities. Successive works on WENO scheme are found in designing better smoothness indicators and non-linear weights [5, 6, 32, 35, 70] to improve solution quality, as well as implementing the WENO concept to different discretization framework [19, 54, 59, 66].

Starting from the piecewise constant approximation in the original Godunov scheme, the development of the high-order shock capturing schemes have evidenced a history of the efforts to reduce the difference between the reconstructed left- and right-side values for smooth solutions. This observation, however to our knowledge, has not been paid enough attention, nor explored further as a prospective guideline to construct new schemes.

1.3.4 High order numerical method with local reconstructions (HLR)

It has been a trend for the past decades in the field of CFD to make use of locally (cell-wisely) increased DOFs to construct high-order schemes. The major advantages of a scheme using loca recontructions lie in the spectral-like convergence rate and the adaptivity to unstructured grids. It has been proved in [90] that p-refinement (polynomial refinement) produces a variable convergence rate, which is increased with number of DOFs, while the h-refinement (the mesh size refinement) only produces a constant rate of convergence rate. Clearly that the variable convergence rate which increases exponentially is much faster than the algebraic convergence rate, which means the local increase of DOFs can help reduce the numerical errors. Some representative methods of this sort for CFD applications are spectral element method [58], discontinuous Galerkin (DG) method [12, 15–17, 33, 48, 65], constrained interpolation profile (CIP) method [106, 108], staggered-grid (SG) Chebyshev multidomain method [47], spectral volume (SV) method [89, 92], spectral difference (SD) method [90] and multi-moment (constrained) finite volume (MV or MCV) method [10, 40, 41, 103, 104].

Although apparent differences are seen among the aforementioned methods in the details of reconstruction and solution procedures, all of them realize high-order accuracy via locally reconstructed polynomials and guarantee the numerical conservation by introducing an FVM-like constraint condition on the continuity of the numerical fluxes across cell boundaries, while the numerical fluxes are computed through exact or approximated Riemann solvers. From this observation, a general framework for constructing high-order spectral-convergent schemes, so-called flux reconstruction (FR) method, was proposed in [37–39]. FR formulation treats the point values as the computational

variables at the solution points located within each cell, which facilitates local reconstructions of high order. An FR scheme computes the point-wise solution via the differential form of the governing equation, and the flux function must be reconstructed so as to satisfy the continuity on the cell boundaries. As shown in [37], nearly all existing nodal-value based high order schemes can be interpreted as the subset cases of FR framework where the correction functions involved in the flux reconstruction procedure makes the difference among the schemes. FR method was extended to unstructured grids under the name of CPR (correction procedure via reconstruction) [91].

We show in the multi-moment constrained flux reconstruction (MMC-FR) method [102] that the flux function can be reconstructed more flexibly with a wider variety of constraint conditions. We demonstrate that stable and more efficient schemes can be devised by making use of not only the point values but also the derivatives of different orders at different constraint points. The class of MCV schemes [41] can be devised straightforwardly from various constraint conditions under the MMC-FR framework.

An alternative way to increase the local DOFs was introduced in the constrained interpolation profile (CIP) scheme [106, 108], where two types of moments, i.e. the point values (PVs) and the first-order derivatives, are simultaneously treated as the model variables and separately updated in time. The successive studies include the interpolated differential operator (IDO) scheme developed by Aoki [3] which is also based on multi-moments reconstruction but using the Eulerian method instead of semi-Lagrangian method in updating the moments. A series of conservative CIP schemes, called CIP-conservative semi-Lagrangian (CIP-CSL) schemes, was presented in [83, 96, 99, 107] for scalar conservation laws. In CIP-CSL schemes, volume integrated average (VIA) is treated as a new model variable that is updated in the same manner as the traditional FVM, thus the scheme has exact numerical conservativeness. In line with the IDO scheme mentioned above, a conservative version of IDO scheme was also devised in [43]. CIP-CSL scheme has been used to solve the global shallow water equations in [50] under the semi-Lagrangian semi-implicit (SLSI) framework, among other implementations of the conservative semi-Lagrangian schemes in geophysical fluid modeling [24, 29, 52, 86]. In the SLSI framework, the advection is solved separately from the geopotential gradient forcing (or equivalently the acoustic effect in gas dynamics). The

later is computed by implicitly solving a Helmholtz equation for geopotential or pressure. To our knowledge, implementation of the semi-Lagrangian schemes to hyperbolic systems with the complete characteristic theory has not been adequately explored.

Despite the superiority of HLR method in resolving complex structures of smoothness, numerical oscillation associated with discontinuity turns out to be an important problem. Using some special interpolation functions, such as the rational function in [97–99], proves to be effective in suppressing numerical oscillations. Being a more general approach, nonlinear limiting projection can be used to prevent the spurious oscillations in the presence of discontinuities or large jumps. In the next section, we will give a deep discussion about the widely used methods for limiting projection.

1.4 Limiting projection

For the HLR schemes, the significant oscillations or even non-linear instabilities are generated when dealing with the problems with strong discontinuities because of the Gibbs phenomena. To handle the problem, flux limiter is one of the widely used approaches that has been successfully implemented in several high resolution schemes to avoid the numerical oscillations. The flux limiter can automatically detect the oscillation in the simulation procedure and thoroughly eliminate the oscillations .

1.4.1 TVD/TVB type limiter

One of the popular flux limiter is the Total Variation Diminishing (TVD) Limiter [30, 33, 84]. To introduce the TVD limiter, we firstly give the definition of the Total Variation (TV) [30] of the function $u(x,t)$ at fixed time $t = t^n$, as

$$TV(u^n) = \sum_{i=-\infty}^{\infty} |u_{i+1}^n - u_i^n|, \tag{1.12}$$

and the scheme is of TVD property if

$$TV(u^{n+1}) \leqslant TV(u^n),\ \forall n. \tag{1.13}$$

So a flux limiter is called TVD limiter if the limiter that can guarantee TVD property of the numerical scheme. There are several limiters belonging to TVD limiters, including min-mod limiter [68], superbee limiter [68] and Van-Leer's MUSCL limiter [88]. For TVD limiter, the numerical scheme can reduce to a monotone scheme at the area where the oscillation appears, which is identified by the flux limiter function depending on the smoothness of the solution. Because of the TVD property, TVD limiter can essentially suppress the oscillation. There is another limiter called Total Variation Bounded (TVB) limiter [71] that can control the increase of the TV, which is possible to achieve higher order of accuracy than TVD limiter. The definition of the TVB is that: the scheme is of TVB property in $0 \leqslant t \leqslant T$ if

$$TV(u^n) \leqslant B,\ \forall n, \tag{1.14}$$

where $B > 0$ is a fixed value depending only on $TV(u^0)$ and all possible n and Δt such that $n\Delta t \leqslant T$.

However, both TVD and TVB limiter can only achieve as high as third order accuracy. For schemes with more than 3rd order of accuracy, the use of TVD/TVB flux limiter destroy the expected convergence rate.

In order to eliminate the oscillation as well as keep the high order of accuracy, the WENO limiter is proposed by borrowing the idea of WENO method. As the WENO method is possible to achieve arbitrary order of accuracy, it is not hard for WENO limiter to keep the original accuracy of the high order scheme. In addition, compared with TVD/TVB limiter, WENO limiter is more robust, especially for high order schemes. In the next subsection, we will take a brief introduction of WENO limiter.

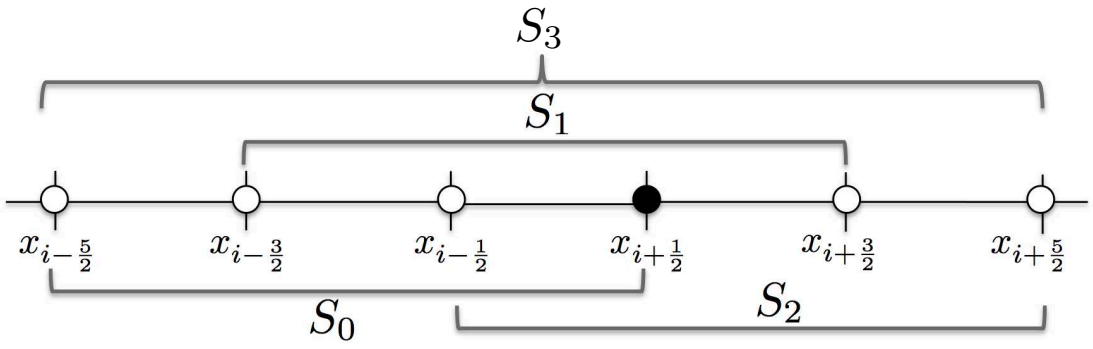

FIGURE 1.1: The calculation stencil for 5th order finite-volume WENO scheme

1.4.2 WENO limiter

WENO limiter is based on the idea of WENO scheme [34, 44–46, 53, 72]. So firstly we show the basic idea of WENO scheme. The WENO scheme stems from the ENO method developed by Harten *et al* in 1987 [31, 73]. The basic idea of ENO is to devise a mechanism to automatically choose the locally smoothest stencils that can avoid crossing discontinuities stencil as much as possible. In 1994, Liu *et al* [53] firstly proposed WENO by replacing the smoothest stencil of ENO by a convex combination of reconstructions from all candidate stencils. In 1996, Jiang and Shu [45] provided a general framework to achieve arbitrary accurate order finite difference WENO scheme, which makes WENO method popular. Generally the fifth order finite volume WENO scheme is the most widely used version of WENO scheme. For the convenience of understanding, we will give a brief introduction of $5th$ order WENO construction.

1.4.2.1 WENO reconstruction

The basic idea of WENO scheme is to choose the smoothest function from three candidate stencils. The division of the stencil is shown in Fig. 1.1. We have three sub stencils S_0, S_1, S_2, and one large stencil S_3. Then we can construct the solution functions by using the VIAs of each cell inside three sub stencils S_0, S_1, S_2 and approximate the PV at the $x_{i+\frac{1}{2}}$ with $3rd$ order accuracy. The solution function of each stencil can be recovered from the following conditions

$$\bar{u}_{i+j+k-2} = \frac{1}{\Delta x_{i+j+k-2}} \int_{x_{i+j+k-\frac{5}{2}}}^{x_{i+j+k-\frac{3}{2}}} u^{(j)}(x)dx, j = 0, 1, 2, k = 0, 1, 2, \tag{1.15}$$

where $\Delta x_{i+j+k-2}$ is the mesh size. For simplicity, we assume a uniform grid spacing, i.e. $\Delta x_{j-i} = x_{i+j+k-\frac{5}{2}} - x_{i+j+k-\frac{3}{2}} = \Delta x$. Thus the third order approximation of $u_{i+\frac{1}{2}}$ is given respectively from solution function $u^{(j)}(x), j = 0, 1, 2$ as

$$u^{(0)}_{i+\frac{1}{2}} = \frac{1}{3}\bar{u}_{i-2} - \frac{7}{6}\bar{u}_{i-1} + \frac{11}{6}\bar{u}_i, \tag{1.16a}$$

$$u^{(1)}_{i+\frac{1}{2}} = -\frac{1}{6}\bar{u}_{i-1} + \frac{5}{6}\bar{u}_i + \frac{1}{3}\bar{u}_{i+1}, \tag{1.16b}$$

$$u^{(2)}_{i+\frac{1}{2}} = \frac{1}{3}\bar{u}_i + \frac{5}{6}\bar{u}_{i+1} - \frac{1}{6}\bar{u}_{i+2}, \tag{1.16c}$$

where $u^{(j)}_{i+\frac{1}{2}}$ is the abbreviation of $u^{(j)}(x_{i+\frac{1}{2}})$. Similarly, we can construct a $4th$ degree polynomial using VIAs in large stencil S_3 , and retrieve the PV at the $x_{i+\frac{1}{2}}$ with fifth order accuracy, by

$$u^{(3)}_{i+\frac{1}{2}} = \frac{1}{30}\bar{u}_{i-2} - \frac{13}{60}\bar{u}_{i-1} + \frac{47}{60}\bar{u}_i + \frac{9}{20}\bar{u}_{i+1} - \frac{1}{20}\bar{u}_{i+2}. \tag{1.17}$$

Then we find that the fifth order approximation can be written through a convex combination of the three third order approximation (1.16a),(1.16b) and (1.16c),namely

$$u^{(3)}_{i+\frac{1}{2}} = \gamma_0 u^{(0)}_{i+\frac{1}{2}} + \gamma_1 u^{(1)}_{i+\frac{1}{2}} + \gamma_2 u^{(2)}_{i+\frac{1}{2}}, \tag{1.18}$$

where $\{\gamma_0, \gamma_1, \gamma_2\} = \left\{\frac{1}{10}, \frac{3}{5}, \frac{3}{10}\right\}$. In order to eliminate the oscillation at the discontinuities, we should replace the coefficient γ_0, γ_1, γ_2 by the weighted parameter ω_0, ω_1, ω_2, which should meet the following conditions:

1. $\omega_1 + \omega_0 + \omega_2 = 1$,

2. $\omega_j,\ j = 0, 1, 2$ should be close to zero for a non-smooth stencil and close to one for a smooth stencil.

To achieve the above properties, Jiang and Shu [45] introduced a measurement for smoothness in each sub-stencil, so-called smoothness indicator, defined by

$$\beta_j = \sum_{l=1}^{2} \int_{x_{i-\frac{1}{2}}}^{x_{i+\frac{1}{2}}} (\Delta x)^2 \left[\frac{\partial^l u^j(x)}{\partial x^l}\right]^2 dx, \quad j = 0, 1, 2. \tag{1.19}$$

Having the smoothness indicator, the weighted parameters are given by

$$\omega_j^{JS} = \frac{\alpha_j}{\alpha_0 + \alpha_1 + \alpha_2}, \quad \alpha_j = \frac{\gamma_j}{(\epsilon + \beta_j)^2}, \quad j = 0, 1, 2. \tag{1.20}$$

Here ω_j^{JS} means the modified weighted parameters derived by the smoothness indicator of Jiang and Shu [45], and ϵ is a small number that is used to avoid the condition that the denominator equals to zero. In Jiang and Shu's paper, ϵ is recommended to be equal to 10^{-6}.

Regarding the WENO reconstruction, some successive works have been conducted to improve the accuracy of the classic WENO [45] by using different nonlinear weights and smoothness measurements in the WENO reconstruction, such as WENO-M [32] and WENO-Z [6] scheme. Shen and Zha [69, 70] provided a careful analysis about how these scheme behaves over a transition cell where smooth region and discontinuity connects, and proposed the optimal estimation of the first-order derivative for the transition cell.

1.4.2.2 Development of WENO limiter

The WENO limiter was designed originally for finite volume and finite difference methods [72] and implemented to DG method in [64], where the fifth order WENO scheme of FVM type was constructed by using the cell average values over a wide stencil. The WENO reconstruction is then used to project the point values (PVs) at the Gauss quadrature points in the target cell. This formulation only uses the cell averages even though more information (DOFs) are available in the local reconstructions of DG. An effort was made by the same authors to use more local information from the cell-wise high-order polynomial by devising a Hermite-type WENO limiter (HWENO) [61, 63], which uses the derivatives as another moment in the reconstruction and looks better suited for the local reconstructions used in DG, and thus makes the stencil more compact. But still, the information inside each cell has not been fully used in WENO reconstruction. For example, the fourth order DG scheme has three DOFs in each cell, while HWENO can only use as much as two DOFs. Also, as the WENO methodology already includes a

smoothness indicator that can detect the smoothness of the flux function, the "trouble cell" indicator seems to be unnecessary if a proper WENO limiter is designed.

Among other successive works, a more general formulation that maps different moments to cell averages or point values for making use of the conventional WENO reconstructions is developed in [36]. Recently, a simple WENO limiter has been proposed in [112] for DG and applied to FR/CPR in [20]. This scheme minimizes the stencil for WENO reconstruction and only uses the target cell and its immediate neighbors.

1.5 Tangent of Hyperbola for INterface Capturing (THINC) reconstruction

Being a sigmoid function, hyperbolic tangent function is a differentiable and monotone function that fits well a step-like discontinuity. A class of VOF (volume of fluid) schemes, so-called THINC, has been devised to compute moving interfaces in multiphase flow simulations. The original THINC scheme is used as an algebraic reconstruction for VOF method to remedy the deficiencies of traditional geometrical type method such as strong numerical dissipation and complex coding process. Some development of THINC can be found in [42, 110] to improve the multi-dimensional solutions when using 1D solver as building-block scheme. These THINC schemes are very simple and can be used as normal advection schemes. In spite of the simplicity, these schemes can obtain high-quality numerical solutions comparable to the conventional geometrical VOF methods in multi-phase flow calculation. By using a continuous analytical function, a THINC scheme can reconstruct the interface uniquely with high resolution from given volume fraction values. A sophisticated version of THINC scheme, so-called MTHINC (multidimensional THINC) method [42], has been proposed by using a multidimensional hyperbolic tangent function for reconstruction, which significantly improves the numerical accuracy due to the multi-dimensional reconstruction.

1.6 Unresolved problems

The Godunov-type method has been widely used in the simulation of Euler equations. For Euler equations, the existence of shock wave can make the simulation difficult due to the strong discontinuity. Among the existing Godunov-type methods, the following problems have been noticed.

1. The excessive numerical dissipation is a significant problem for FVM of Godunov-type method. The traditional FVM always assumes a jump at the cell boundary in reconstruction procedure which is remedied by solving the Riemann problem along each cell interface exactly or approximately. To some extent, the development of FVM is the effort to minimize the reconstruction difference at cell interfaces for smooth solutions by using high order polynomial reconstruction. However, this can be problematic when the solutions include discontinuities, which will be discussed in detail in the next chapter. Anyway, the conventional high order polynomial can not reduce the reconstruction difference with the increase of the polynomial order, thus it is not suitable to reconstruct the discontinous solutions. As shown in (1.11), the reconstruction difference at the cell interface is connected with the magnitude of numerical dissipation term. As a results, in order to reduce the numerical dissipation near the discontinuous area, we need find a new way to build up the FVM.

2. For HLR method, numerical oscillation is an inevitable problem. Even though several strategies of limiting projection have been proposed in the literature, most of the existing methods simply follow the flux limiter of FVM without considering the local DOFs defined inside each cell element. Thus, the traditional limiting projections such as WENO limiter for DG destroy the geometry flexibility of locally reconstructed methods. Due to the above reasons, we want to find a new flux limiter based on WENO methodology that can fully take advantage of locally defined DOFs.

1.7 Purposes of current study

In this paper, we want to explore the new formulation of the numerical scheme to solve Euler equations based on Godunov-type method. For Euler equations, the strategy in dealing with the discontinuity is important to the quality of the numerical solutions due to the existence of shock wave. Based on the existing problems discussed in the previous section, we give the purposes of our study from the following two parts.

1. Firstly, we hope to propose a new guideline to design high-resolution schemes that can reduce the excessive numerical dissipation error existing in traditional FVM. The target numerical method should be consistent with the observation gained for smooth solutions that the development of high-order shock capturing schemes is in reality an effort to reduce the reconstructed difference at cell interfaces. Thus, we come up with the following principle

   (a) The reconstruction of the new method should be based on the principle that the reconstructed jump at the cell interface can be minimized;

   (b) The new method needs to automatically realize the highest possible order of polynomial interpolation for the smooth profile;

   (c) More importantly, it can recover the discontinuous solutions with high accuracy by using the reconstruction that is of better monotonicity.

   In other words, we want to develop a switch procedure between a high order polynomial reconstruction and a low order reconstruction that can better represent the discontinuity on the basis of minimization of the reconstructed difference at the cell interfaces. The switch procedure should be reliable that it can reconstruct the solution function for both smooth profile and discontinuity with high resolution.

   Based on the above requirements, we develop the boundary variation diminishing (BVD) reconstruction in this thesis that can efficiently mitigate the reconstructed discontinuities appeared at the cell interfaces. We want that our the new guideline can be applied to both FVM and HLR method.

2. Furthermore, in order to deal with the numerical oscillations of HLR method, we want to present a better-matched WENO limiter for MMC-FR scheme. The new WENO limiter should fullfill the following properties.

   (a) The new WENO limiter must be able to eliminate the oscillation at the discontinuity, which is the basic requirement for the WENO limiter;

   (b) The new WENO limiter should be able to recover the original order of accuracy of MMC- FR scheme;

   (c) The new WEON limiter is better to use the PVs instead of the VIAs in the WENO construction so that the size of the reconstruction stencil can be reduced, which preserves the locality of the MMC-FR scheme and realizes the geometrical flexibility;

   (d) The "trouble cell" indicator [62] used in traditional WENO limiter is needless under the WENO methodology. So the new WENO limiter should be a "trouble cell" indicator free limiter which doesn't generate excessive dissipation at the discontinuities.

   In this thesis, we present a new WENO limiter to MCV3 scheme of MMC-R formulation. The resulting scheme, MCV-WENO4 (Multi-moment Constrained finite Volume with WENO limiter of 4th order) method meets all the above requirements.

   We also extend the new WENO limiter to CIP multi-moment finite volume method (CIP/MM FVM) of semi-Lagrangian to solve the Euler conservation laws by implementing the characteristic theory. The new WENO limiter will be built on the CIP-CSL scheme [40], while the reconstruction of the WENO limiter should use the PVs within mesh elements instead of the cell VIAs. Also, the new scheme should be less dissipative so that it can be free of the TVB criterion that was originally used to control the superfluous numerical dissipation for traditional WENO limiter.

   Finally, we apply the BVD reconstruction to the MCV-WENO4 scheme as a practice to introduce the BVD algorithm in HLR-type method. As the reconstruction of MCV method requires the continuity of not only the PV but also the first order

derivative, the BVD reconstruction should also include the derivative values in the build-up of the scheme.

1.8 Outline of thesis

The remainder of this thesis is arranged as follows. In Chapter 2, we introduce our original BVD scheme. Initially, we discuss the influence of boundary variation for the characteristic of high order FVM, to induce the fundamental idea of our BVD method. Then, an instance of BVD scheme by using the WENO/ Targeted ENO (TENO) presented in this chapter. A gross analysis of the computational efficiency of BVD method is also discussed. Finally, we show the numerical solutions for both scalar conservation law and Euler equations computed using BVD scheme.

In Chapter 3, the problem of the existence of numerical oscillations near the discontinuities for HLR method is introduced. Then we take a brief review of MMC-FR construction. As the 4th order WENO limiter is performed on the 3-point MCV scheme with slope constraint (MCV-SC) scheme, the reconstruction procedure of the MCV-SC scheme is given in detail aforehand. Then we propose the construction of the MCV-SC scheme using the WENO limiting (we call the resulting scheme MCV-WENO4 scheme) in scalar conservation law. In this part, the stencil discretization, the polynomial interpolation and the WENO reconstruction in the MCV-WENO4 scheme is introduced separately. In addition, the issue on applying the MCV-WENO4 scheme to Euler equations is discussed. Also, the computational cost of WENO limiter is analyzed. Finally, the numerical results of the widely used benchmark tests in one and two dimensions are given to verify the proposed scheme.

In Chapter 4, the CIP-CSL3 scheme is reviewed under the formulation of CIP/MM FVM, including the implementation to scalar conservation law as well as the Euler equations. Then, we describe the application of the 4th order nodal-value based WENO limiter to CIP-CSL3 method, where the resulting scheme is called CIP-conservative Semi-Lagrangian with WENO limiter of 4th order (CIP-CSL-WENO4) scheme. The comparison between the Eulerian and semi-Lagrangian schemes based on the error

measurements are given in this chapter, which demonstrates the superiority of the semi-Lagrangian scheme. In the end, the numerical results of some widely-used benchmark tests are presented to verify the accuracy and robustness of the proposed scheme.

In Chapter 5, we present a new version of BVD reconstruction that is suitable for HLR method. The new BVD algorithm includes the derivative values in the selection procedure, which is compatible with the multi-moment reconstruction of HLR method. Based on the new BVD concept, we present a new scheme named BVD-MCV-WENO4 scheme that uses MCV-WENO4 scheme and a THINC-implemented MCV reconstruction as the building-blocks for BVD reconstruction. Finally, some numerical experiments are done for BVD-MCV-WENO4 scheme to validate the effectiveness of our new BVD method.

In Chapter 6, we review the previous chapters to provide a full picture of this thesis. The major contributions of the current study are introduced along with the future works extended from this thesis.

Chapter 2

Boundary Variation Diminishing (BVD) reconstruction: a new approach to improve Godunov schemes

2.1 The problem of existing high order finite volume method

As mentioned in the previous chapter, the discontinuity is always assumed at the cell boundary, where the L_0 continuity is realized by solving the Riemann problem at each interface. The discontinuity is caused by the biased stencil used in the reconstruction of flux at cell boundary. The numerical flux at cell boundary can be given in the following formulation for 1D advection equation $u_t + au_x = 0$, a is constant

$$\hat{f}_{i+\frac{1}{2}} = \frac{1}{2}\left(f(u^L_{i+\frac{1}{2}}) + f(u^R_{i+\frac{1}{2}})\right) - \frac{1}{2}|a_{i+\frac{1}{2}}|\left(u^R_{i+\frac{1}{2}} - u^L_{i+\frac{1}{2}}\right) \tag{2.1}$$

Actually the numerical flux is a combination of central scheme $\frac{1}{2}\left(f(u^L_{i+\frac{1}{2}}) + f(u^R_{i+\frac{1}{2}})\right)$ and numerical dissipation term $\frac{1}{2}|a_{i+\frac{1}{2}}|\left(u^R_{i+\frac{1}{2}} - u^L_{i+\frac{1}{2}}\right)$. As the wave velocity a is constant, the value of numerical dissipation term is mainly influenced by the reconstructed

difference at the cell interface. The upwind property of hyperbolic equation is represented by the numerical dissipation term, so the scheme will become unstable if the numerical dissipation term is omitted. However, the excessive numerical dissipation will generate very dissipative numerical solutions. In this case, some weak discontinuities such as the contact discontinuity of Euler equations will be strongly dissipated, sometimes even vanish. Too much numerical dissipation can leave the numerical solutions inaccurate, especially in simulation of compressible flow with multi-interaction of discontinuities. Thus, even though the numerical dissipation is indispensable in solving the hyperbolic system, it is still necessary to reduce the numerical dissipation as much as possible.

Here, we give a new definition, boundary variation (BV) as

$$BV(u)_{i+\frac{1}{2}} = |u^R_{i+\frac{1}{2}} - u^L_{i+\frac{1}{2}}|, \tag{2.2}$$

which can measure the quantity of the numerical dissipation. From the history of the FVM introduced in tbe previous chapter, we can see that the development of FVM is a history to reduce the BV. People try to use as high order polynomial as possible in the innovation of FVM. By using higher order polynomial in the numerical reconstruction, the BV can be significantly reduced for smooth solutions. This can be grossly verified from the test in Fig. 2.1(b). Here, the profile is distributed following the sine wave, a very smooth profile. The BV at the boundary plotted by green line is calculated by growing order of polynomial. It can be seen from the Fig. 2.1(a), that with the increase of polynomial order, the BV is consistently reduced. But is it true for discontinuous solutions that the higher order polynomial reconstruction can still reduce the BV ? With the above question, we do the following test. We assume a discontinuity located right in the middle of computational domain as displayed in Fig. 2.2(b). The BV at boundary which is marked by the vertical line is computed by using the polynomial of various orders. The resulting BV is shown in Fig. 2.2(a) . We can notice an interesting phenomena. With the increase of the polynomial order, the BV is not accordingly decreased. On the contrary, if we take a close look at BV computed by even and odd order of polynomial separately, we can see for each case, the BV is increased with the increase

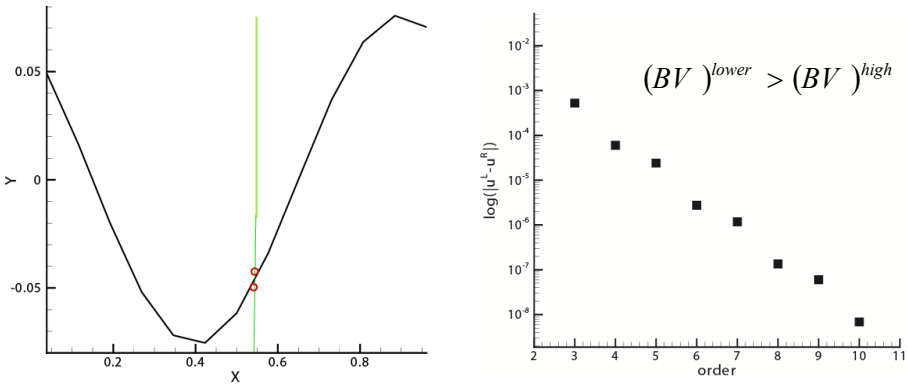

FIGURE 2.1: The distribution of a sine wave on a 11-cell mesh (a) and the magnitude of BV computed by different orders of reconstruction polynomials (b) at the cell interface marked by the green line in (a).

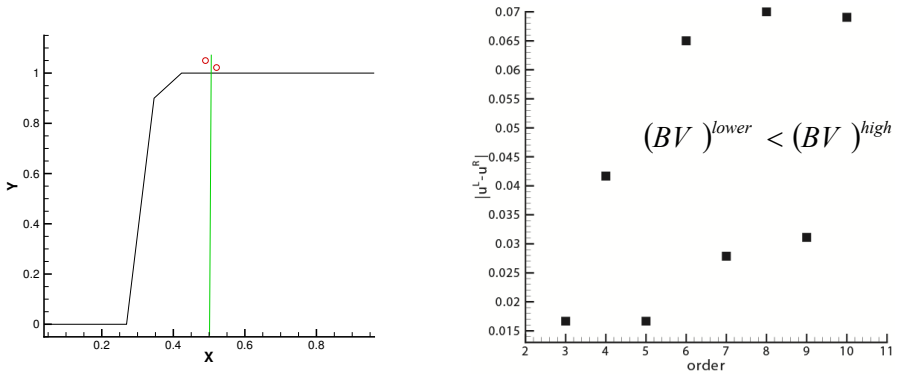

FIGURE 2.2: The distribution of a jump discontinuity on a 11-cell mesh (a) and the magnitude of BV computed by different orders of reconstruction polynomials (b) at the cell interface marked by the green line in (a).

of order of polynomial. This observation is totally in contrary to the case of smooth profile. From this observation, we can conclude that it is not always true that the high order polynomial can necessarily reduce the BV at the cell interface for discontinuous profile.

Based on the above observation, we deem that the mere increase of the polynomial order does not necessarily decrease the BV at the cell interface, i.e. the numerical dissipation term. This is the reason why current FVMs always encounter large numerical dissipation near the discontinuous solutions. Therefore, we propose a novel guideline for reconstruction that adaptively chooses proper interpolation functions so as to minimize the jump between the left- and right- side values, u^L and u^R, at each cell interface, i.e.

BV. The new scheme is called boundary variation diminishing (BVD) method, and we will elaborate the algorithm of BVD reconstruction in the following paragraphs.

2.2 Numerical algorithm

We use a scalar conservation law in the following form to present the BVD algorithm

$$\frac{\partial u}{\partial t} + \frac{\partial f}{\partial x} = 0, \tag{2.3}$$

where $u(x)$ is the solution function and $f(u)$ is the flux function. For a hyperbolic equation, $\alpha = f^{'}(u)$ is a real number, the characteristic speed.

We divide the computational domain into N non-overlapping cell elements, $I_i = [x_{i-\frac{1}{2}}, x_{i+\frac{1}{2}}]$, $i = 1, 2, \cdots, N$. The mesh is assumed to be uniform across the computational domain for simplicity, $\Delta x = x_{i+\frac{1}{2}} - x_{i-\frac{1}{2}}$, which is not essential and formulations on non-uniform meshes can be constructed under the same concept.

Using an FVM framework, we define the VIA of a function $u(x)$ for cell I_i as

$$\overline{u}_i = \frac{1}{\Delta x} \int_{x_{i-\frac{1}{2}}}^{x_{i+\frac{1}{2}}} u(x,t)dx. \tag{2.4}$$

The VIA $\bar{u}_i$ of each cell $I_i = [x_{i-\frac{1}{2}}, x_{i+\frac{1}{2}}]$ is updated by

$$\frac{d\bar{u}_i}{dt} = -\frac{1}{\Delta x}(\tilde{f}_{i+\frac{1}{2}} - \tilde{f}_{i-\frac{1}{2}}), \tag{2.5}$$

where the numerical fluxes at the cell boundaries are computed by a Riemann solver

$$\tilde{f}_{i+\frac{1}{2}} = f^{\text{Riemann}}_{i+\frac{1}{2}}(u^L_{i+\frac{1}{2}}, u^R_{i+\frac{1}{2}}), \tag{2.6}$$

using the left-side value u^L and right-side value u^R obtained from the reconstructions over left- and right-biased stencils. In spite of different variants, the Riemann flux is

essentially upwinding and can be thus written in a canonical form as

$$f^{\text{Riemann}}_{i+\frac{1}{2}}(u^L_{i+\frac{1}{2}}, u^R_{i+\frac{1}{2}}) = \frac{1}{2}\left(f(u^L_{i+\frac{1}{2}}) + f(u^R_{i+\frac{1}{2}}) - |\tilde{\alpha}_{i+\frac{1}{2}}|(u^R_{i+\frac{1}{2}} - u^L_{i+\frac{1}{2}})\right), \tag{2.7}$$

where $\tilde{\alpha}_{i+\frac{1}{2}}$ stands for a characteristic speed in a hyperbolic equation. The last term in (2.7) can be interpreted as the numerical dissipation.

Our central task now is how to calculate the left-side value $u^L_{i+\frac{1}{2}}$ and right-side value $u^R_{i+\frac{1}{2}}$ for all cell boundaries $x_{i+\frac{1}{2}}$, $i = 1, 2, \cdots, N$.

2.2.1 Boundary variation diminishing (BVD) reconstruction

We propose a novel guideline for reconstruction that adaptively chooses proper interpolation functions so as to minimize the jump between the left- and right- side values, u^L and u^R, at the cell interface. We elaborate the algorithm of boundary variation diminishing (BVD) reconstruction for cell I_i as follows.

i) Prepare two piece-wisely reconstructed interpolation functions, $\Phi_i^{<1>}(x)$ and $\Phi_i^{<2>}(x)$, of solution function $u(x)$ for each cell from the VIAs $\bar{u}_i$ available over the computational domain. The existing reconstruction methods, such as WENO and THINC described later, can be employed for this purpose. Without losing generality, we assume that $\Phi_i^{<1>}(x)$ is a higher-order polynomial-based interpolant, while $\Phi_i^{<2>}(x)$ might be of low-order but has better monotonicity (a sigmoid function is preferred for step-like discontinuity, for example);

ii) Find $\Phi_i^{<p>}(x)$ and $\Phi_{i+1}^{<q>}(x)$ with p and q being either 1 or 2, so that the boundary variation (BV)

$$BV(\Phi)_{i+\frac{1}{2}} = |\Phi_i^{<p>}(x_{i+\frac{1}{2}}) - \Phi_{i+1}^{<q>}(x_{i+\frac{1}{2}})|, \tag{2.8}$$

is minimized;

iii) In case that a different choice for cell i is made when applying step ii) to the neighboring interface $x_{i-\frac{1}{2}}$, that is, $\Phi_i^{<p'>}(x)$ found to minimize

$$BV(\Phi)_{i-\frac{1}{2}} = |\Phi_{i-1}^{<p'>}(x_{i-\frac{1}{2}}) - \Phi_i^{<q'>}(x_{i-\frac{1}{2}})|, \tag{2.9}$$

with p' and q' being either 1 or 2, is different from that found to minimize (2.8), we adopt the following criterion to uniquely determine the reconstruction function.

$$\Phi_i^{<p>}(x) = \begin{cases} \Phi_i^{<1>}(x), \text{ if } \left(\Phi_i^{<p>}(x_{i+\frac{1}{2}}) - \Phi_{i+1}^{<q>}(x_{i+\frac{1}{2}})\right)\left(\Phi_{i-1}^{<p'>}(x_{i-\frac{1}{2}}) - \Phi_i^{<q'>}(x_{i-\frac{1}{2}}\right) < 0, \\ \Phi_i^{<2>}(x), \text{ otherwise.} \end{cases} \tag{2.10}$$

iv) Compute the left-side value $u_{i+\frac{1}{2}}^L$ and the right-side value $u_{i-\frac{1}{2}}^R$ for each cell by

$$u_{i+\frac{1}{2}}^L = \Phi_i^{<p>}(x_{i+\frac{1}{2}}) \text{ and } u_{i-\frac{1}{2}}^R = \Phi_i^{<p>}(x_{i-\frac{1}{2}}). \tag{2.11}$$

Remark 1. The BVD algorithm reduces the reconstructed jumps at the cell interfaces, and thus the numerical dissipation term $ND_{i+\frac{1}{2}} = |\tilde{\alpha}|_{i+\frac{1}{2}}(u_{i+\frac{1}{2}}^R - u_{i+\frac{1}{2}}^L)$ in Riemann solvers, which can be expected to effectively improve the numerical solution.

Remark 2. For smooth solution, the BVD reconstruction naturally realizes the highest possible interpolation because interpolants of higher order tend to find an interface value closer to the continuous "true" solution.

Remark 3. For discontinuous solution, pursuing higher order polynomials does not necessarily lead to the reduction of the reconstructed boundary jumps. It might imply the limitation of the current practice to use high-order polynomials for reconstruction.

Remark 4. By minimizing the jumps at the cell boundaries, the BVD algorithm requires a reconstruction that is able to represent a jump within the cell where a discontinuity exists. In this sense, the THINC reconstruction shown later is preferred to a polynomial.

Remark 5. The BVD reconstruction provides a practical and effective guidance to construct high-fidelity schemes for resolving discontinuous solutions. As shown later, excellent numerical results can be obtained if the candidate reconstructions, $\Phi_i^{<1>}(x)$ and $\Phi_i^{<2>}(x)$, are properly chosen.

Remark 6. Another simpler alternative to (2.10) is

$$\Phi_i^{<p>}(x) = \begin{cases} \Phi_i^{<1>}(x), \text{ if } (\bar{u}_i - \bar{u}_{i+1})(\bar{u}_{i-1} - \bar{u}_i) < 0, \\ \Phi_i^{<2>}(x), \text{ otherwise.} \end{cases} \tag{2.12}$$

It does not make significant difference in our numerical experiments.

Remark 7. Other BV-equivalent quantities can be also used in the algorithm. For example, we have tested to minimize the total boundary variation (TBV), $TBV(\Phi)_i = |BV(\Phi)_{i-\frac{1}{2}}| + |BV(\Phi)_{i+\frac{1}{2}}|$ for cell i, which gives quite similar results but is more algorithmically complicated. For FVM, when we use the Lax-Friedrich flux as the numerical flux, the update of VIA can be written as

$$\begin{aligned} \bar{u}_i^{n+1} - \bar{u}_i^n = &-\frac{\Delta t}{\Delta x}\frac{\left(\hat{f}(u_{i+\frac{1}{2}}^L) + \hat{f}(u_{i+\frac{1}{2}}^R)\right) - \left(\hat{f}(u_{i-\frac{1}{2}}^L) + \hat{f}(u_{i-\frac{1}{2}}^R)\right)}{2} \\ &+ \frac{1}{2}\alpha\Delta x\frac{\left(u_{i+\frac{1}{2}}^R - u_{i+\frac{1}{2}}^L\right) - \left(u_{i-\frac{1}{2}}^R - u_{i-\frac{1}{2}}^L\right)}{\Delta x^2}, \end{aligned} \tag{2.13}$$

where

$$\alpha = \max_u |f^{'}(u)|. \tag{2.14}$$

The second part at the right hand side of equation (2.13) represents the viscous term that is in fact the second order derivative. From the numerical viscosity

$$\frac{\left(u_{i+\frac{1}{2}}^R - u_{i+\frac{1}{2}}^L\right) - \left(u_{i-\frac{1}{2}}^R - u_{i-\frac{1}{2}}^L\right)}{\Delta x^2}, \tag{2.15}$$

we can see that current BVD reconstruction that minimizes the $BV(\Phi)_{i+\frac{1}{2}}$ and $BV(\Phi)_{i-\frac{1}{2}}$ is only the sufficient condition for the minimization of the numerical dissipation. Being aware of that the numerical dissipation appears eventually in

a numerical scheme as $ND_{i+\frac{1}{2}} - ND_{i-\frac{1}{2}}$, we see another future option to minimize effective numerical dissipation (END), $END(\Phi)_i = |ND_{i+\frac{1}{2}} - ND_{i-\frac{1}{2}}|$, where $ND_{i+\frac{1}{2}} = |\tilde{\alpha}|_{i+\frac{1}{2}}(\Phi_{i+1}^{<q>}(x_{i+\frac{1}{2}}) - \Phi_i^{<p>}(x_{i+\frac{1}{2}}))$ is the numerical dissipation term. The sufficient and necessary condition for the minimization of numerical dissipation should be the minimization of END. Even though, we still believe that the current BVD criterion provides an algorithmically simple and practical way to reduce the numerical dissipation, which achieves a good balance between the ability to reduce the numerical dissipation and computational complexity.

2.2.2 The building-block reconstruction schemes

As shown in the BVD reconstruction algorithm, we need two building-block schemes to construct the candidate interpolation functions, $\Phi_i^{<1>}(x)$ and $\Phi_i^{<2>}(x)$. In order to enable the resulting scheme to accurately resolve both smooth and discontinuous solutions, we use two fifth-order WENO reconstructions, known as the WENO-Z scheme [6] and the fifth-order targeted ENO (TENO5) scheme [23] to construct $\Phi_i^{<1>}(x)$, while use the THINC scheme [100, 101] to construct $\Phi_i^{<2>}(x)$. We give a brief description for each of these algorithms as below.

2.2.2.1 The (W/T)ENO reconstructions for $\Phi_i^{<1>}(x)$

Both WENO-Z and TENO5 schemes compute the cell interface values by

$$\Phi_i^{<1>}(x_{i\pm\frac{1}{2}}) = \omega_0 u^{(0)}_{i\pm\frac{1}{2}} + \omega_1 u^{(1)}_{i\pm\frac{1}{2}} + \omega_2 u^{(2)}_{i\pm\frac{1}{2}}, \tag{2.16}$$

where $u^{(0)}$, $u^{(1)}$ and $u^{(2)}$ are computed from the third-order polynomials constructed separately over three slided 3-cell stencils. It is noted that an uniform grid is assumed here for simplicity, but is not essential.

$$\begin{aligned}
u^{(0)}_{i-\frac{1}{2}} &= \frac{1}{3}\overline{u}_{i+2} - \frac{7}{6}\overline{u}_{i+1} + \frac{11}{6}\overline{u}_i,\ u^{(1)}_{i-\frac{1}{2}} = -\frac{1}{6}\overline{u}_{i+1} + \frac{5}{6}\overline{u}_i + \frac{1}{3}\overline{u}_{i-1},\ u^{(2)}_{i-\frac{1}{2}} = \frac{1}{3}\overline{u}_i + \frac{5}{6}\overline{u}_{i-1} - \frac{1}{6}\overline{u}_{i-2};\\
u^{(0)}_{i+\frac{1}{2}} &= \frac{1}{3}\overline{u}_{i-2} - \frac{7}{6}\overline{u}_{i-1} + \frac{11}{6}\overline{u}_i,\ u^{(1)}_{i+\frac{1}{2}} = -\frac{1}{6}\overline{u}_{i-1} + \frac{5}{6}\overline{u}_i + \frac{1}{3}\overline{u}_{i+1},\ u^{(2)}_{i+\frac{1}{2}} = \frac{1}{3}\overline{u}_i + \frac{5}{6}\overline{u}_{i+1} - \frac{1}{6}\overline{u}_{i+2}.
\end{aligned} \tag{2.17}$$

The computation of the non-linear weights, ω_j, $j = 0, 1, 2$, depends on the smoothness indicator which measures the smoothness of solution function $u(x)$. Different formulations are used in the WENO-Z and TENO5 reconstructions to compute the nonlinear weights.

Interested readers are referred to [6] and [23] for details. We summarize the key formulate to calculate the non-linear weights in both WENO-Z and TENO5 schemes as follows.

For WENO-Z scheme, the non-linear weights is computed by

$$\omega_k = \frac{\alpha_k}{\sum_{k=0}^{2} \alpha_k},\ \alpha_k = d_k \left(1 + \left(\frac{\tau_5}{\beta_k + \epsilon}\right)^q\right),\ \tau_5 = |\beta_2 - \beta_0|,\ k = 0, 1, 2, \quad (2.18)$$

where d_k is the optimal weight to recover the full 5th-order scheme with the values $d_0 = 0.1,\ d_1 = 0.6,\ d_2 = 0.3$. $q = 1$ is recommended to control the excessive numerical dissipation in non-smooth region. The smoothness indicator β_k is defined following Jiang and Shu [45] as

$$\beta_j = \sum_{l=1}^{2} \int_{x_{i-\frac{1}{2}}}^{x_{i+\frac{1}{2}}} \Delta x^{2l-1} \left(\frac{d^l u^j(x)}{dx^l}\right)^2 dx, \quad j = 0, 1, 2. \quad (2.19)$$

For the TENO5 scheme, the smoothness measure is defined as

$$\gamma_k = \left(C + \frac{\tau_K}{\beta_k + \epsilon}\right)^q,\ k = 0, \ldots, K - 3, \quad (2.20)$$

where $K = 5$ is the maximum order for the TENO5 scheme. $C = 1$ and $q = 6$ is suggested in [23] to balance between numerical dissipation and computation robustness. The core of the TENO scheme is the ENO-like stencil selection procedure. Firstly, the normalization of the smoothness measure is given by

$$\chi_k = \frac{\gamma_k}{\sum_{k=0}^{2} \gamma_k},\ k = 0, 1, 2, \quad (2.21)$$

then the cut-off function is defined subjected to χ_k as

$$\delta_k = \begin{cases} 0, & \text{if } \chi_k < C_T \\ 1, & \text{otherwise} \end{cases} \quad k = 0, 1, 2, \tag{2.22}$$

where the C_T is set to be 10^{-5}. Finally, the nonlinear weight can be obtained from a renormalization procedure as

$$\omega_k = \frac{d_k \delta k}{\sum_{k=0}^{2} d_k \delta_k}, \; k = 0, 1, 2, \tag{2.23}$$

As discussed in [23], the TENO5 scheme is superior to the WENO-Z scheme in resolving discontinuities with less numerical dissipation. We compared the two schemes in some numerical tests and observed that both work well under the BVD framework, and the original properties of WENO-Z and TENO5 can be observed when implemented with the BVD principle.

2.2.2.2 The THINC reconstruction for $\Phi_i^{<2>}(x)$

Being a sigmoid function, hyperbolic tangent function is a differentiable and monotone function that fits well a step-like discontinuity. A class of VOF(volume of fluid) schemes, so-called THINC (Tangent of Hyperbola for INterface Capturing), has been devised to compute moving interfaces in multiphase flow simulations [9, 75, 100, 101] based on the hyperbolic tangent function. In the present work, we use THINC reconstruction as the second candidate interpolation function $\Phi_i^{<2>}(x)$ in the BVD algorithm

$$\Phi_i^{<2>}(x) = u_{min} + \frac{u_{max}}{2}\left(1 + \gamma \tanh\left(\beta\left(\frac{x - x_{i-\frac{1}{2}}}{x_{i+\frac{1}{2}} - x_{i-\frac{1}{2}}} - \tilde{x}_i\right)\right)\right), \tag{2.24}$$

where $u_{min} = \min(\bar{u}_{i-1}, \bar{u}_{i+1})$, $u_{max} = \max(\bar{u}_{i-1}, \bar{u}_{i+1}) - u_{min}$ and $\gamma = \mathrm{sgn}(\bar{u}_{i+1} - \bar{u}_{i-1})$. Parameter β is used to control the jump thickness. We use a constant value of $\beta = 1.6$ for most of the numerical tests in this Chapter. We need to notice that β can also be given in a variable formulation. In some cases, the variable β can yield better

numerical solutions. The variable β is defined by

$$\beta = \beta_{min} + \frac{(u_{max} - u_{min})^7}{\Delta x} \frac{(\beta_{max} - \beta min)}{S}, \tag{2.25}$$

where β_{max} and β_{min} is the given range where β is allowed to fluctuate, and S is a constant scaling factor. In the numerical tests presented in this paper, without specific indication, we use a constant β in our computation.

The unknown $\tilde{x}_i$, which represents the location of the jump center, is computed from the constraint condition, $\bar{u}_i = \frac{1}{\Delta x} \int_{x_{i-\frac{1}{2}}}^{x_{i+\frac{1}{2}}} \Phi_i^{<2>}(x) dx$.

Rather than showing explicitly the formula to calculate $\tilde{x}_i$, we give the expressions for the reconstructed left- and right-end values of cell i by

$$\begin{aligned} \Phi_i^{<2>}(x_{i+\frac{1}{2}}) &= u_{min} + \frac{u_{max}}{2} \left(1 + \gamma \frac{\tanh(\beta) + A}{1 + A\tanh(\beta)}\right), \\ \Phi_i^{<2>}(x_{i-\frac{1}{2}}) &= u_{min} + \frac{u_{max}}{2}(1 + \gamma A), \end{aligned} \tag{2.26}$$

where $A = \frac{B/\cosh(\beta)-1}{\tanh(\beta)}$, $B = \exp\left(\gamma\beta\left(2\frac{\bar{u}_i - \bar{u}_{min} + \epsilon}{u_{max} + \epsilon} - 1\right)\right)$ and $\epsilon = 10^{-20}$. It should be noted that the THINC reconstruction applies only to cells where $(\overline{u}_{i+1} - \overline{u}_i)\,(\overline{u}_i - \overline{u}_{i-1}) > 0$ hold.

Remark 8. We also experimented using piece-wise constant and MUSCL reconstructions for $\Phi_i^{<2>}(x)$, and find that the BVD algorithm results in a less oscillatory solution without noticeable increase in numerical dissipation in comparison with the computations which only use WENO-Z or TENO5 reconstructions. Another combination that uses MUSCL for $\Phi_i^{<1>}(x)$ and THINC for $\Phi_i^{<2>}(x)$ gives significant improvement in resolving contact discontinuities in numerical solutions as well.

We refer to the BVD algorithm using WENO-Z and THINC reconstructions as BVD-WENOZ-THINC method, and the BVD algorithm using TENO5 and THINC reconstructions as BVD-TENO5-THINC method in this paper. More explicitly, WENO-Z reconstruction is used for $\Phi_i^{<1>}(x)$ and THINC for $\Phi_i^{<2>}(x)$ in BVD-WENOZ-THINC

method, while TENO5 reconstruction is used for $\Phi_i^{<1>}(x)$ and THINC reconstruction for $\Phi_i^{<2>}(x)$ in BVD-TENO5-THINC method.

For Euler equations, the (W/T)ENO and THINC reconstructions are implemented to the characteristic variables, and the minimization in the BVD algorithm is conducted in terms of the primitive variables separately, i.e. density, velocity and pressure. We use Roe's Riemann solver [67] to calculate the numerical fluxes.

The five stage fourth order strong stability preserving (SSP) Runge-Kutta method [27, 79] is used for time marching with a Courant-Friedrich-Lewy (CFL) number of 0.4 in the numerical tests presented next.

2.3 Analysis of the computational efficiency and numerical errors for BVD scheme

In this section, we measure the computational efficiency of BVD scheme by comparing the computational time of the advection of a square wave on a 10000-mesh cell after one period between the BVD scheme and FVM without BVD reconstruction. The initial condition of test case is given as

$$u(x,0) = \begin{cases} 1, & \text{when}|\text{x}| \leqslant 0.4, \\ 0, & \text{otherwise.} \end{cases} \tag{2.27}$$

where the computation domain is $x \in [-1, 1]$. The computational is performed up to $t = 2.0$.

In this quantitative measurement, we use THINC and WENO-Z reconstruction as the building block for BVD scheme, while for FVM we use the WENO-Z scheme in our computation. The elapsed time is given as follows

$$\begin{cases} \text{Time taken by BVD scheme} : 1126.33\text{s} \\ \text{Time taken by WENO} - \text{Z scheme} : 937.25 \end{cases} \tag{2.28}$$

We can see that the BVD reconstruction brings in about 20% extra computational time.

Also, we compare the total error, dissipation error and dispersion error between the numerical results computed by BVD-WENOZ-THINC scheme and only WENO-Z scheme. The total error E_{TOT}, dispersion error E_{DISP} and dissipation error E_{DISS} is measured using the method presented in [82]. The total error E_{TOT} is defined by the mean square error for numerical solutions as

$$E_{TOT} = \frac{1}{N}\sum_{i=0}^{N}(\overline{u}_i^n - \overline{u}_i^e)^2, \tag{2.29}$$

where $\overline{u}_i^n$ is the numerical solution of the VIA for cell i, $\overline{u}_i^e$ represents the exact solution and N the mesh number. The total error can be split into the dissipation error E_{DISS} and dispersion error E_{DISP}

$$E_{TOT} = E_{DISS} + E_{DISP}, \tag{2.30}$$

where

$$\begin{aligned} E_{DISS} &= \left(\sigma(\overline{u}^n) - \sigma(\overline{u}^e)\right)^2 + \left(\overline{\overline{u}^n} - \overline{\overline{u}^e}\right)^2, \\ E_{DISP} &= 2(1-\rho)\sigma(\overline{u}^n)\sigma(\overline{u}^e). \end{aligned} \tag{2.31}$$

Here $\sigma(\overline{u}^n)$ is the standard deviation of numerical solution $\overline{u}^n$, $\sigma(\overline{u}^e)$ is the standard deviation of analytic solution $\overline{u}^e$ and $\overline{\overline{u}^e}$ represents the mean value of $\overline{u}^e$ while $\overline{\overline{u}^n}$ is the mean value of $\overline{u}^n$. ρ is the correlation coefficient between $\overline{u}^n$ and $\overline{u}^e$ defined by

$$\rho = \frac{cov(\overline{u}^e, \overline{u}^n)}{\sigma(\overline{u}^n)\sigma(\overline{u}^e)}, \tag{2.32}$$

where $cov(\overline{u}^e, \overline{u}^n)$ is the covariance of $\overline{u}^n$ and $\overline{u}^e$. If $\overline{u}^e$ and $\overline{u}^e$ are exactly correlated, i.e. $\rho = 1$, then the dispersion error defined in (2.31) will become zero, which means that the numerical error is only from the numerical dissipation.

The three error measurements of numerical errors of advection of a square wave (2.27) are given in Table 2.1. We can see that by using BVD reconstruction, both of the total error, numerical dissipation error and numerical dispersion error are significantly reduced.

Compared to the results computed by just WENO-Z scheme, the total error and numerical dispersion error is reduced by about 63%, while the numerical dissipation error is reduced by more than 73%. This observation confirmed that the BVD reconstruction can effectively reduce not only the numerical dissipation error but also the overall error and numerical dispersion error for the solutions including jump discontinuity.

TABLE 2.1: Comparison of E_{TOT},E_{DISS} and E_{DISP} between BVD-WENOZ-THINC scheme and WENO-Z scheme for advection of a square wave

Scheme	E_{TOT}	E_{DISS}	E_{DISP}
BVD-WENOZ-THINC scheme	1.40e-03	2.55e-05	1.37e-03
WENO-Z scheme	3.81e-03	9.72e-05	3.71e-03

We also count the operations and instructions of our scheme. We use the method given in [99]. The ratio of computational cost between different operations is given as

$$\text{addition} : \min(x) : \text{if} : \text{division} : \text{exponential function} = 1 : 2 : 2.3 : 6 : 6 \qquad (2.33)$$

The operation counts of BVD-WENOZ-THINC scheme and WENO-Z scheme is shown in Table 2.2. We can learn from the table that the BVD reconstruction introduces about 33.1% computational burden in terms of operation counts.

TABLE 2.2: Operation Counts of Different Schemes.

Operation	BVD-WENOZ-THINC scheme	WENO-Z scheme
if logic	14	5
+,-,*,ABS(x)	192	160
/	14	12
MAX(x), or MIN(x)	2	0
Exponential function	2	0
Summation	324.2	243.5

From the above analysis, we deem that the slight increase of computational burden can be acceptable in exchange for the significant reduction of the numerical dissipation near the discontinuities, especially for the computation of Euler equations where the accurate simulation of discontinuous solutions turns out to be an important issue.

2.4 Numerical experiments

In this section, the numerical results of some benchmark tests for scalar and Euler conservation laws are presented to illustrate the performance of the BVD algorithm described above.

2.4.1 Linear advection equation

Firstly, we consider the following 1D linear advection equation

$$u_t + u_x = 0. \tag{2.34}$$

Example 2.1. **Accuracy test for 1D advection equation.** An initially smooth profile defined by $u(x,0) = \sin(\pi x),\ x \in [-1,1]$ is advected. The L_1 and L_∞ errors of VIA after one period are measured under different grid resolutions. Shown in Table 4.4, the numerical errors of BVD-WENO-THINC are identical to that of WENO-Z for all grid resolutions. It proves that the BVD-WENO-THINC scheme retrieves the $5th$ order WENO schemes for smooth solution.

TABLE 2.3: Numerical errors and convergence rate for 1D advection equation, $t = 2.0$.

N	BVD-WENO-THINC scheme				WENO-Z scheme			
	L_1 error	Order	L_∞	Order	L_1 error	Order	L_∞	Order
20	2.14e-04		3.65e-06		2.14e-04		3.65e-06	
40	6.40e-06	5.07	1.03e-05	5.10	6.40e-06	5.07	1.03e-05	5.10
80	2.00e-07	5.00	3.18e-07	5.02	2.00e-07	5.00	3.18e-07	5.02
160	6.32e-09	4.99	9.96e-09	5.00	6.32e-09	4.99	9.96e-09	5.00
320	2.04e-10	4.00	3.20e-10	4.96	2.04e-10	4.00	3.20e-10	4.96

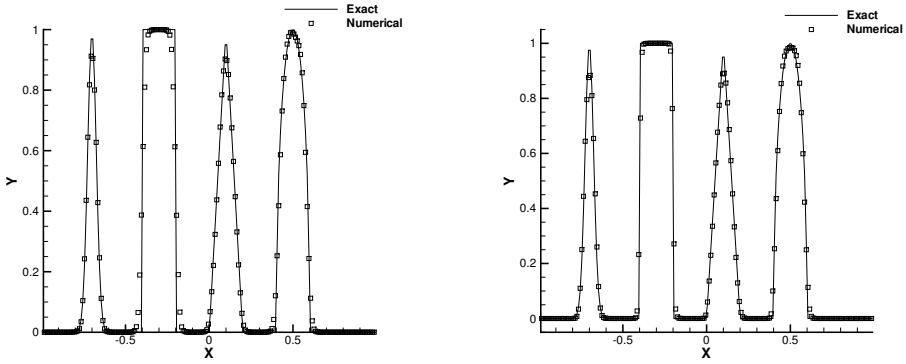

FIGURE 2.3: Numerical results of Jiang and Shu's test after one period (t = 2.0) with 200 grid cells computed by WENO-Z scheme (left) and BVD-WENOZ-THINC scheme (right).

Example 2.2. **Jiang and Shu's test.** The initial condition of this test includes both discontinuities and smooth profile. We set the initial condition as

$$u(x,0) = \begin{cases} \dfrac{1}{6}\left(G(x,\beta,z-\delta) + G(x,\beta,z+\delta) + 4G(x,\beta,z)\right), & -0.8 \leqslant x \leqslant -0.6, \\ 1, & -0.4 \leqslant x \leqslant -0.2, \\ 1 - |10(x-0.1)|, & 0.0 \leqslant x \leqslant 0.2, \\ \dfrac{1}{6}\left(F(x,\alpha,a-\delta) + F(x,\alpha,a+\delta) + 4F(x,\alpha,a)\right), & 0.4 \leqslant x \leqslant 0.6, \\ 0, & \text{otherwise}, \end{cases} \tag{2.35}$$

where the computation domain is $[-1,1]$. The function F and G is defined by

$$G(x,\beta,z) = \exp\left(-\beta(x-z)^2\right), F(x,\alpha,a) = \sqrt{\max(1-\alpha^2(x-a)^2, 0)}, \tag{2.36}$$

and the coefficients to determine the initial profile are given by

$$a = 0.5,\ z = 0.7,\ \delta = 0.005,\ \alpha = 10.0,\ \beta = \log 2/(36\delta^2). \tag{2.37}$$

The numerical results are shown in Fig.2.3. Compared to the WENO-Z method (Fig.2.3 (left)), the BVD-WENOZ-THINC method (Fig.2.3 (right)) can resolve the sharp discontinuity with significantly improved quality while keeping the smooth profile with good resolution.

Example 2.3. **Advection of jump discontinuity.** In this test, we analyze the sharpness of a single discontinuity for advection equation. Initially, the discontinuity is located at $x = 0.5$, defined as

$$u(x,0) = \begin{cases} 1, \ 0.0 \leqslant x \leqslant 0.5 \\ 0, \ \text{otherwise.} \end{cases} \tag{2.38}$$

To demonstrate the ability of BVD-WENOZ-THINC in minimizing the numerical dissipation, we display the numerical results at $t = 0.25$ on a 200-cell mesh computed by WENO-Z, THINC and BVD-WENOZ-THINC scheme respectively in Fig.2.4. It can be observed that the sharpness is thinner for both THINC and BVD-WENOZ-THINC scheme than WENO-Z scheme, and THINC and BVD-WENOZ-THINC scheme has almost the same resolution for jump discontinuity. To further examine the sharpness quantitatively, we introduce the thickness measurement of a discontinuity proposed by in [56] as

$$\delta_{thickness} = \frac{\alpha_{jump}}{\Delta x} \frac{1}{\max(\frac{\delta u}{\delta x})} = \frac{\alpha_{jump}}{\max(u_j - u_{j-1})} \tag{2.39}$$

where $\alpha_{jump} = 1$ for this test. The results are shown in Table 2.4. As expected, the thickness of discontinuity for WENO-Z scheme is much larger than that of the BVD-WENOZ-THINC and THINC schemes. Although the difference of thickness between BVD-WENOZ-THINC and THINC scheme is small, the BVD-WENOZ-THINC scheme looks even better that the pure THINC computation in resolving a thin discontinuity, which manifests the effectiveness of the BVD-THINC based schemes in minimizing numerical dissipation.

TABLE 2.4: Comparison of discontinuity thickness for the advection of jump discontinuity

	THINC	BVD-WENOZ-THINC	WENOZ
$\delta_{thickness}$	2.02722	2.01354	3.51015

2.4.2 Inviscid Burgers equation

We consider the 1D inviscid Burger's equation

$$u_t + \left(\frac{u^2}{2}\right)_x = 0. \tag{2.40}$$

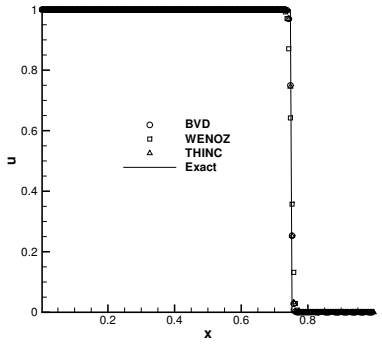

FIGURE 2.4: The advection of jump discontinuity computed by WENO-Z, THINC, and BVD-WENOZ-THINC scheme at $t = 0.25$.

Here we will give two examples for inviscid Burgers equation.

Example 2.4. **Burgers equation with an initial sine wave.** In this test, a sine wave is given as the initial profile, which will develop into a shock wave after $t = 1.5/\pi$ due to the convexity of the Burgers flux. Firstly, in order to measure the convergence rate of the BVD-based algorithm, we carried out the computation with BVD-WENOZ-THINC method up to $t = 0.5/\pi$. The numerical errors are shown in Table 4.8, which demonstrate nearly the $5th$ order accuracy. As the profile is time-dependent for the Burgers equation, the accuracy test can illustrate the time-depending accuracy of our scheme. We also show the numerical results computed on a 100-cell mesh at $t = 1.5/\pi$ in Fig.4.7(left). We can see that the shock wave in this test can be resolved within only two mesh cells.

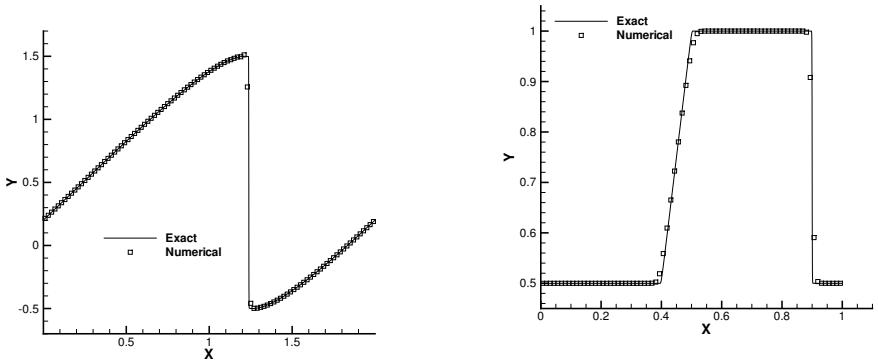

FIGURE 2.5: Numerical results of Burgers equation computed by BVD-WENOZ-THINC scheme. Left: Solution at $t = 1.5/\pi$ on a 100-cell mesh with a sine-wave initial condition. Right: Solution at $t = 0.2$ on a 80-cell mesh with a square pulse initial condition (2.41).

TABLE 2.5: Numerical errors and convergence rates for 1D Burgers equation at $t = 1/(2\pi)$.

N	L_1 error	Order of Accuracy	L_∞ error	Order of Accuracy
20	3.00e-04		2.07e-03	
40	1.66e-05	4.18	2.15e-04	3.27
80	7.36e-07	4.49	9.94e-06	4.43
160	2.65e-08	4.79	3.56e-07	4.80

Example 2.5. **Burgers equation with shock and rarefaction waves.** The initial condition of this benchmark test is given by

$$u(x,0) = \begin{cases} 1, & 0.3 \leqslant x \leqslant 0.75, \\ 0.5, & \text{otherwise}, \end{cases} \tag{2.41}$$

Both shock and rarefaction wave are included in this test. The numerical results at $t = 0.2$ are shown in Fig.4.7(right). The BVD-WENOZ-THINC scheme can reproduce both the shock and expansion fan with good accuracy.

2.4.3 Burgers turbulence

A well-known observation is that Godunov type methods using Riemann solvers, even of high order, generates excessive numerical dissipation to high wave number range, and might not be properly used in large eddy simulations for turbulent flows of high Reynolds number. In order to examine the numerical dissipation of the proposed methods in simulating turbulent flows, we solved Burger turbulence problem introduced in [4]. Burgers equation with viscosity is written as

$$u_t + \left(\frac{u^2}{2}\right)_x = \nu u_{xx}, \tag{2.42}$$

where $\nu = 1 \times 10^{-4}$ is the viscosity coefficient.

The computational domain is $[0, 1]$ with periodical boundary conditions. The Fourier representation of the velocity function is $u(x,t) = \sum_q \hat{u}_q(t) exp(ik_q x)$. The energy of

single model k_q is calculated by $E(k_q,t) = |u(k_q,t)^2|$. The initial condition is prescribed in terms of energy spectrum in the same as in [4], i.e.

$$E(k,0) = A\sigma k^4 exp(-0.5\sigma^2 k^2), \tag{2.43}$$

where constant $A = \frac{U_0^2}{3\sqrt{2\pi}}$ with $U_0^2 = \langle u_0(x)^2 \rangle$ the mean kinetic at $t = 0.0$ and $\sigma = 0.05/2\pi$. The initial velocity field is given through the means of Wiener process. The initial energy spectrum is reported in Fig. 2.6

The initial kinetic energy which is concentrated in the low wave number range is transfered to the high wave number range. In the present paper, the numerical results from WENO-Z scheme on a fine mesh (8192 cells) are referred to as the DNS (Direct numerical simulation) solutions. We computed the Burgers turbulence for a truncated spectral range on a mesh of 1024 cells by both WENO-Z and BVD-WENOZ-THINC methods. Here the diffusing viscous term is solved by the 4th order central difference scheme. The energy spectrum at $t = 0.06$ are plotted in Fig.2.7. It is found that the BVD-WENOZ-THINC method effectively reduces the numerical dissipation in high wave number range compared to the WENO-Z scheme. Also, the velocity distribution in physical field from $x = 0.15$ to $x = 0.35$ is given in Fig.2.8. It shows that BVD-WENZ-THINC scheme can achieve better resolution for velocity field than WENO-Z scheme, although the difference is not so significant. Consistent to all other numerical tests, significant improvement in numerical dissipation can be obtained by the BVD algorithm, which thus are expected to be a general remedy also to other existing methods that are too numerically dissipative to simulate turbulence flows of high Reynolds numbers.

2.4.4 Buckley Leverett equation

1D Buckley Leverett equation reads

$$u_t + \left(\frac{4u^2}{4u^2 + (1-u)^2} \right)_x = 0. \tag{2.44}$$

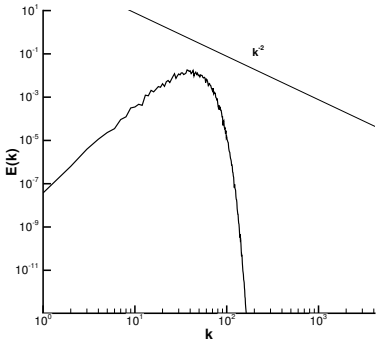

FIGURE 2.6: The prescribed energy spectrum at $t = 0$.

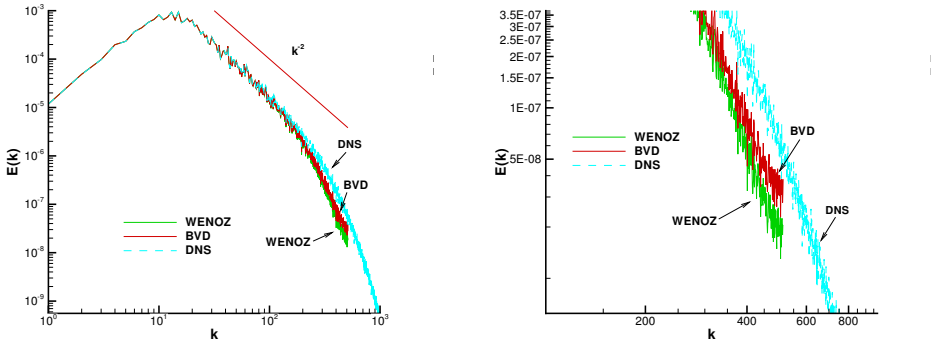

FIGURE 2.7: The energy spectra of Burgers turbulence at $t = 0.06$ on 1024 cells computed by WENO-Z and BVD-WENOZ-THINC schemes. The DNS results are computed on 8192 cells by WENO-Z scheme. Displayed are the spectra for the whole region (left) and the zoomed-in view of high-wave number region (right).

This equation was originally presented by Buckley & Leverett in [8]. The formulation given here is deduced by assuming the relative permeability functions in fractional flow rate are quadratic [78].

Example 2.6. **Square pulse problem.** The initial condition is set to be a square pulse,

$$u(x,0) = \begin{cases} 1, & -\dfrac{1}{2} \leqslant x \leqslant 0, \\ 0, & \text{otherwise}. \end{cases} \tag{2.45}$$

The solution to this test is a mixture of containing shock, rarefaction and contact discontinuity. We carried out the computation up to $t = 0.4$. The numerical results of BVD-WENOZ-THINC method are given in Fig.2.9. We can see that the results are of good quality even with such a low resolution grid.

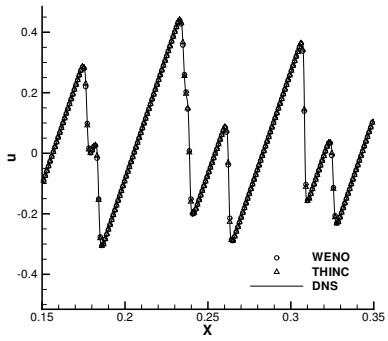

FIGURE 2.8: Velocity distribution at $t = 0.06$ computed by WENO-Z and BVD-WENOZ-THINC schemes. The DNS results are calculated by WENO-Z scheme on 8192 cells.

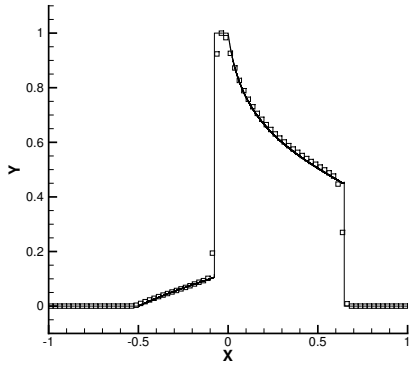

FIGURE 2.9: Numerical solutions of Buckley Leverett problem at $t = 0.2$ with 80 cells.

2.4.5 1D Euler equations

In this subsection, we present the numerical results of some benchmark shock-tube tests for 1D Euler equations to verify our new scheme for resolving the shock wave, contact discontinuity and rarefaction wave in compressible gas flows

Example 2.7. **Sod's problem.** The initial condition is given by

$$(\rho_0, v_0, p_0) = \begin{cases} (1, 0, 1), & 0 \leqslant x \leqslant 0.5, \\ (0.125, 0, 0.1), & \text{otherwise.} \end{cases} \tag{2.46}$$

The mesh number is 100 in this test. The results from both WENO-Z and BVD-WENO-THINC are presented in Fig.2.10 for comparison. It is observed that BVD-WENOZ-THINC scheme resolves better the contact discontinuity and the expansion front, while the solution of WENO-Z looks more dissipative.

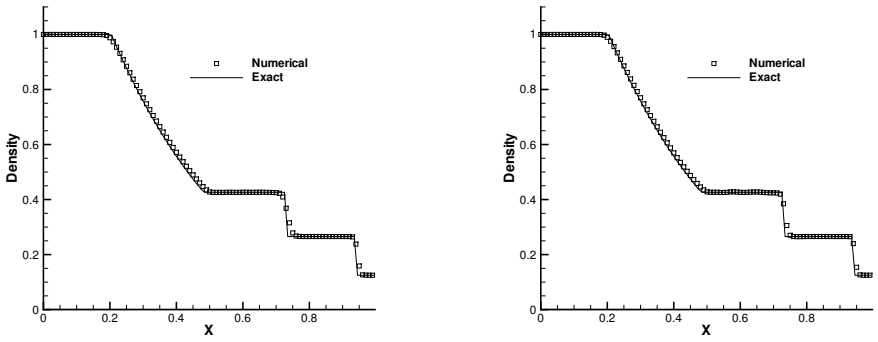

FIGURE 2.10: Sod's problem at $t = 0.25$ with 100 cells solved by WENO-Z (left) and BVD-WENOZ-THINC method (right).

Example 2.8. **Lax's problem.** This is another widely used benchmark test [49] with the initial condition given by

$$(\rho_0, v_0, p_0) = \begin{cases} (0.445, 0.698, 3.528), & 0 \leqslant x \leqslant 0.5, \\ (0.5, 0, 0.571), & \text{otherwise.} \end{cases} \tag{2.47}$$

We show the numerical results at $t = 0.16$ for both WENO-Z and BVD-WENO-THINC are presented in Fig.2.11 for comparison. It can be seen again that our scheme can reproduce sharp contact discontinuity and shock wave, while maintaining the high accuracy for smooth profile. We plot the $t - x$ diagram in Fig.2.12 to demonstrate the cells where the THINC reconstruction is implemented. It reveals that the discontinuities, both contact discontinuity and shock, are properly identified by the BVD criterion. In this test, we also use the variable β in our computation. The parameter for variable β is given as

$$\beta_{min} = 1.6,\ \beta_{max} = 3.0,\ S = 80.0. \tag{2.48}$$

The numerical results are shown in Fig.2.13. We find that by using the variable β, we can get better resolution for contact discontinuity solution. However, to strike a balance

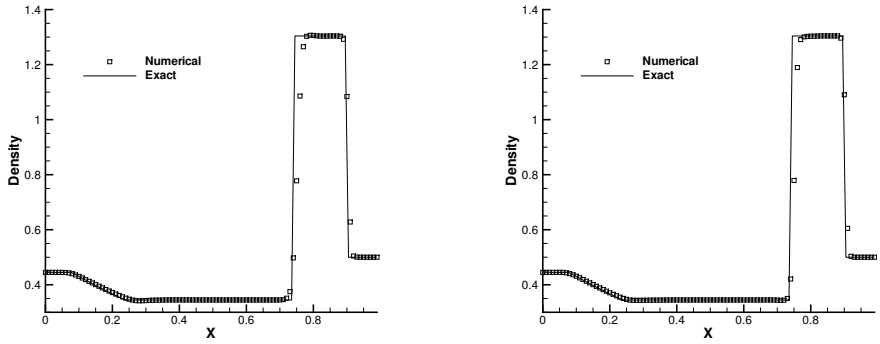

FIGURE 2.11: Lax's problem at $t = 0.16$ with 100 cells solved by WENO-Z (left) and BVD-WENOZ-THINC method (right).

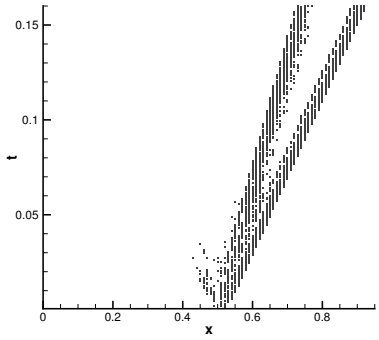

FIGURE 2.12: The mesh cells where the THINC reconstruction for density is implemented based on the BVD principle corresponding to Lax's problem in Fig.2.11.

between robustness and solution resolution, we deem that the constant β is enough to get the solution with less numerical dissipation without damaging the computational stability. A more robust variable β can be seen as a future choice for the development of the BVD reconstruction.

Example 2.9. **A shock-tube test with high Mach number.** The initial condition of this benchmark test is given by

$$(\rho_0, v_0, p_0) = \begin{cases} (1000.0, 0.0, 10000.0), & 0 \leqslant x \leqslant 0.2, \\ (1.0, 0.0, 1.0), & \text{otherwise}. \end{cases} \tag{2.49}$$

The numerical results at $t = 0.05$ are presented in Fig.2.14. The mesh number is 800. Here we give the results computed by both WENO-Z and BVD method. The density are plotted using the log scale to better express the structure of the discontinuities. Through

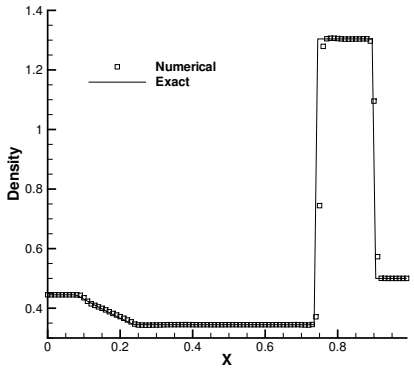

FIGURE 2.13: Lax's problem at $t = 0.16$ with 100 cells solved by BVD-WENOZ-THINC method with the variable β.

the comparison, we can clearly see that the BVD scheme can get better resolution for the contact discontinuity near $x = 0.65$ than WENO-Z scheme. The contact discontinuity computed by BVD scheme can be resolved by only about three cells, while the WENO-Z results need more than seven points.

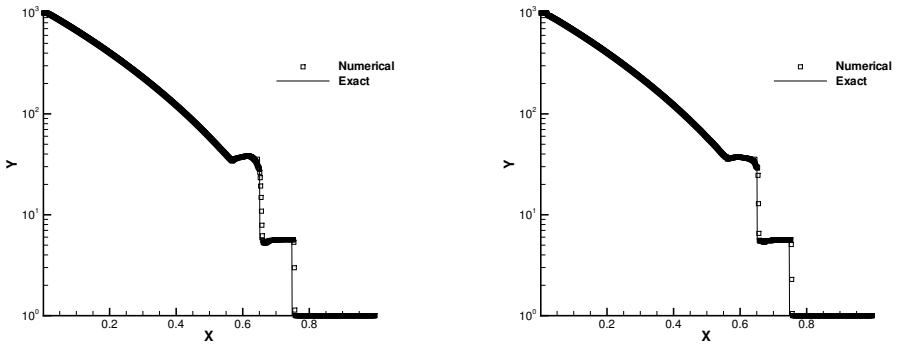

FIGURE 2.14: Shock-tube test with high Mach number at t = 0.16 on a mesh with 800 cells solved by WENO-Z (left) and BVD method (right).

Example 2.10. **Shock-turbulence interaction.** The initial condition of this test is specified by

$$(\rho_0, v_0, p_0) = \begin{cases} (3.857143, 2.629369, 10.333333), & \text{when x} < 0.1, \\ (1.0 + 0.2\sin(50x - 25), 0, 1.0), & \text{when x} \geqslant 0.1. \end{cases} \tag{2.50}$$

The computational domain is $[0, 1]$ and we perform the calculation up to $t = 0.18$ on a mesh of 200 cells. The numerical results of WENO-Z, BVD-WENOZ-THINC and

BVD-TENO5-THINC are shown in Fig.4.12. It is observed that the BVD algorithm does not make significant difference to the smooth solution where the polynomial-based reconstructions are preferred as in the linear advection tests. The difference between WENO-Z and TENO5 is clearly seen in the results.

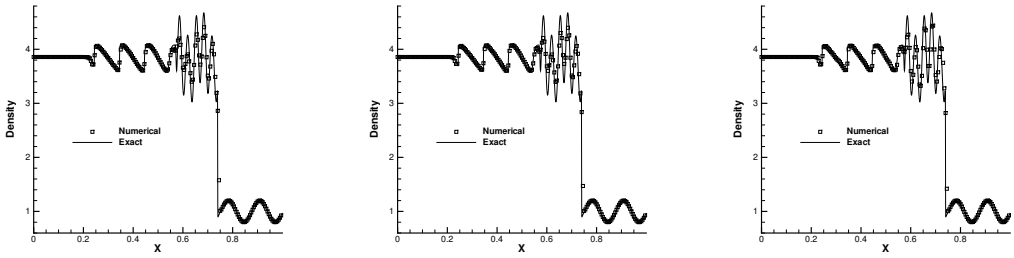

FIGURE 2.15: Numerical results of shock-turbulence interaction at $t = 0.18$ with 200 cells. Displayed are solutions of density computed by WENO-Z (left), BVD-WENOZ-THINC (middle) and BVD-TENO5-THINC (right) method.

Example 2.11. **Two interacting blast waves.** This is a 1D benchmark test including more complicated interactions and discontinuous structures. Initially we set the following condition for state variables,

$$(\rho_0, v_0, p_0) = \begin{cases} (1, 0, 1000), & 0 \leqslant x \leqslant 0.1, \\ (1, 0, 0.01), & 0.1 < x < 0.9, \\ (1, 0, 100), & \text{otherwise}. \end{cases} \tag{2.51}$$

The reflection boundary is set to the left and right ends of computational domain. This test includes the multiple interaction of strong shock waves, density discontinuities and rarefaction waves. The numerical solutions of density computed by WENO-Z, BVD-WENOZ-THINC and BVD-TENO5-THINC are given in Fig.4.14. The common headache to nearly all existing shock-capturing schemes is the overly smeared density discontinuities in the numerical solutions, as can be seen in the result of WENO-Z in Fig.4.14 (a). The numerical results of BVD-WENOZ-THINC (Fig.4.14 (b)) and BVD-TENO5-THINC (Fig.4.14 (c)) are among the best ones ever reported in the literature to this benchmark test. Especially, the resolution of the left-most density discontinuity is resolved within less than four cells, which is much superior to any other existing shock capturing scheme without artificial compression steepening treatment.

In this test, we also give the results computed by BVD-MUSCL-THINC scheme in Fig.4.14 (d), which uses MUSCL scheme as the building-block scheme for smooth resolution. The MUSCL scheme is only 2rd order accuracy, so it will generate more numerical dissipation than high order scheme such as WENO of fifth order accuracy. But we notice from numerical results that after applying the BVD algorithm, the MUSCL scheme can obtain the numerical solutions with the better resolution than those given by fifth order WENO scheme presentd in Fig.4.14 (a).

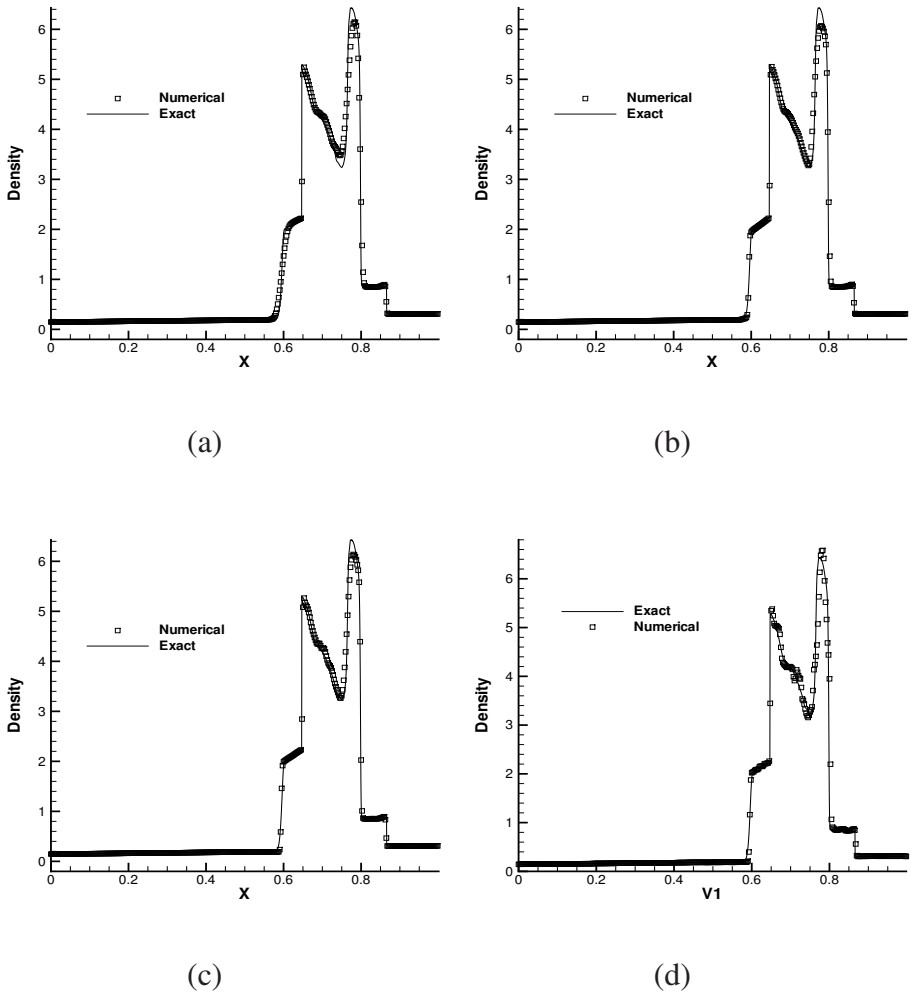

FIGURE 2.16: Numerical results of two interacting blast waves at $t = 0.038$ with 400 cells. Displayed are solutions of density computed by WENO-Z (a), BVD-WENOZ-THINC (b) and BVD-TENO5-THINC (c) method and BVD-MUSCL-THINC scheme (d)

2.4.6 2D Euler equations

Implementing the BVD algorithm in multiple dimensions on structured grids is straightforward. In order to verify the proposed methods in multi-dimensions, we solved two benchmark tests suggested in [94] for 2D Euler equations.

Example 2.12. **Double Mach Reflection.** This benchmark test contains both shock wave and contact discontinuity, and is usually used to verify numerical schemes in capturing strong shocks and vortical structures, which requires a numerical scheme to be optimized in terms of suppressing both numerical oscillation and dissipation.

We computed the solution up to $t = 0.2$ on two meshes of different resolutions. The numerical results of WENO-Z, BVD-WENOZ-THINC and BVD-TENO5-THINC on a 100×320 mesh are shown in Fig.2.17 with the zoomed-in part in Fig.2.18, and the results on a 200×640 mesh are displayed in Fig.2.19 with the zoomed-in region in Fig.2.20. The vortex structures resulted from Kelvin-Helmholtz instabilities along the slip line are the key features to evaluate the intrinsic numerical dissipation of the tested scheme. The vortex is developed with the time-marching. On the coarse mesh of 100×320 cells, the WENO-Z is not able to produce the vortex structures along the slip line, while both BVD-WENOZ-THINC and BVD-TENO5-THINC methods resolved adequately the vortex structures. On the 200×640 mesh, the numerical solutions from BVD-WENOZ-THINC and BVD-TENO5-THINC methods are of high quality comparable to those obtained using discontinuous Galerkin (DG) method with even more degrees of freedom (DOFs) [21, 55, 64]. The favorable resolution of vortex structure validates the good transient performance of our scheme.

Example 2.13. **Mach 3 step tunnel.** In this benchmark test, a right-moving Mach 3 flow in a tunnel with a forward step and reflective boundaries generates complex flows due to the interactions among shocks, density disturbances and shear flows.

We show the numerical results of WENO-Z, BVD-WENOZ-THINC and BVD-TENO5-THINC at $t = 4.0$ on a 100×300 mesh in Fig.2.21. All shock waves are well resolved by three schemes without significant difference, while the vortex structures starting from the front triple point look different. The vortex structures are more clearly resolved

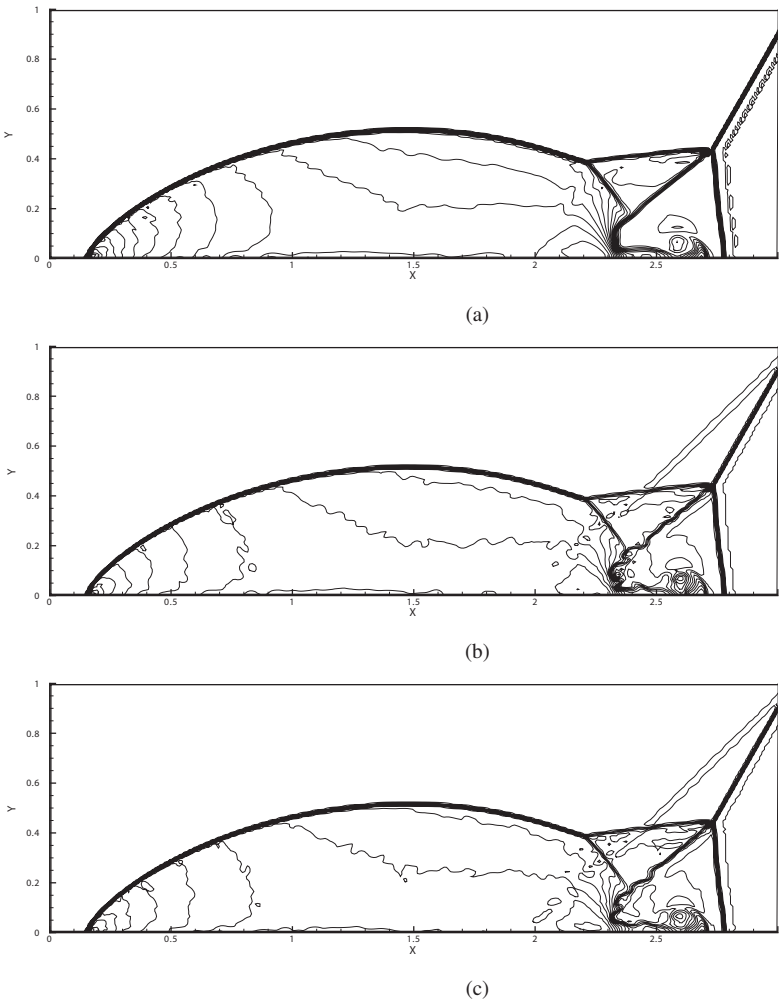

FIGURE 2.17: Numerical results of double Mach reflection at $t = 0.2$ with 100×320 cells by WENO-Z (a), BVD-WENOZ-THINC (b) and BVD-TENO5-THINC (c) method.

by both BVD-WENOZ-THINC and BVD-TENO5-THINC methods. The numerical results on a finer mesh (200×600 mesh) of BVD-WENOZ-THINC and BVD-TENO5-THINC are shown in Fig.2.22. All shocks and vortex structures are well resolved, and the numerical results are comparable to other high-order and less-dissipative methods, such as DG method. It is noted again that the BVD-WENOZ-THINC and BVD-TENO5-THINC methods produce the competitive numerical results for the vortex structures, but on a relatively lower mesh resolution in comparison with existing methods. Consistently, a striking feature in our numerical solution is that even the small disturbances are preseved owing to the reduced numerical dissipation in the BVD-based schemes used in the numerical experiments.

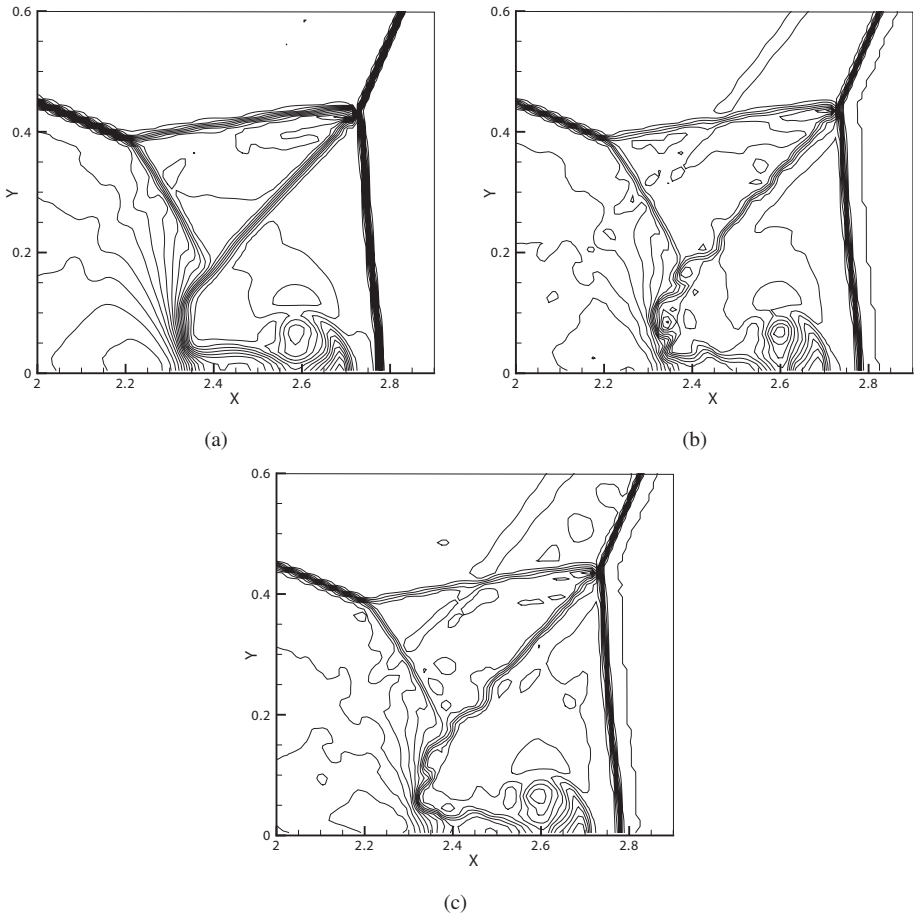

FIGURE 2.18: The Zoomed-in parts of numerical results shown in Fig.2.17. (a): WENO-Z method, (b): BVD-WENOZ-THINC method, (c): BVD-TENO5-THINC method.

2.5 Summary

We have proposed a new guideline to construct high-resolution Godunov type schemes to resolve both smooth and discontinuous solutions. The basic idea, so-called BVD (boundary variation diminishing), is to reconstruct the solution functions so that the jumps at cell boundaries are minimized, which effectively reduces the numerical dissipation in the resulting schemes. The original idea of BVD reconstruction is based on the observation that the development of high order numerical method is the effort to reduce the reconstructed difference at the cell boundaries. The BVD reconstruction automatically realizes the highest possible order of polynomial interpolation for smooth profile, whilst prefers other forms of reconstructions in the presence of discontinuities.

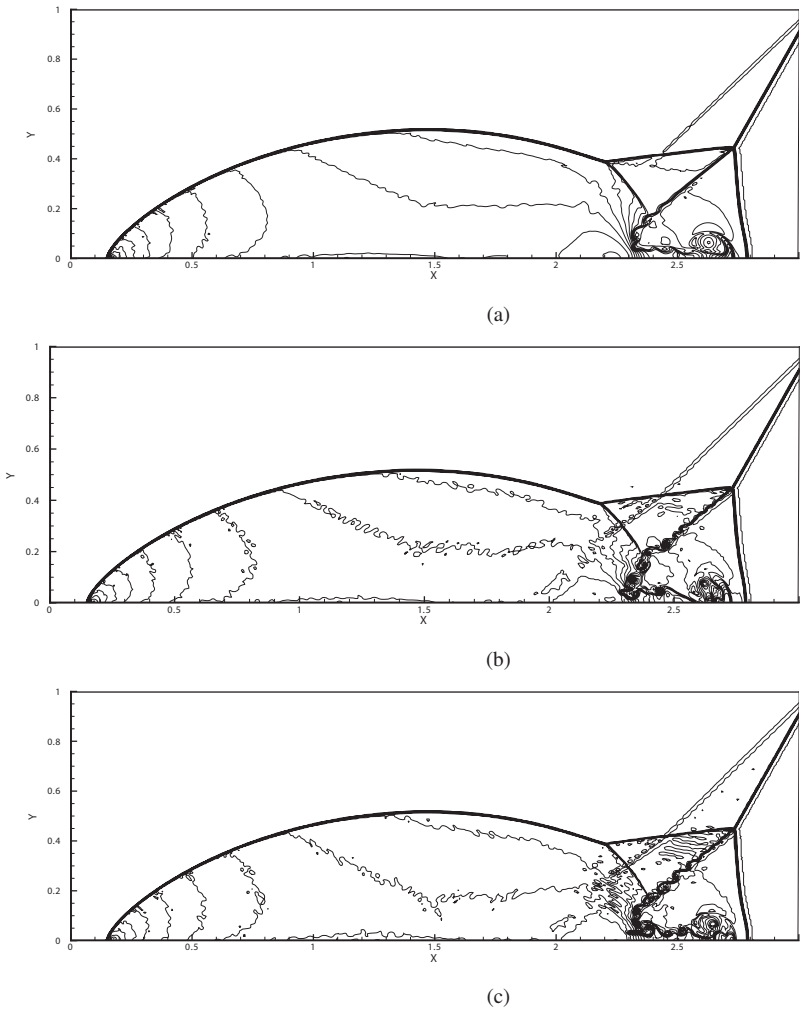

FIGURE 2.19: Numerical results of double Mach reflection at $t = 0.2$ with 200×640 cells by WENO-Z (a), BVD-WENOZ-THINC (b) and BVD-TENO5-THINC (c) method.

As a result, BVD reconstruction mitigates the questionable premiss that discontinuities only appear at cell interfaces in the current paradigm of high-order Godunov schemes.

We have implemented the BVD algorithm with the existing schemes as the building-block schemes, i.e. WENO-Z, TENO5 and THINC schemes. The BVD algorithm provides a reliable switching mechanism to reconstruct the solution function for both smooth profile and discontinuity. For smooth profile, we use the polynomial reconstruction, while for jump discontinuity, we use a step-like function for flux reconstruction. Excellent numerical results have been obtained for both scalar and Euler conservation laws, which show a substantial improvement in comparison with the existing methods

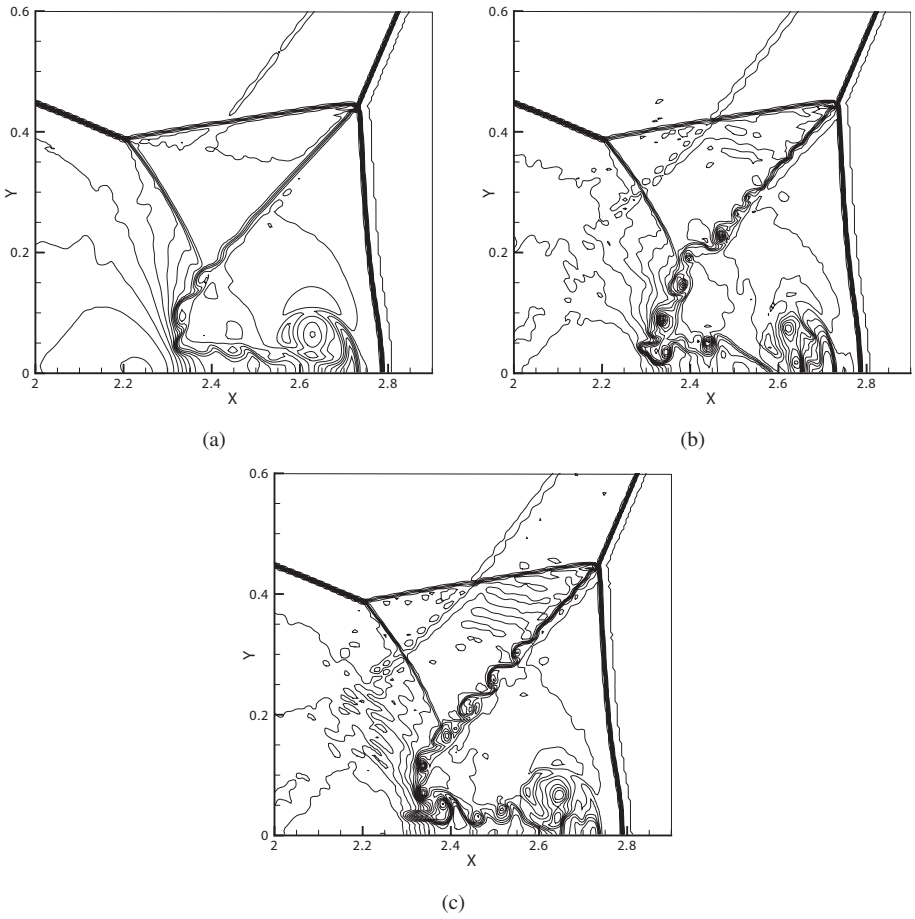

FIGURE 2.20: The Zoomed-in parts of numerical results shown in Fig.2.19. (a): WENO-Z method, (b): BVD-WENOZ-THINC method, (c): BVD-TENO5-THINC method.

including the high-order and less-dissipasive methods. Especially, the BVD reconstruction displays superior performance in dealing with the problems including vortical flow field that is sensible to numerical dissipation. For the numerical method with excessive numerical dissipation, the vortex structure can be easily dissipated under low density mesh. In order to fully resolve the vortex solutions, the mesh with high density is needed for traditional FVM, which will decrease the computational efficiency. Under the same grid, the BVD reconstruction can give the results with more details than traditional FVM.

Not limited to (W/T)ENO and THINC schemes, the BVD concept as a general platform of more profound impact can be used with other candidate reconstructions to further explore high-fidelity schemes for capturing both smooth and discontinuous solutions. A preliminary analysis [1] of the BVD algorithm in the DG-WENO framework shows

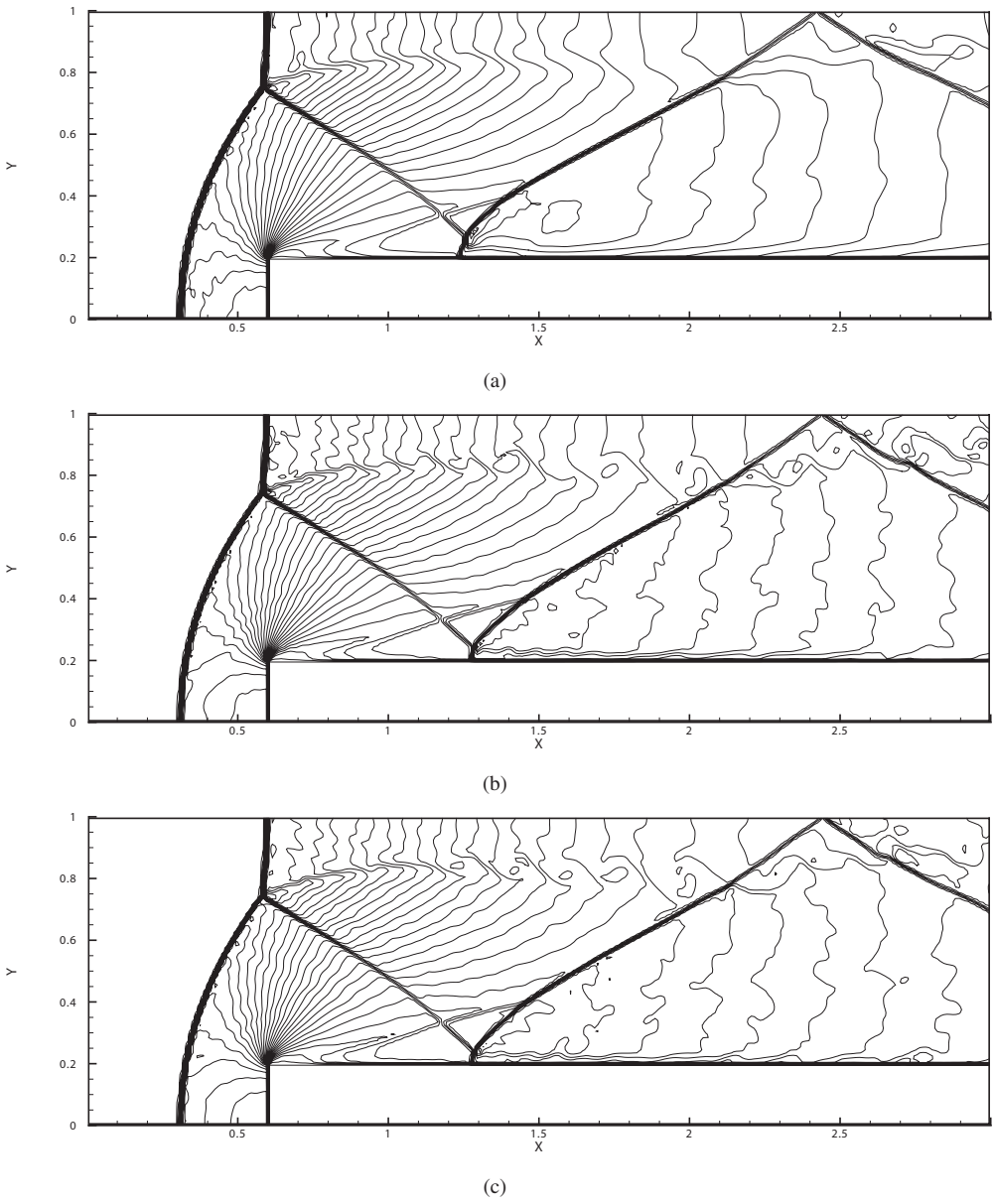

FIGURE 2.21: Numerical results of Mach 3 step test at $t = 0.2$ on a 100×300 mesh. Displayed are the solutions of WENO-Z (top), BVD-WENOZ-THINC (middle) and BVD-WENOZ-TENO5 (bottom) method.

that BVD provides a more reliable switching compared to the prevailing total variation bounded (TVB) switching [61, 64].

For unstructured meshes, high order FVM always needs a large reconstruction stencil. The low order method with better geometrical adaptability generates excessive numerical dissipation that can easily dissipate the resolution for vortical flow field. The BVD reconstruction can efficiently reduce the numerical viscosity for low order reconstruction, which gives a scheme with both high geometrical adaptability and low numerical

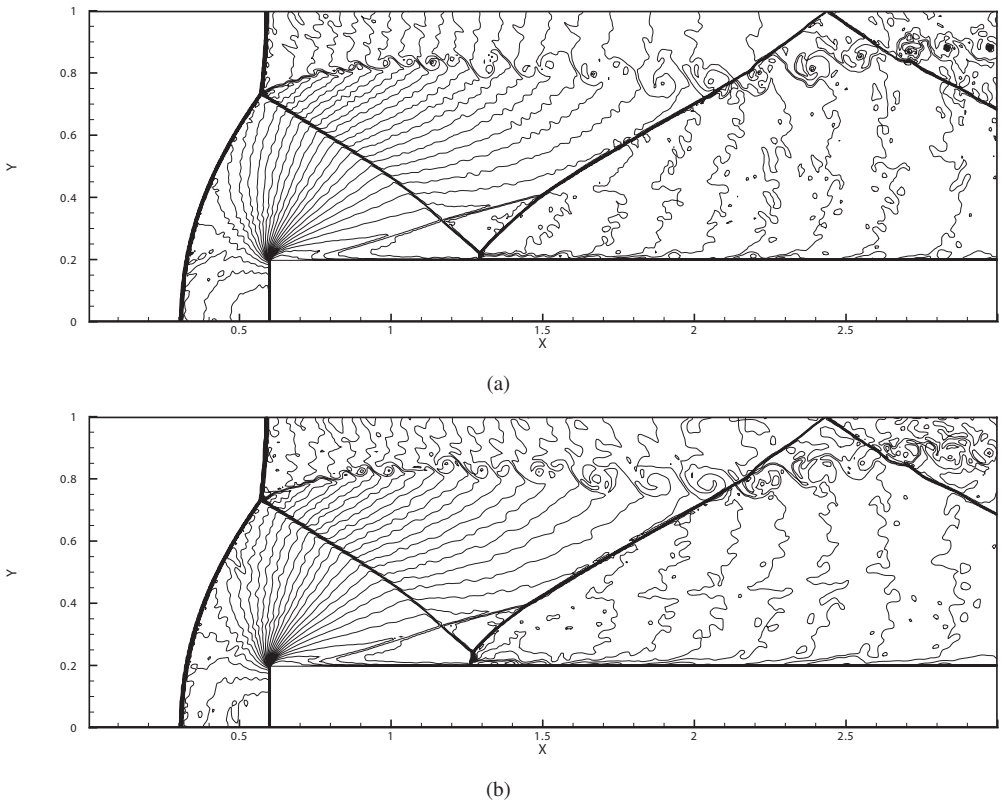

(a)

(b)

FIGURE 2.22: Numerical results of Mach 3 step test at $t = 0.2$ on a 200×600 mesh. Displayed are the solutions of BVD-WENOZ-THINC (top) and BVD-WENOZ-TENO5 (bottom) method.

dissipation. In other words, for low order FVM with better geometrical adaptability such as MUSCL scheme, by using the BVD reconstruction, we can recover the numerical results with the resolution that is comparable to those computed by high order methods. An example of applying BVD principle on unstructured meshes has been presented in [105].

Chapter 3

A Slope Constrained 4th Order Multi-Moment Finite Volume Method with WENO Limiter

3.1 Problem of existing HLR method: Numerical Oscillation

For all exiting HLR methods, the numerical oscillations are unavoidable due to the Gibbs phenomenon [26]. For most HLR method, the polynomial function is used in flux reconstruction, which will inevitably generate the numerical oscillations when the flux profile includes the jump discontinuity. When solving the Euler equations, the oscillation will leave the fields of density or temperature to take unphysical values [33]. Furthermore, the oscillation will bring about the problem in the physical process where a slight disturbance of field variable would change the solution dramatically.

To demonstrate the numerical oscillations, we compute advection equation $u_t + u_x = 0$ with the square wave as initial profile for one period by MCV3 scheme of HLR method. The numerical results along with the exact solution is shown in Fig. 3.1. It can be observed that near the jump discontinuities, the overshoots and undershoots are significant,

about 5% of the discontinuity's height. This can be disastrous in the computation of Euler equations because sometimes the density or pressure can be as low as almost zero, where ever the tiny oscillations can result in the negative value for physical quantity, which can blow up the numerical computation.

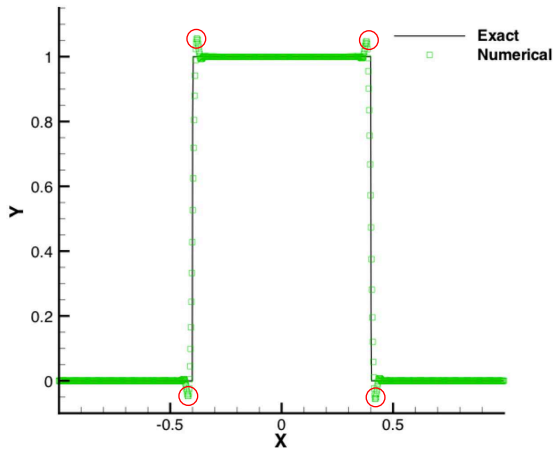

FIGURE 3.1: The simulation of the advection of a square wave by MCV3 method on a 1000-cell mesh. The numerical oscillations are marked by the red circles.

3.2 MMC-FR formulation and 3-point MCV scheme with slope constraint

Being an extension of the FR formulation of Huynh [37], the MMC-FR [102] is briefed at first for completeness in this section. A new scheme is then devised under the MMC-FR framework by adding a slope constraint to the 3-point MCV scheme.

3.2.1 Brief of MMC-FR formulation

We consider the following hyperbolic conservation law

$$\frac{\partial u}{\partial t} + \frac{\partial f}{\partial x} = 0, \tag{3.1}$$

where u is the solution function, and $f(u)$ the flux function.

The computational domain is divided into I non-overlapping cells or elements $\Omega_i = [x_{i-\frac{1}{2}}, x_{i+\frac{1}{2}}], i = 1, 2, \cdots, I$, and K solution points x_{ik}, $k = 1, 2, \cdots, K$, are set over Ω_i where the solution u_{ik}, $k = 1, 2, \cdots, K$, is computed. As shown in the FR formulation of Huynh[37], given a properly approximated numerical flux function $\hat{f}_i(x)$, we can update the solutions within Ω_i by the following point-wise semi-discretised equations at solution points x_{ik},

$$\frac{du_{ik}}{dt} = -\left(\frac{d\hat{f}_i(x)}{dx}\right)_{ik}, \quad k = 1, 2, \cdots, K. \tag{3.2}$$

The above equation (3.2) is of differential form, which covers a wide range of schemes including the collocation method, spectral element method and nodal DG method. The central task left now is how to reconstruct the flux function $\hat{f}_i(x)$. In principle, the way to reconstruct $\hat{f}_i(x)$ makes difference among the numerical schemes.

Given the solution u_{ik} at x_{ik}, $k = 1, 2, \cdots, K$, a piece-wise Lagrange interpolation polynomial of degree $K-1$ for Ω_i reads

$$\tilde{u}_i(x) = \sum_{k=1}^{K} u_{ik}\phi_{ik}(x), \tag{3.3}$$

where $\phi_{ik}(x)$ is the Lagrange basis function,

$$\phi_{ik}(x) = \prod_{l=1, l\neq k}^{K} \frac{x - x_{il}}{x_{ik} - x_{il}}. \tag{3.4}$$

Given flux $f(u)$ as the function of solution u, we have the flux function f_{ik} at the solution points x_{ik}, $k = 1, 2, \cdots, K$, simply by $f_{ik} = f(u_{ik})$. The piece-wisely reconstructed polynomial for flux function is then obtained as

$$\tilde{f}_i(x) = \sum_{k=1}^{K} f_{ik}\phi_{ik}(x), \tag{3.5}$$

which is of degree $K-1$, same as that for the solution function $u_i(x)$.

We call (3.5) the primary reconstruction which is separately constructed over each cell and thus broken from cell by cell. As shown later, the primary reconstruction is not limited to (3.4) or (3.5). Other conditions might be also added so that the resulting scheme have some desired numerical properties. In general, the primary reconstruction cannot be directly used to calculate (3.2). Further modification is required to ensure that the modified numerical flux function $\hat{f}_i(x)$ is at least C^0 continuous at the two ends $x_{i-\frac{1}{2}}$ and $x_{i+\frac{1}{2}}$ of cell Ω_i, which is the necessary condition for numerical conservation and computational stability.

In [102], we demonstrate that the modified flux function, $\hat{f}_i(x)$, can be reconstructed more flexibly with a wider variety of constraint conditions in a more straightforward and intuitive way. The resulting formulation is called multi-moment constrained flux reconstruction (MMC-FR), which provides a platform to devise new schemes. The numerical procedure of MMC-FR to construct the modified flux function $\hat{f}_i(x)$ is summarized as follows.

1. Compute the primary reconstruction for the solution u or flux function $f(u)$ through (3.3) or (3.5) for all cell Ω_i, $i = 1, 2, \cdots, I$.

2. Compute the solution or flux function on the two sides of the cell boundary $x_{i-\frac{1}{2}}$, for example, by $f^L_{i-\frac{1}{2}} = \tilde{f}_{i-1}(x_{i-\frac{1}{2}})$ and $f^R_{i-\frac{1}{2}} = \tilde{f}_i(x_{i-\frac{1}{2}})$, as well as their derivatives $f^{[m]L}_{xi-\frac{1}{2}} = \tilde{f}^{[m]}_{xi-1}(x_{i-\frac{1}{2}}) = \frac{d^m}{dx^m}\left(\tilde{f}_{i-1}(x_{i-\frac{1}{2}})\right)$ and $f^{[m]R}_{xi-\frac{1}{2}} = \tilde{f}^{[m]}_{xi}(x_{i-\frac{1}{2}}) = \frac{d^m}{dx^m}\left(\tilde{f}_i(x_{i-\frac{1}{2}})\right)$ in case they are not continuous and to be used as the constraint conditions;

3. Find the flux function, $f^{\mathcal{B}}_{i-\frac{1}{2}}$, and its derivatives, $f^{[m]\mathcal{B}}_{xi-\frac{1}{2}}$, at the cell boundary by solving

$$\begin{aligned} f^{\mathcal{B}}_{i-\frac{1}{2}} &= \mathrm{Riemann}\left(f^L_{i-\frac{1}{2}}, f^R_{i-\frac{1}{2}}\right), \\ f^{[m]\mathcal{B}}_{xi-\frac{1}{2}} &= \mathrm{DRiemann}\left(f^{[m]L}_{xi-\frac{1}{2}}, f^{[m]R}_{xi-\frac{1}{2}}\right), \end{aligned} \tag{3.6}$$

where "$\mathrm{Riemann}(\cdot\ ,\ \cdot)$" and "$\mathrm{DRiemann}(\cdot\ ,\ \cdot)$" denote the solvers for the Godunov and derivative Riemann problems.

4. The modified flux function $\hat{f}_i(x)$ of degree K' ($K' \geq K$) is then constructed by properly choosing $K'+1$ constraints including the continuity conditions of flux function, as well as its derivatives if needed, at the cell boundaries. Other constraint conditions can be chosen as the point values or derivatives directly computed from the primary flux function $\tilde{f}_i(x)$ at the constraint points inside the mesh cell.

5. Given the modified flux function $\hat{f}_i(x)$, the numerical solutions are updated by solving the semi-discretised equations (3.2) through time integration.

It is noted that there are options for a user to choose for which variable the primary reconstruction is made, such as the conservative variable, the flux function or the characteristic variable in the system equations.

In the MMC-FR formulation, we need to compute the derivatives of the flux function at cell boundaries which are usually discontinuous and need to be evaluated from the primary reconstructions of the neighboring cells. It is generally known as the derivative Riemann problems. The high-order linear and homogeneous derivative Riemann problems are detailed in [84, 85] for the hyperbolic systems. As addressed in [84], since the first-instant plays a leading role in the interaction of the two states, the derivative Riemann problems with the linearization simplifications provide a reasonable accuracy.

The extension of MMC-FR method to two dimensional case on a structured mesh is straightforward through the tensor product of 1D algorithm. We consider the conservation law of (3.7) in two dimensions,

$$\begin{cases} u_t + f(u)_x + g(u)_y = 0, \\ u(x,y,0) = u_0(x,y), \end{cases} \tag{3.7}$$

where $f(u)$ is the flux function in x direction and $g(u)$ in y direction respectively. The flux reconstruction is conducted over each line segment, e.g. for target cell ij, in x direction, we construct the flux function along line segments $\overline{x_{i-\frac{1}{2}}x_{i+\frac{1}{2}}} \bigcap y_{jk},\ k = 1, 2, \cdots, K$, while for y direction the flux function can be obtained by the reconstructions over line segments $\overline{y_{j-\frac{1}{2}}y_{j+\frac{1}{2}}} \bigcap x_{ik},\ k = 1, 2, \cdots, K$. The solution points are

updated from the summation of the spatial derivatives of flux functions for x and y directions.

3.2.2 3-point MCV scheme with slope constraint

We describe the 3-point MCV scheme with slope constraint, referred to as MCV-SC hereafter, as an example of the MMC-FR method. Three solution points x_{ik}, $k = 1, 2, 3$, are used over each cell Ω_i. In the present scheme we locate the solution points respectively at $x_{i1} = x_{i-\frac{1}{2}}$, $x_{i2} = x_i = (x_{i-\frac{1}{2}} + x_{i+\frac{1}{2}})/2$ and $x_{i3} = x_{i+\frac{1}{2}}$. The solutions u_{ik}, $k = 1, 2, 3$, can be updated through the semi-discretized equation (3.2).

It should be noted that because $x_{i1} = x_{i-\frac{1}{2}}$ and $x_{i3} = x_{i+\frac{1}{2}}$ are the two ends of the cell and u_{i1} is shared by cells Ω_{i-1} and Ω_i, i.e. $u_{(i-1)3} = u_{i1} = u_{i-\frac{1}{2}}$, only two of (3.2) need to be computed.

Given the solutions $u_{ik},\ k = 1, 2, 3$, the primary reconstruction is a quadratic Lagrange interpolation built to approximate the flux function, which results in the MCV3 (Multi-moment constrained finite volume method of 3rd order) scheme as shown in [41, 102]. Following the basic idea in [96], we add another constraint condition as the first-order derivative (slope), $f_x^{[1]}(x_i)$, at the cell center and build the primary flux reconstruction as a cubic polynomial $\tilde{f}_i(x)$ from the following conditions,

$$\begin{cases} \tilde{f}_i(x_{i-\frac{1}{2}}) = f(u_{i1}); \\ \tilde{f}_i(x_i) = f(u_{i2}); \\ \tilde{f}_i(x_{i+\frac{1}{2}}) = f(u_{i3}); \\ \tilde{f}_{xi}^{[1]}(x_i) = f_x^{[1]}(x_i). \end{cases} \tag{3.8}$$

Here the first-order derivative $f_x^{[1]}(x_i)$ is obtained from an interpolation that may involve cell Ω_i and its immediate neighbors. For example, a fourth-order approximation is obtained by using the nodal values $f(u_{i\pm\frac{1}{2}})$ and $f(u_{i\pm1})$ from two neighboring cells,

$$f_x^{[1]}(x_i) = \frac{8f(u_{i+\frac{1}{2}}) - 8f(u_{i-\frac{1}{2}}) + f(u_{i-1}) - f(u_{i+1})}{6\Delta x_i}. \tag{3.9}$$

Using $f_x^{[1]}(x_i)$ as a constraint condition, we can make the scheme to have the desired numerical properties. A 4th-order scheme can be constructed if approximation (4.7) is used in (5.14). We refer it as the MCV-SC4 (MCV-SC of 4th order).

As mentioned before, interpolation $\tilde{f}_i(x)$ cannot be immediately used in (3.2) to update the nodal solutions, but is used to find the left and right-side derivative values of the flux function at the cell boundaries. It is observed from (5.14) that the primary reconstruction $\tilde{f}(x)$ is continuous at the cell boundary, i.e. $\tilde{f}_{i-1}(x_{i-\frac{1}{2}}) = \tilde{f}_i(x_{i-\frac{1}{2}}) = f(u_{i-\frac{1}{2}})$.

In the present scheme, we impose the following constraint conditions to the modified flux reconstruction $\hat{f}_i(x)$ in terms of both flux function and its first-order derivative, same as the MCV3 scheme shown in [102],

$$\begin{cases} \hat{f}_i(x_{i\pm\frac{1}{2}}) = f_i(u_{i\pm\frac{1}{2}}), \\ \hat{f}_{xi}^{[1]}(x_{i\pm\frac{1}{2}}) = f_x^{[1]B}(x_{i\pm\frac{1}{2}}), \end{cases} \tag{3.10}$$

where $f_i(u_{i\pm\frac{1}{2}})$ can be calculated directly with $u_{i\pm\frac{1}{2}}$ updated every time step, and $f_x^{[1]B}(x_{i\pm\frac{1}{2}})$ are the approximations of the first-order derivatives of the flux function at cell boundaries, which need to be computed as the solutions of the Derivative Riemann problems based on the left and right-side values at the cell boundaries as discussed before.

Constraint condition (3.10) yields a Hermite interpolation to determine the modified flux function which is written in a cubic polynomial as,

$$\begin{cases} \hat{f}_i(x) = \left(2\left(f_i(u_{i-\frac{1}{2}}) - f_i(u_{i+\frac{1}{2}})\right) + \Delta x_i\left(f_x^{[1]B}(x_{i-\frac{1}{2}}) + f_x^{[1]B}(x_{i+\frac{1}{2}})\right)\right)\xi^3 \\ \qquad + \left(3\left(f_i(u_{i+\frac{1}{2}}) - f_i(u_{i-\frac{1}{2}})\right) - \Delta x_i\left(2f_x^{[1]B}(x_{i-\frac{1}{2}}) + f_x^{[1]B}(x_{i+\frac{1}{2}})\right)\right)\xi^2 \\ \qquad + \Delta x_i f_x^{[1]B}(x_{i-\frac{1}{2}})\xi + f_i(u_{i-\frac{1}{2}}), \end{cases} \tag{3.11}$$

where $\xi = (x - x_{i-\frac{1}{2}})/\Delta x_i$.

The derivatives of the modified flux function at the solution points are obtained as

$$\begin{cases} \left(\dfrac{d\hat{f}_i(x)}{dx}\right)_{i1} = f_x^{[1]B}(x_{i-\frac{1}{2}}); \\ \left(\dfrac{d\hat{f}_i(x)}{dx}\right)_{i2} = \dfrac{3}{2\Delta x_i}\left(f_i(u_{i+\frac{1}{2}}) - f_i(u_{i-\frac{1}{2}})\right) - \dfrac{1}{4}\left(f_x^{[1]B}(x_{i-\frac{1}{2}}) + f_x^{[1]B}(x_{i+\frac{1}{2}})\right); \\ \left(\dfrac{d\hat{f}_i(x)}{dx}\right)_{i3} = f_x^{[1]B}(x_{i+\frac{1}{2}}). \end{cases} \tag{3.12}$$

The solutions are then immediately computed by (3.2) with a proper time integration algorithm. We note here again that the boundary values u_{i1} and u_{i3} are shared by the two neighboring cells, and only following two semi-discretized equations need to be solved for each cell,

$$\begin{cases} \dfrac{du_{i1}}{dt} = f_x^{[1]B}(x_{i-\frac{1}{2}}); \\ \dfrac{du_{i2}}{dt} = \dfrac{3}{2\Delta x_i}\left(f_i(u_{i+\frac{1}{2}}) - f_i(u_{i-\frac{1}{2}})\right) - \dfrac{1}{4}\left(f_x^{[1]B}(x_{i-\frac{1}{2}}) + f_x^{[1]B}(x_{i+\frac{1}{2}})\right). \end{cases} \tag{3.13}$$

As discussed in [11, 51], the MCV method is more computationally efficient in comparison with DG as well as other HLR based schemes regarding both memory requirement and CPU cost.

3.3 WENO limiter

In this section, we present the details of the new WENO limiter for 3-point MCV scheme. The resulting scheme is called MCV-WENO4 (Multi-moment Constrained finite Volume with WENO limiter of 4th order) method. The reason why our new WENO limiter is applied for 3-points MCV scheme can be illustrated from the following three parts. First of all, three points MCV (MCV-3) method is the most basic version of MCV-type scheme, and it is a third-order accuracy scheme that averagely uses only two DOFs inside each cell. Second, for unstructured meshes, the third order accuracy scheme can achieve a balance between accuracy and computational robustness. Last but not least,

for our new $4th$ order WENO limiter, under the three points MCV scheme, the width of the reconstruction stencil can be minimized.

The basic idea of this WENO limiter is to reconstruct the 1st order derivative at the cell center for the MCV-SC scheme described above. The WENO reconstructed 1st order derivative is used in (5.14) to construct the primary flux reconstruction locally within each cell. Then, the modified flux reconstruction procedure of MCV-SC scheme is applied without any change. It is noted that the present scheme has much less dissipation error to the smooth solution. Unlike other existing WENO limiters for the DG method, the present WENO projection applies to all cells not just limited to the so-called "trouble cells" which is identified by the TVB criterion and involves artificial parameter. Shown in the numerical results, the smooth solutions are accurately reproduced without significant numerical dissipation.

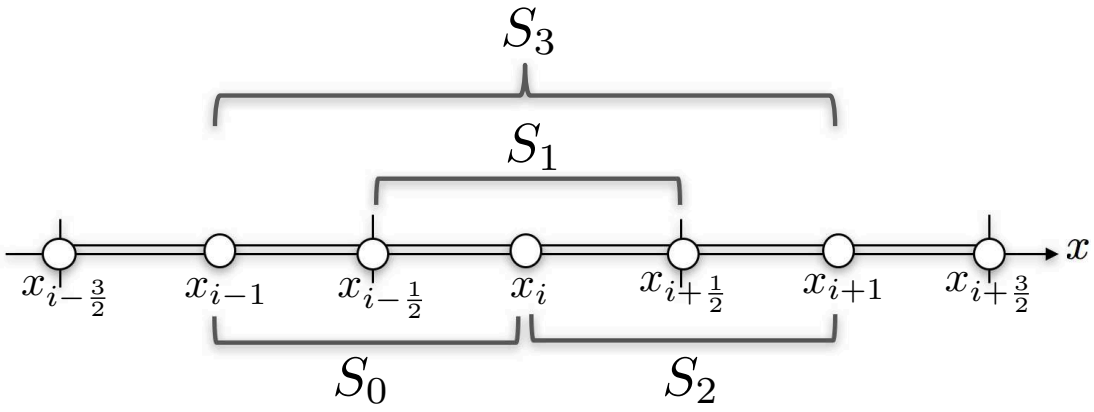

FIGURE 3.2: Reconstruction stencils for the new WENO limiter.

3.3.1 WENO reconstruction for first-order derivative: Scalar case

We describe the WENO reconstruction of conservative variable $u(x)$ for cell Ω_i. For MCV-WENO4 scheme, we have three small stencils $S_j = \left\{x_{i-1+\frac{j}{2}}, x_{i-\frac{1}{2}+\frac{j}{2}}, x_{i+\frac{j}{2}}\right\}$, $j = 0, 1, 2$, and one large stencil $S_3 = \left\{x_{i-1}, x_{i-\frac{1}{2}}, x_i, x_{i+\frac{1}{2}}, x_{i+1}\right\}$. The distribution of the stencil is shown in Fig.4.1. Then, we can construct a 2nd-degree polynomial through the interpolation of three PVs inside each small stencil. Here the polynomial is denoted by $q_j(x)$ associated with each of the stencils $S_j,\ j = 0, 1, 2$. The 1st order spatial derivative at the center of cell Ω_i can be approximated with second order accuracy respectively

from the derivative of the reconstructed polynomial in each stencil as

$$\begin{aligned} q_{x0}^{[1]}(x_i) &= \frac{3u_i + u_{i-1} - 4u_{i-\frac{1}{2}}}{\Delta x_i}, \\ q_{x1}^{[1]}(x_i) &= \frac{u_{i+\frac{1}{2}} - u_{i-\frac{1}{2}}}{\Delta x_i}, \\ q_{x2}^{[1]}(x_i) &= -\frac{3u_i + u_{i+1} - 4u_{i+\frac{1}{2}}}{\Delta x_i}. \end{aligned} \tag{3.14}$$

Meanwhile, we have a fourth-degree polynomial reconstruction denoted by $Q_i(x)$ in stencil S_3 which has the first-order derivative at cell center as

$$Q_{xi}^{[1]}(x_i) = \frac{8u_{i+\frac{1}{2}} + u_{i-1} - 8u_{i-\frac{1}{2}} - u_{i+1}}{6\Delta x_i}. \tag{3.15}$$

Given (4.36), we can re-write the 1st order derivative at the cell center with $4th$ order accuracy by the linear combination of the three 2nd order approximations, i.e.

$$Q_x^{[1]}(x_i) = \sum_{j=0}^{2} \gamma_j q_{xj}^{[1]}(x_i), \tag{3.16}$$

where

$$\gamma_0 = \frac{1}{6}, \quad \gamma_1 = \frac{2}{3}, \quad \gamma_2 = \frac{1}{6}. \tag{3.17}$$

Following the spirit of existing WENO schemes, instead of (4.38) nonlinear weighting can be designed to effectively suppress spurious oscillation near discontinuity and maintain numerical accuracy in smooth region.

We define the smoothness indicator by

$$\beta_j = \sum_{l=1}^{2} \int_{x_{i-\frac{1}{8}}}^{x_{i+\frac{1}{8}}} \Delta x_i^{2l-1} \left(\frac{\partial^l q_j(x)}{\partial x^l} \right)^2 dx, \quad j = 0, 1, 2; \tag{3.18}$$

which measures the smoothness of the polynomial function in the target area. Compared with the smoothness indicator of the conventional WENO scheme, we modify the upper and lower limits of integral from $x_{i-\frac{1}{2}}$ and $x_{i+\frac{1}{2}}$ to $x_{i-\frac{1}{8}}$ and $x_{i+\frac{1}{8}}$ in order to match the compact WENO reconstruction stencil used in the present scheme.

Regarding the WENO reconstruction, some successive works have been conducted to improve the accuracy of the classic WENO [45] by using different nonlinear weights and smoothness measurements in the WENO reconstruction, such as the WENO-M [32] and WENO-Z [6] schemes. Shen and Zha [69, 70] provided a detail analysis how these scheme behave over a transition cell where smooth region and discontinuity connect, and proposed an optimal estimation of the first-order derivative for the transition cell. In the present study, we adopt the scheme in [69] and calculate the nonlinear weights $\omega_j,\ j = 0, 1, 2$, as the functions of β_j and γ_j by

$$\{\omega_0, \omega_1, \omega_2\} = \begin{cases} \left\{\frac{1}{3}, \frac{2}{3}, 0\right\} & \text{if } \tau_4^0 \le \min(\beta_j) \text{ and } \tau_4^1 > \min(\beta_j), \\ \left\{0, \frac{2}{3}, \frac{1}{3}\right\} & \text{if } \tau_4^0 > \min(\beta_j) \text{ and } \tau_4^1 \le \min(\beta_j), \\ \left\{\omega_0^Z, \omega_1^Z, \omega_2^Z\right\} & \text{otherwise;} \end{cases} \tag{3.19}$$

where

$$\tau_4^0 = |\beta_0 - \beta_1|, \quad \tau_4^1 = |\beta_1 - \beta_2|, \tag{3.20}$$

and $\left\{\omega_0^Z, \omega_1^Z, \omega_2^Z\right\}$ are the nonlinear weights obtained from the WENO-Z scheme[6], which are given by

$$\omega_j^Z = \frac{\alpha_j^Z}{\sum_{k=0}^2 \alpha_k^Z}, \quad \alpha_j^Z = \gamma_j \left(1 + \frac{\tau_5}{\beta_j + \epsilon}\right), \quad j = 0, 1, 2. \tag{3.21}$$

where ϵ is equal to 10^{-40} and $\tau_5 = |\beta_2 - \beta_0|$.

It is noted that our numerical experiments don't show noticeable difference between (3.19) and the WENO-Z scheme.

Finally, we can get the WENO reconstructed first order derivative $\tilde{Q}_x^{[1]}(x_i)$ by

$$\tilde{Q}_x^{[1]}(x_i) = \sum_{j=0}^{2} \omega_j q_{xj}^{[1]}(x_i). \tag{3.22}$$

We assume that the WENO reconstruction is conducted for the conservative variable, and summarize the MCV-WENO4 method as followings:

1. Get the 1st order derivative at the center of the target cell, $q_{xj}^{[1]}(x_i)$, $j = 0, 1, 2$, by (4.35) for each small stencil;
2. Calculate the smoothness indicator for each stencil by (4.39);
3. Obtain the nonlinear weights for each stencil using (3.19);
4. Compute the modified 1st order derivative at cell center by (4.41);
5. Replace the 1st order derivative at cell center $f_x^{[1]}(x_i)$ in (5.14) by that computed from the WENO reconstruction;
6. Get the primary reconstruction from the constraint conditions (5.14);
7. Repeat the rest steps of the MCV-SC scheme.

For multi-dimensional structured grids which can be mapped to a Cartesian grid, the WENO reconstruction is carried out along the line segment in each direction separately with the 1D algorithm given above.

3.3.2 WENO reconstruction for first-order derivative: Euler equations

The 1D Euler equations for ideal gas are given by

$$\mathbf{U}_t + \mathbf{F}(\mathbf{U})_x = 0, \tag{3.23}$$

where

$$\mathbf{U} = \begin{pmatrix} u^{(1)} \\ u^{(2)} \\ u^{(3)} \end{pmatrix} = \begin{pmatrix} \rho \\ \rho v \\ E \end{pmatrix}, \quad \mathbf{F}(\mathbf{U}) = \begin{pmatrix} f^{(1)} \\ f^{(2)} \\ f^{(3)} \end{pmatrix} = \begin{pmatrix} \rho v \\ \rho v^2 + p \\ v(E+p) \end{pmatrix}. \tag{3.24}$$

Here ρ is density, v velocity, p pressure and E total energy. We use the equation of state (EOS) of ideal gas, i.e.

$$E = \frac{p}{\gamma - 1} + \frac{1}{2}\rho v^2, \tag{3.25}$$

where $\gamma = 1.4$. The Jacobian matrix of the flux function is defined by $\mathbf{A} = \partial\mathbf{F}/\partial\mathbf{U}$. The explicit form of Jacobian matrix will be given in Appendix A.

For the Euler system, the WENO reconstruction is carried out in terms of the characteristic variables. To this end, the vector of conservative variables is mapped firstly to the characteristic variables $\mathbf{W} = (w^{(1)}, w^{(2)}, w^{(3)})^T$ using the left eigenvectors of the Jacobian matrix $\overline{\mathbf{A}}_{i+\frac{1}{2}}$ computed from Roe averaging,

$$\mathbf{W}_j = \overline{\mathbf{R}}^{-1}_{i+\frac{1}{2}}\mathbf{U}_j, \quad j = i-1,\ i-\frac{1}{2},\ i,\ i+\frac{1}{2},\ i+1, \tag{3.26}$$

where $\overline{\mathbf{R}}^{-1}_{i+\frac{1}{2}}$ is a 3×3 matrix whose rows are the left eigenvectors of Jacobian matrix $\overline{\mathbf{A}}_{i+\frac{1}{2}}$. The Roe averaged expressions of Jacobian matrix and its corresponding eigenvectors can be found in Appendix B. Then, all the WENO reconstruction is conducted for the characteristic variables $\mathbf{W}_j$ to get the 1st order derivative of characteristic variables, $\mathbf{W}^{[1]}_{xi}$, at the cell center. After that, we project the derivative of characteristic variable back to the conservative variables by

$$\mathbf{U}^{[1]}_{xi} = \overline{\mathbf{R}}_{i+\frac{1}{2}}\mathbf{W}^{[1]}_{xi}, \tag{3.27}$$

where $\overline{\mathbf{R}}_{i+\frac{1}{2}}$ is a 3×3 matrix of which the columns are the right eigenvectors of Jacobian matrix $\overline{\mathbf{A}}_{i+\frac{1}{2}}$. After obtaining $\mathbf{U}^{[1]}_{xi}$, we make the primary reconstruction $\tilde{\mathbf{U}}_i(x)$ from the constraints (5.14) component-wisely for each conservative variable. Then, the 1st order derivative at cell boundary $x_{i+\frac{1}{2}}$ can be obtained from the reconstructed solution function by $\mathbf{U}^{[1]L}_{xi+\frac{1}{2}} = \frac{d}{dx}\tilde{\mathbf{U}}_i(x_{i+\frac{1}{2}})$. The derivative of the corresponding flux function is then computed by

$$\mathbf{F}^{[1]L}_{xi+\frac{1}{2}} = \overline{\mathbf{A}}_{i+\frac{1}{2}}\mathbf{U}^{[1]L}_{xi+\frac{1}{2}}. \tag{3.28}$$

It is noted that we use the Roe-averaged Jacobian matrix at the right boundary $x_{i+\frac{1}{2}}$ of cell Ω_i in the characteristic field decomposition. In this case, the WENO modified first order derivative at the cell center is used to compute the 1st order derivative at the right boundary $x_{i+\frac{1}{2}}$. When calculating the 1st order derivative at the left boundary $x_{i-\frac{1}{2}}$, we use the Roe-averaged Jacobian matrix, $\overline{\mathbf{A}}_{i-\frac{1}{2}}$, at the left boundary, which results in

$\mathbf{U}^{[1]R}_{xi-\frac{1}{2}} = \frac{d}{dx}\tilde{\mathbf{U}}_i(x_{i-\frac{1}{2}})$ and

$$\mathbf{F}^{[1]R}_{xi-\frac{1}{2}} = \overline{\mathbf{A}}_{i-\frac{1}{2}}\mathbf{U}^{[1]R}_{xi-\frac{1}{2}}. \tag{3.29}$$

Having obtained the left and right values of the derivatives of the conservative variables and flux functions at cell boundaries, the numerical approximation of the flux derivative is computed by the Roe approximate Riemann solver [67], i.e.

$$\mathbf{F}^{[1]B}_{xi+\frac{1}{2}} = \frac{1}{2}\left(\mathbf{F}^{[1]L}_{xi+\frac{1}{2}} + \mathbf{F}^{[1]R}_{xi+\frac{1}{2}} - \overline{\mathbf{A}}_{i+\frac{1}{2}}\left(\mathbf{U}^{[1]R}_{xi+\frac{1}{2}} - \mathbf{U}^{[1]L}_{xi+\frac{1}{2}}\right)\right). \tag{3.30}$$

We have so far described the spatial discretization and obtained the semi-discretized ordinary differential equations (ODEs) with respect to time. In the numerical tests presented in this chapter, we use the five stage fourth order SSP Runge-Kutta method (SSPRK(5,4)) developed by Spiteri and Ruuth [28, 79].

3.4 Analysis of the computational efficiency for MCV-WENO4 scheme.

The computational efficiency of our scheme can be illustrated from the following three parts. Firstly, we define a solution point at the cell boundary which is shared by two cells in the space discretization of our scheme. This property can help us reduce the number of DOF while keeping the high order accuracy. Secondly, compared with original DG scheme, our scheme is algorithmically simpler and doesn't include any numerical quadrature. Last, the implementation of the WENO limiter is quite efficient because the WENO limiter is designed to reconstruct the first-order derivative at the cell center, which can be directly used in the primary interpolation of MCV-SC scheme.

To give a quantitative measurement, we evaluate the computational time of the advection of a square wave on a 1000-cell mesh after 10 periods (with the same initial condition of Example 3.2 in this chapter) by using the MCV-WENO4 scheme and MCV-WENO4 scheme without WENO limiting (i.e.the MCV-SC4 scheme). We get the following results

$$\begin{cases} \text{Time taken by MCV} - \text{WENO4 scheme} : 4.75\text{s} \\ \text{Time taken by MCV} - \text{SC4 scheme} : 3.95\text{s} \end{cases} \tag{3.31}$$

We can see that the computational time only increases about 20% after the implementation of the WENO limiting projection.

We also analyze the computational efficiency in terms of the operation counts. Here we count the operations using the same method as used in Section 2.3. The operation counts of the MCV-SC and MCV-WENO4 scheme are given in Table 3.1. From the summation of the operations, we find that the 4th order WENO limiter brings in about 39.2% extra computation burden.

TABLE 3.1: Operation Counts of Different Schemes.

Operation	MCV-SC scheme	MCV-WENO4 scheme
if logic	6	6
+,-,*,ABS(x)	61	103
/	13	16
Summation	152.8	212.8

3.5 Numerical experiments

In this section, we give the numerical results for some widely used benchmark tests to illustrate the performance of the MCV-WENO4 method presented in this chapter. The largest allowable CFL number for MCV-WENO4 scheme with the SSP Runge-Kutta method (SSPRK(5,4)) is 0.6. Here we use CFL$= 0.4$ in all numerical tests presented here.

3.5.1 1D linear advection equation

In this subsection, the numerical tests to advect the 1D profile are computed by the MCV-WENO4 method with the linear advection equation defined by

$$u_t + u_x = 0. \tag{3.32}$$

Example 3.1. **Accuracy test.** For this test, we use the grid refinement to check the convergence rate of our scheme. The initial smooth distribution is given as

$$u(x, 0) = \sin(\pi x), \quad x \in [-1, 1]. \tag{3.33}$$

The grid is refined by doubling the grid number for the computational domain, and the

TABLE 3.2: Numerical errors and convergence rate for 1D advection equation, $t = 2.0$.

N	MCV-SC4 scheme				MCV-WENO4 scheme			
	L_1 error	Order	L_∞	Order	L_1 error	Order	L_∞	Order
10	7.45e-04		1.15e-03		7.60e-04		1.31e-03	
20	4.94e-05	3.91	7.65e-05	3.91	4.95e-05	4.05	7.72e-05	4.08
40	3.12e-06	3.99	4.88e-06	3.97	3.12e-06	3.98	4.88e-06	3.98
80	1.96e-07	3.99	3.07e-07	3.99	1.96e-07	3.99	3.07e-07	3.99
160	1.23e-08	4.00	1.92e-08	4.00	1.23e-08	4.00	1.92e-08	4.00
320	7.67e-10	4.00	1.20e-09	4.00	7.67e-10	4.00	1.20e-09	4.00

L_1 errors and L_∞ errors at $t = 2.0$ (after one period) are calculated with different grid resolutions. We show the numerical errors and the convergence rate for MCV-WENO4 scheme as well as MCV-SC4 scheme in Table 4.4. We can see that our scheme uniformly converges to 4th order accuracy. We also notice that the new WENO limiter can maintain not only the convergence rate but also the magnitude of the errors of the original MCV-SC4 scheme.

Example 3.2. **Advection of a square wave.** This test is used to verify the ability of the MCV-WENO4 scheme to capture the jump discontinuities. The initial profile is set as

$$u(x,0)=\begin{cases}1, & \text{when}|\text{x}|\leqslant 0.4,\\ 0, & \text{otherwise.}\end{cases} \tag{3.34}$$

In Fig. 4.2, we show the numerical solution by the open squares which is computed by the MCV-WENO4 scheme with 200 cells over $[-1,1]$ at $t=2.0$ (after one period). We can clearly see that after one period, the numerical solution doesn't cause spurious oscillations in the vicinity of the jump discontinuities located at $x=0.4$ and $x=-0.4$.

Example 3.3. **Jiang and Shu's test.** This test was proposed in [45]. Here we use it to evaluate the ability of the MCV-WENO4 scheme in resolving both discontinuities and smooth solutions. The initial profile is set by

$$u(x,0)=\begin{cases}\dfrac{1}{6}\left(G(x,\beta,z-\delta)+G(x,\beta,z+\delta)+4G(x,\beta,z)\right), & -0.8\leqslant x\leqslant -0.6,\\ 1, & -0.4\leqslant x\leqslant -0.2,\\ 1-|10(x-0.1)|, & 0.0\leqslant x\leqslant 0.2,\\ \dfrac{1}{6}\left(F(x,\alpha,a-\delta)+F(x,\alpha,a+\delta)+4F(x,\alpha,a)\right), & 0.4\leqslant x\leqslant 0.6,\\ 0, & \text{otherwise,}\end{cases} \tag{3.35}$$

where the computation domain is $[-1,1]$. The function F and G is defined by

$$G(x,\beta,z)=\exp\left(-\beta(x-z)^2\right), F(x,\alpha,a)=\sqrt{\max(1-\alpha^2(x-a)^2,0)}, \tag{3.36}$$

and the coefficients to determine the initial profile are given by

$$a=0.5,\ z=0.7,\ \delta=0.005,\ \alpha=10.0,\ \beta=\log 2/(36\delta^2). \tag{3.37}$$

The numerical solution computed over a 200-cell mesh after one period ($t=2.0$) is shown in Fig. 4.3. Here we use the periodic boundary condition. The numerical results

show that the MCV-WENO4 scheme can effectively suppress the oscillations near the discontinuities while keeping the high order accuracy for a smooth profile.

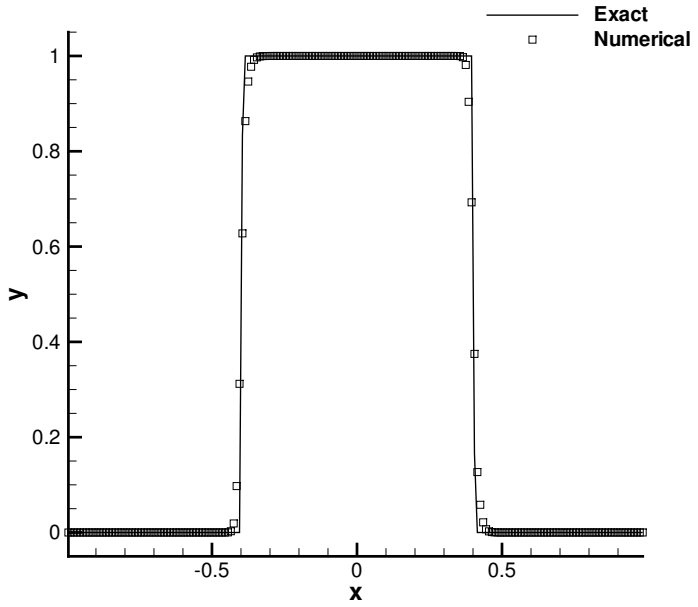

FIGURE 3.3: Advection of a square wave after one period (t=2.0) with 200 grid cells. The solid line indicates the exact solution and the open squares the numerical solution.

3.5.2 1D inviscid Burgers' equation

In this subsection, we consider the 1D inviscid Burgers' equation

$$u_t + \left(\frac{u^2}{2}\right)_x = 0. \tag{3.38}$$

In the examples of the 1D inviscid Burgers equation, the derivative Riemann problem is computed by a pure upwinding scheme at the cell boundary $x_{i+\frac{1}{2}}$ as

$$f^{[1]}_{xi+\frac{1}{2}} = \frac{1}{2}\left(f^{[1]L}_{xi+\frac{1}{2}} + f^{[1]R}_{xi+\frac{1}{2}} - \mathrm{sgn}(\alpha_{i+\frac{1}{2}})(f^{[1]L}_{xi+\frac{1}{2}} + f^{[1]R}_{xi+\frac{1}{2}})\right), \tag{3.39}$$

where $\alpha_{i+\frac{1}{2}} = \dfrac{\bar{u}_i + \bar{u}_{i+1}}{2}$, and $\bar{u}_i$ is the integrated average value for cell Ω_i. The WENO interpolation is performed in terms of the flux function $f(u) = \dfrac{u^2}{2}$.

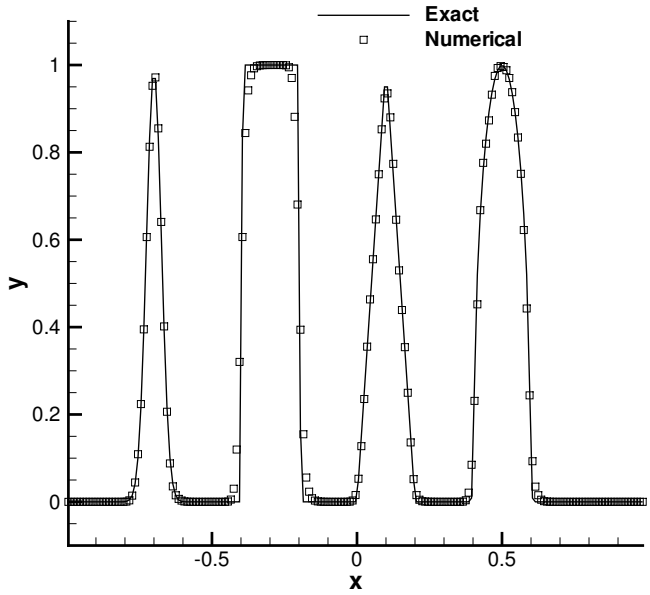

FIGURE 3.4: Numerical results of Jiang and Shu's linear advection test at $t = 2.0$ with 200 grid cells.

TABLE 3.3: Numerical errors and convergence rate for 1D Burgers equation at $t = 1/(2\pi)$.

N	L_1 error	Order of Accuracy	L_∞ error	Order of Accuracy
40	1.11e-05		9.03e-05	
80	8.13e-07	3.86	7.37e-06	3.61
160	5.61e-08	3.86	5.33e-07	3.79
320	3.79e-09	3.89	3.61e-08	3.88
640	2.52e-10	3.91	2.35e-09	3.94

Example 3.4. **Accuracy test.** This test starts with a smooth initial condition, $u(x, 0) = 0.5 + \sin(\pi x)$. The exact solution remains smooth up to $T = 1.0/\pi$, and then a moving shock and a rarefaction wave develops. To evaluate the order of accuracy in respect to grid refinement, we run computation to $t = 0.5/\pi$, and calculate the L_1 and L_∞ errors with different grid resolutions. A periodic boundary condition is imposed and our computation domain is set to be $[0, 2]$. The numerical errors and convergence rate are shown in Table 4.8.

We see again that the MCV-WENO4 scheme uniformly converges up to 4th-order accuracy for this nonlinear test. Due to the interaction between the characteristic lines in Burgers eqution, the profiles of the numerical solutions are changing with the time.

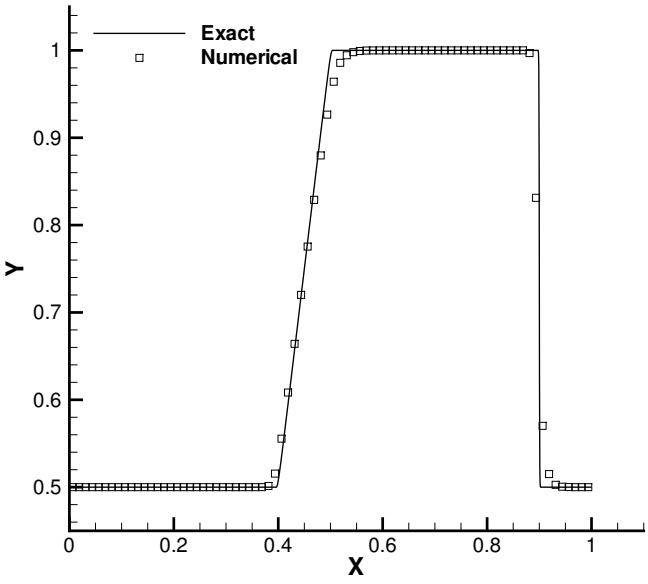

FIGURE 3.5: Numerical results of Burgers equation with a shock and rarefaction at $t = 0.2$ with 80 cells.

Thus, the accuracy test for Burgers equation can help us validate the time-depending accuracy of our scheme.

Example 3.5. **Test with shock.** This test for 1D inviscid Burgers equation includes both shock and rarefaction wave. The initial profile is given by

$$u(x,0) = \begin{cases} 1, & 0.3 \leqslant x \leqslant 0.75, \\ 0.5, & \text{otherwise}. \end{cases} \tag{3.40}$$

The numerical solutions at $t = 0.2$ is displayed in Fig. 4.8. We can see that the numerical solution well resolves the shock wave without spurious oscillation, as well as the expansion wave without significant dissipation.

3.5.3 Buckley-Leverett equation

We show in this subsection the numerical solutions of the Buckley-Leverett equation,

$$u_t + \left(\frac{u^2}{u^2 + (1-u)^2} \right)_x = 0. \tag{3.41}$$

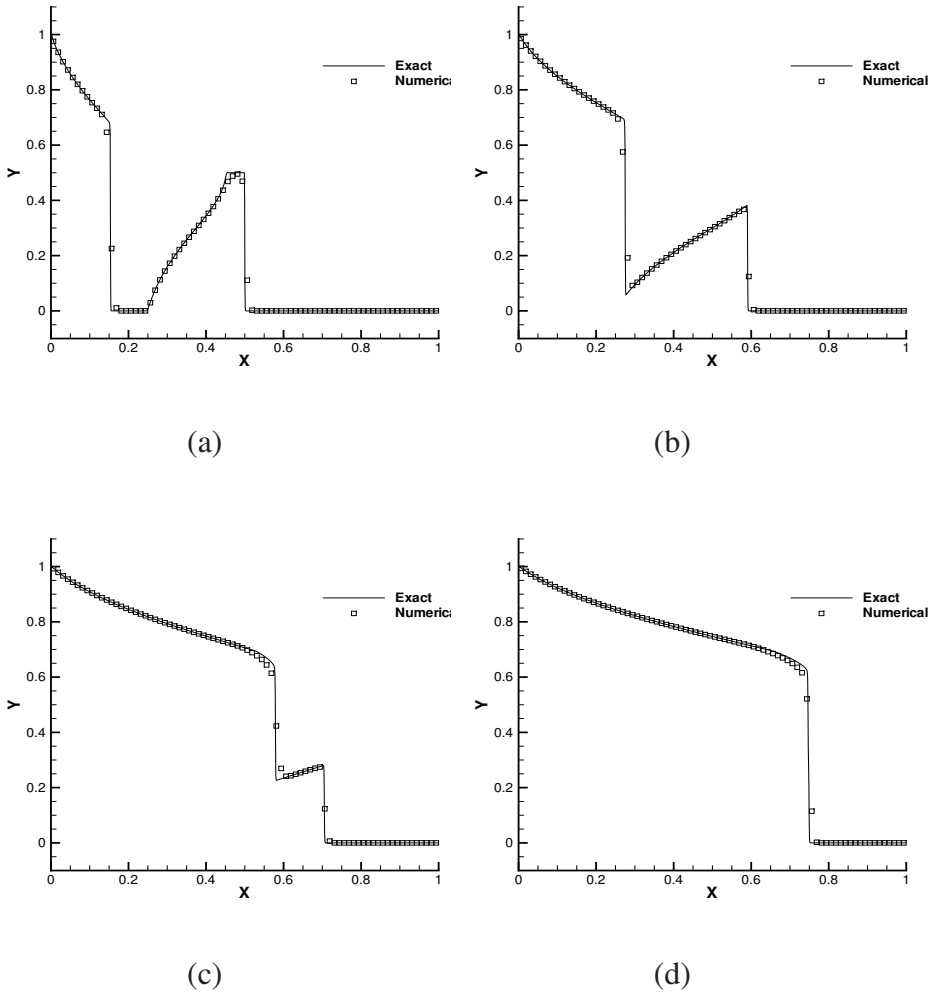

FIGURE 3.6: Numerical results of 1D Buckley-Leverett equation at (a) $t = 0.1$, (b) $t = 0.2$, (c) $t = 0.4$, (d) $t = 0.5$ with 80 cells.

This equation was derived by Buckley & Leverett in [8] with the assumption that the relative permeability functions are quadratic [78]. The upwinding scheme Eq.(3.39) is used as the approximate solver for the derivatives of the flux function at cell boundaries.

Example 3.6. **Two pulse interaction test.** Initially, we set the following conditions

$$u(x,0) = \begin{cases} 1 - 20x, & 0 \leqslant x \leqslant 0.05, \\ 0.5, & 0.25 \leqslant x \leqslant 0.4, \\ 0, & \text{otherwise}. \end{cases} \tag{3.42}$$

The computation is carried out up to $t = 0.5$ using 80 cells, and we show the results at $t = 0.1$, $t = 0.2$, $t = 0.4$ and $t = 0.5$ in Fig. 3.6. It is clear that the MCV-WENO4

scheme can reproduce the merging of two pulses well and recover good resolution for rarefaction wave.

3.5.4 1D Euler equations

Example 3.7. **Sod and Lax's problems.** These two tests are the 1D shock tube problem proposed in [49, 77]. For Sod's problem, the initial distribution is given by

$$(\rho_0, v_0, p_0) = \begin{cases} (1, 0, 1), & 0 \leqslant x \leqslant 0.5, \\ (0.125, 0, 0.1), & \text{otherwise.} \end{cases} \tag{3.43}$$

For Lax's problem [49], the initial profile is given by

$$(\rho_0, v_0, p_0) = \begin{cases} (0.445, 0.698, 3.528), & 0 \leqslant x \leqslant 0.5, \\ (0.5, 0, 0.571), & \text{otherwise.} \end{cases} \tag{3.44}$$

We use a 100-cell mesh for both of these tests, and at the boundary we use the Dirichlet boundary condition given with the constant value of initial distribution. In Sod's test, the computation is carried out up to $t = 0.25$, while in Lax's problem we conduct the computation to $t = 0.16$. The numerical results are shown in Figs.4.9 and 4.10. In both of the two tests, an expansion wave, a contact discontinuity and a shock is generated. We can see that our results can suppress the oscillations near the shock and resolve both contact discontinuity and expansion wave with good accuracy.

We also give the results computed with reflective boundary condition for Sod's problem. The reflective boundary condition used in this test problem is defined in Fig. 3.9. For the left boundary, the density and pressure at solution points of cell -1 and cell 0 are set to be the mirror reflection of those at solution points of cell 1 and cell 2 with $x = x_{0+\frac{1}{2}}$ to be the axis of the symmetry, i.e.

$$(\rho_{i,k}, p_{i,k}) = (\rho_{1-i,4-k}, p_{1-i,4-k}), \;\; i = -1, 0, \; k = 1, 2, 3, \tag{3.45}$$

and the velocity at solution points of cell -1 and cell 0 are defined by the equation

$$v_{i,k} = 2v^L_{wall} - v_{1-i,4-k}, \;\; i = -1, 0, \; k = 1, 2, 3. \tag{3.46}$$

where the v^L_{wall} is the moving speed of the left wall. In our computation, the velocity of the left wall is set to be zero. Thus, at the point $x_{0+\frac{1}{2}}$ we impose the condition $v^L_{wall} = v_{0+\frac{1}{2}} = v_{0,3} = v_{1,1} = 0$. To define reflective boundary at right side, we do the same manipulation as we have done for left boundary, i.e.

$$\begin{aligned} &(\rho_{i,k}, p_{i,k}) = (\rho_{2N+1-i,4-k}, p_{2N+1-i,4-k}), \\ &v_{i,k} = 2v^R_{wall} - v_{2N+1-i,4-k}, \quad i = N+1, N+2, \; k = 1, 2, 3. \end{aligned} \tag{3.47}$$

Also, in our calculation the right moving wall is defined with zero velocity, i.e.

$$v^R_{wall} = v_{N+\frac{1}{2}} = v_{N,3} = v_{N+1,1} = 0. \tag{3.48}$$

The numerical results after the shock wave is reflected by the boundary condition is shown in Fig.3.10. Here we use a mesh of 200 cells. We give the numerical results at 5 steps, 10 steps, 100 steps and 200 steps after the shock wave is reflected by the boundary condition respectively. From the numerical results, we can see that the reflective boundary condition doesn't have significant impact on the effectiveness of our WENO limiter, which means the numerical oscillations can still be suppressed near the discontinuities after the shock wave and constact discontinuity is reflected by the boundary condition.

Example 3.8. **Symmetry expansion wave[84].** For this test problem, the initial condition is given by

$$(\rho_0, v_0, p_0) = \begin{cases} (1.0, -2.0, 0.4), & 0 \leqslant x \leqslant 0.5, \\ (1.0, 2.0, 0.4), & \text{otherwise}, \end{cases} \tag{3.49}$$

This test describes an isentropic process. Both density and pressure are uniform in the whole domain, while a divergent velocity field split the flow field with an initial velocity having opposite directions at the center of computational domain. Our computation is

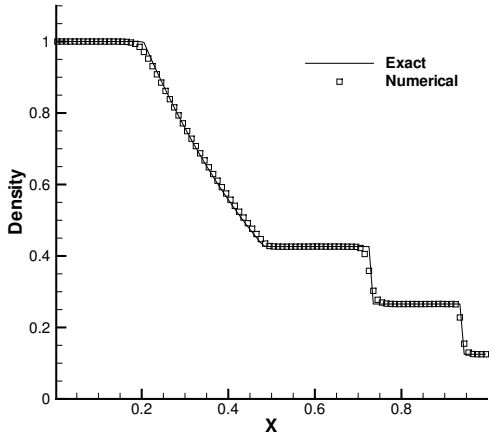

FIGURE 3.7: Numerical results of Sod's problem at $t = 0.25$ with 100 cells.

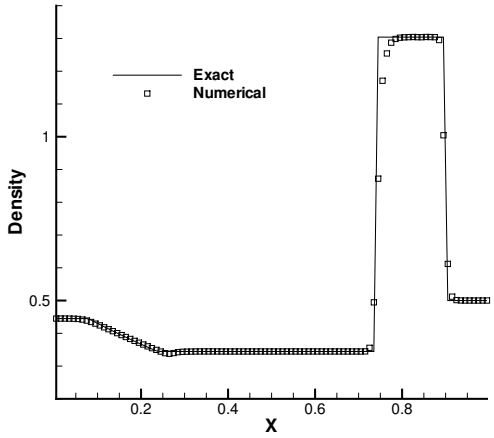

FIGURE 3.8: Numerical results of Lax's problem at $t = 0.16$ with 100 cells.

carried out up to $t = 0.15$ with 200 cells over $[0, 1]$. We show the numerical solutions of density, velocity, pressure and internal energy in Fig. 4.11. We find that the MCV-WENO4 scheme can accurately reproduce all the physical fields.

Example 3.9. **Shock-turbulence interaction.** This test problem is proposed in [73] to simulate a Mach 3 shock interacting with a density wave. The initial profile is given by

$$(\rho_0, v_0, p_0) = \begin{cases} (3.857143, 2.629369, 10.333333), & \text{when x} < 0.1, \\ (1.0 + 0.2\sin(50x - 25), 0, 1.0), & \text{when x} \geqslant 0.1. \end{cases} \tag{3.50}$$

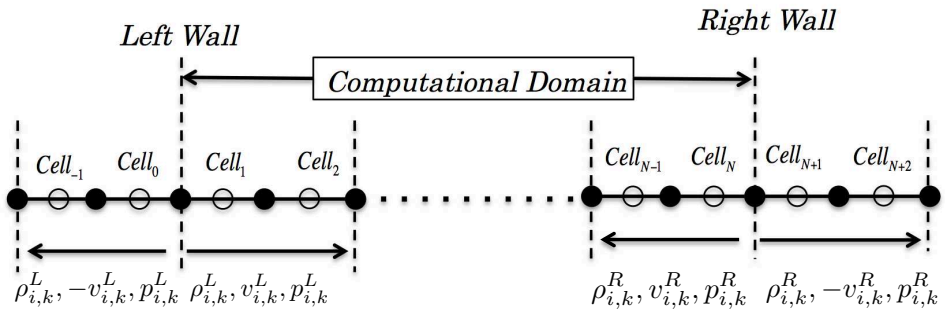

FIGURE 3.9: The reflective boundary condition for MCV-WENO4 scheme.

A Mach 3 shock is initially located at $x = 0.1$ and moves to the right. The initial density in the right part to the shock is generated by superimposing a sine-wave perturbation. The final results contain both the shock and smooth solutions. We perform the calculation until $t = 0.18$ with 200 cells over $[0, 1]$. The numerical solutions are shown in Fig. 4.12. The reference solution plotted by the solid line is computed by a fifth order WENO scheme of Jiang and Shu[45] with 2000 grid points. Our results show that there are no visible oscillations near the shock. Meanwhile, the density perturbation has been resolved accurately.

Example 3.10. **Two interacting blast waves.** This test problem was introduced by Wooward and Colella in[94]. Multiple interaction of strong shocks and rarefactions are included in this test problem. The initial condition with only the pressure difference is given by

$$(\rho_0, v_0, p_0) = \begin{cases} (1, 0, 1000), & \text{if } 0 \leqslant \mathrm{x} \leqslant 0.1, \\ (1, 0, 0.01), & \text{if } 0.1 < \mathrm{x} < 0.9, \\ (1, 0, 100), & \text{otherwise.} \end{cases} \tag{3.51}$$

The computation is conducted with 400 cells and reflective boundary condition. We give the numerical solutions of density ρ at $t = 0.038$ in Fig. 4.14, where the reference solution is computed by the finite volume scheme with MUSCL reconstruction on a grid of 4000 cells. We can see that our numerical solution fits well with the exact solution.

Given the fact that only two local DOFs per cell is used in the present scheme, we may conclude that the numerical results of examples 3.9 and 3.10 are among the best ever seen in the existing literature.

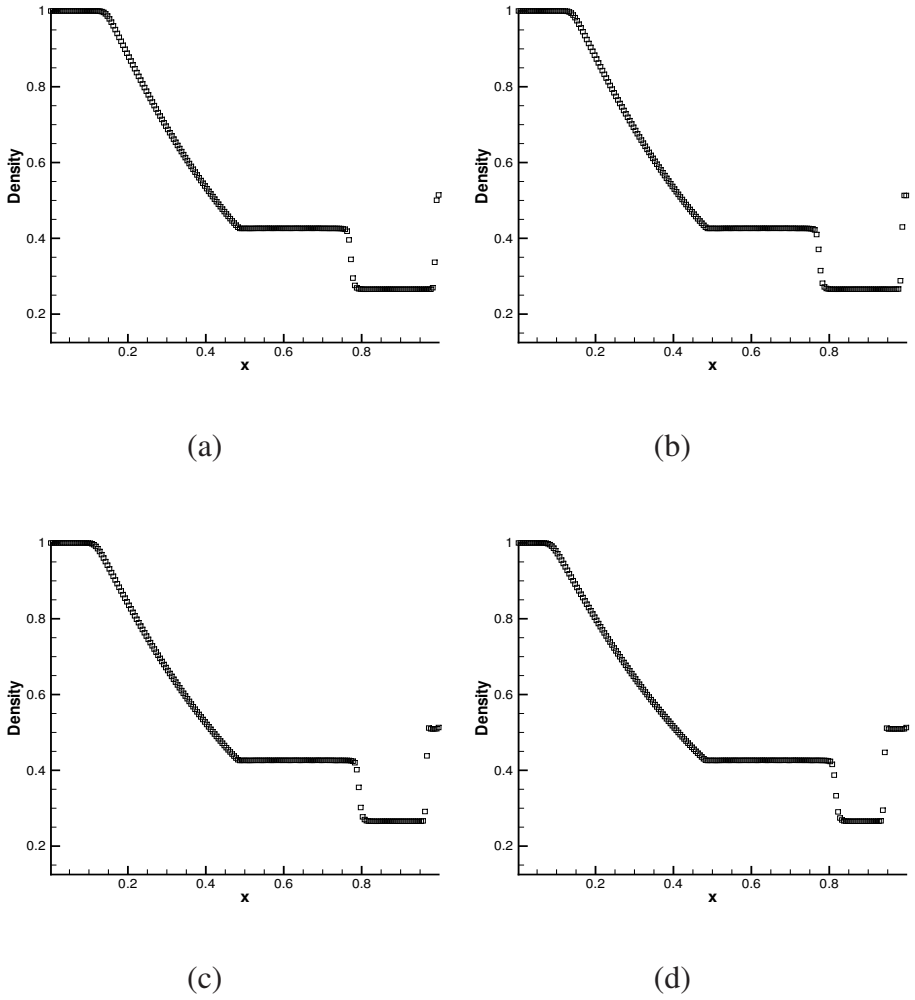

FIGURE 3.10: Numerical results of Sod's problem with reflective boundary condition at (a) 5 steps, (b) 10 steps, (c) 100 steps, (d) 200 steps after he shock wave is reflected by the boundary condition.

3.5.5 2D linear advection equation

In this subsection, we consider the 2D linear advection equation,

$$u_t + v_1 u_x + v_2 u_y = 0, \tag{3.52}$$

where (v_1, v_2) are the velocity components in x and y directions. For 2D linear advection equation, all our computation is performed on uniform Cartesian grid.

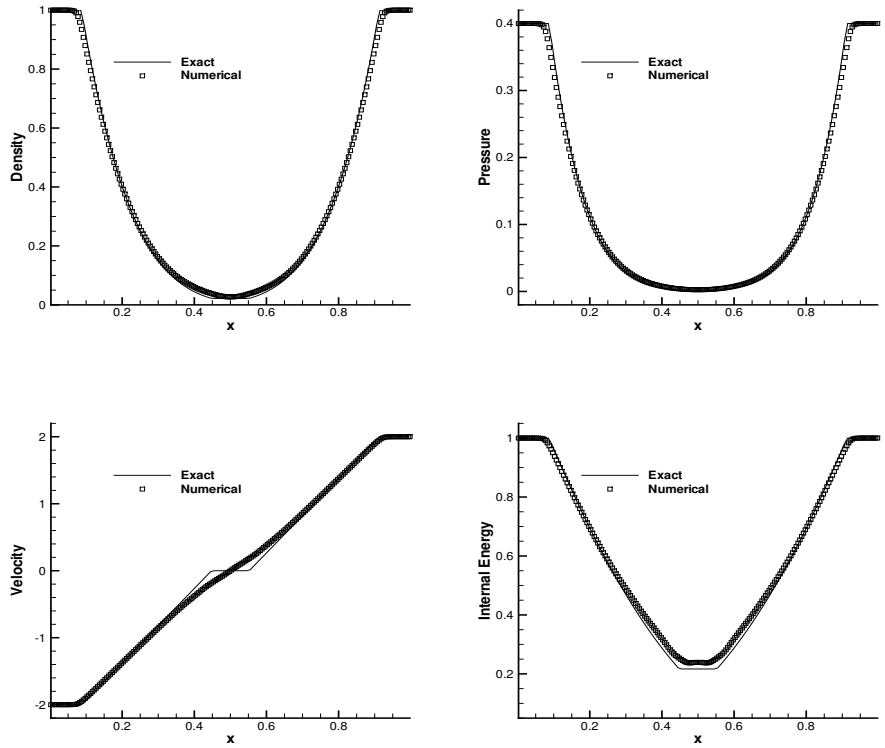

FIGURE 3.11: Numerical results of symmetrical expansion problem at $t = 0.15$ with 200 cells.

Example 3.11. **Accuracy test.** The accuracy test for 2D linear advection equation is conducted by using the mesh refinement. The initial smooth profile is given by

$$u(x, y, 0) = \sin(\pi(x + y)), \ x \in [-1, 1], \ y \in [-1, 1]. \tag{3.53}$$

Here the velocity is set to be the constant value $(v_1, v_2) = (1, 1)$. The computation is carried out up to $t = 2.0$ (after one period), and the periodic boundary condition is specified for this problem. From Table 3.4, we can see that the expected order of accuracy

TABLE 3.4: Numerical errors and convergence rate for 2D advection equation, $t = 2.0$.

$N_x \times N_y$	L_1 error	Order of Accuracy	L_∞ error	Order of Accuracy
10×10	1.55e-03		2.90e-03	
20×20	9.79e-05	3.98	1.54e-04	4.24
40×40	6.21e-06	3.98	9.77e-06	3.98
80×80	3.91e-07	3.99	6.15e-07	3.99

can be achieved by MCV-WENO4 scheme.

Example 3.12. **Transport of complex profile.** In this test, the 2D complex initial profile is given by

$$u(x,y,0)=\begin{cases}\dfrac{1}{6}\left(G(r_1+\delta,\beta)+G(r_1-\delta,\beta)+4G(r_1,\beta)\right), & |r_1|\leqslant 0.2,\\ 1, & |x|\leqslant 0.2,\ \ -0.7\leqslant y\leqslant -0.3,\\ 1-|5r_2|, & |r_2|\leqslant 0.2,\\ \dfrac{1}{6}\left(F(r_3+\delta,\alpha)+F(r_3-\delta,\alpha)+4F(r_3,\alpha)\right), & |r_3|\leqslant 0.2,\\ 0, & \text{otherwise},\end{cases} \tag{3.54}$$

where

$$r_1=\sqrt{(x+0.6)^2+y^2},\ r_2=\sqrt{(x-0.6)^2+y^2},\ r_3=\sqrt{x^2+(y-0.6)^2},$$

and $G(r,\beta)=\exp(-\beta r^2)$, $F(r,\alpha)=\sqrt{\max(1-\alpha^2r^2,0)}$. The coefficients are set to be $\delta=0.01$, $\alpha=5$ and $\beta=\log 2/(36\delta^2)$. The rotational velocity field is defined by $(v_1,v_2)=(-2\pi y,2\pi x)$ and the computation domain is $[-1,1]\times[-1,1]$. Our computation is executed up to $t=1.0$ on two grids of 50×50 and 100×100 respectively. The numerical results are shown in Fig. 4.6. We can see that there are no visible oscillations near the jump discontinuities, and the numerical solution resolves all the structures adequately even on a grid of low resolution.

3.5.6 2D Euler equations

In this subsection, we solve the 2D Euler equations

$$\frac{\partial \mathbf{u}}{\partial t}+\frac{\partial \mathbf{f}(\mathbf{u})}{\partial x}+\frac{\partial \mathbf{g}(\mathbf{u})}{\partial y}=0, \tag{3.55}$$

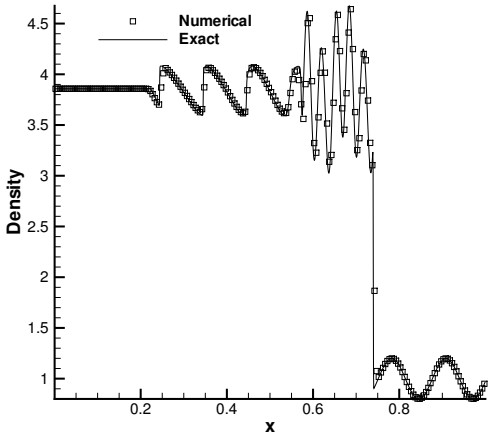

FIGURE 3.12: Numerical results of shock-turbulence interaction at $t = 0.18$ with 200 cells.

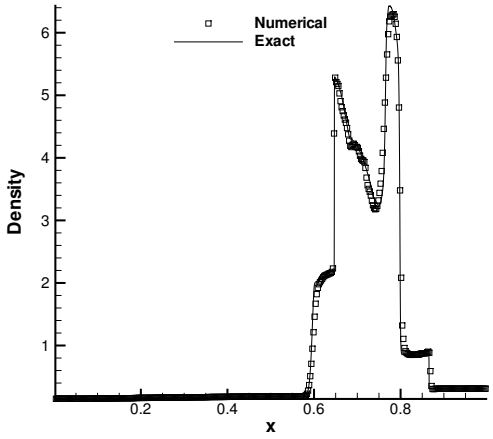

FIGURE 3.13: Numerical results of two interacting blast waves at $t = 0.038$ with 400 cells.

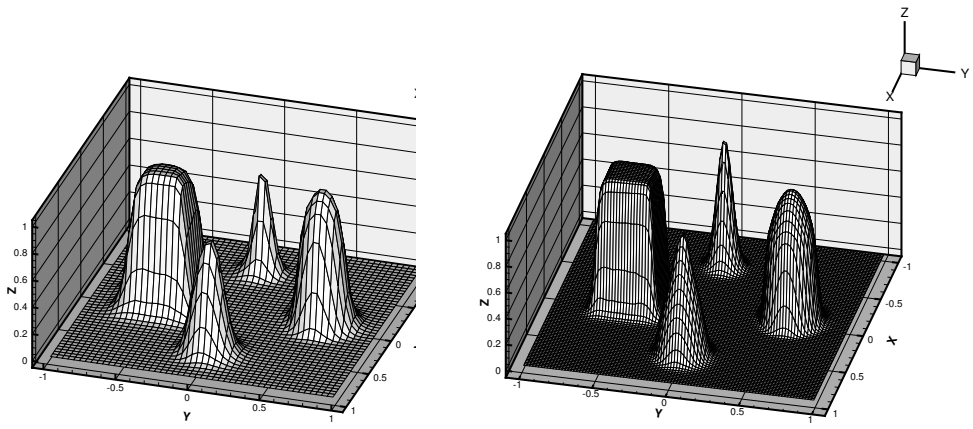

FIGURE 3.14: Numerical results of 2D rotation test at $t = 1.0$ on 50×50 (left) and 100×100 (right) grids.

where

$$\mathbf{u} = \begin{pmatrix} \rho \\ \rho u \\ \rho v \\ E \end{pmatrix}, \quad \mathbf{f}(\mathbf{u}) = \begin{pmatrix} \rho u \\ \rho u^2 + p \\ \rho uv \\ u(E+p) \end{pmatrix}, \quad \mathbf{g}(\mathbf{u}) = \begin{pmatrix} \rho v \\ \rho uv \\ \rho v^2 + p \\ v(E+p) \end{pmatrix}, \tag{3.56}$$

and (v_1, v_2) are the velocity components in x and y directions.

Example 3.13. **Accuracy test for 2D Euler equations.** To test the convergence rate of the MCV-WENO4 scheme, we use the following initial condition [61]

$$\begin{cases} \rho(x,y,0) = 1 + 0.2\sin\left(\pi(x+y)\right), \\ u(x,y,0) = 0.7, \\ v(x,y,0) = 0.3, \\ p(x,y,0) = 1.0. \end{cases} \qquad x \in [-1,1], y \in [-1,1] \tag{3.57}$$

With the velocity and pressure fields specified uniformly over the whole computation domain, only the perturbation of density is transported. The convergence rate is evaluated via the grid refinement. The L_1 and L_∞ errors of density are shown in Table 3.5. Here the N_x and N_y are the mesh number in x direction and y direction. We can clearly see that the MCV-WENO4 scheme can achieve the convergence rate of 4th order for 2D Euler equations as expected.

TABLE 3.5: Numerical errors and convergence rate for density perturbation test of 2D Euler equations at $t = 2.0$.

$N_x \times N_y$	L_1 error	Order of Accuracy	L_∞ error	Order of Accuracy
10×10	1.61e-04		3.00e-04	
20×20	1.04e-05	3.95	1.64e-05	4.20
40×40	6.66e-07	3.97	1.05e-06	3.97
80×80	4.20e-08	3.99	6.60e-08	3.99

Example 3.14. **Isentropic vortex.** This test is a 2D vortex evolution problem[34, 109], which is used to examine the order of accuracy of a scheme for the 2D Euler equations (3.55) when solving flows of strong nonlinearity. In this test, an isentropic vortex is propagated by a mean flow defined by $(\rho_\infty, u_\infty, v_\infty, p_\infty) = (1,1,1,1)$. The perturbation is given as

$$(\delta u, \delta v)^T = \frac{\epsilon}{2\pi}\exp\left(\frac{1-r^2}{2}\right)(-y,x)^T,\ \delta T = -\frac{(\gamma-1)\epsilon^2}{8\gamma\pi^2}\exp(1-r^2), \tag{3.58}$$

where $r^2 = x^2 + y^2$, $T = \dfrac{p}{\rho}$ is the temperature and $\epsilon = 5.0$ the vortex strength. The solution of this test is the advection transport of the initial vortex along the diagonal

direction. The computational domain is $[-5,5]\times[-5,5]$ with periodic boundary conditions. The L_1 and L_∞ errors of density at $t=10.0$ is shown in Table 3.6. We can see that convergence rate got from this test problem is not as uniform as the previous test. This phenomenon has also been observed for traditional WENO in [34]. It can be explained by the fact that in a coarse grid the smoothness indicator of WENO construction may incorrectly identify the smooth solutions with steep gradient as discontinuities. We can see from Table 3.6 that the our scheme tends to eventually converge to 4th order accuracy when the grid is sufficiently fine.

Also, to visually illustrate the convergence rate of the numerical solution, we compute this test on a computation area $[-5,5]\times[-5,5]$ up to $t=10.0$ and $t=100.0$ with the periodic boundary condition. We use a mesh of 32×32. The density distribution of numerical solutions on $y=0$ cross section is plotted in Fig. 3.15. We can see that the numerical solutions maintain visually identical to the analytical solutions at $t=10.0$, while at $t=100.0$ there is a slight accumulation of numerical dissipation which is acceptable for such a long term computation on a low resolution grid.

TABLE 3.6: Numerical errors and convergence rate for isentropic vortex of 2D Euler equations at $t=10.0$

$N_x\times N_y$	L_1 error	Order of Accuracy	L_∞ error	Order of Accuracy
20×20	7.55e-03		9.93e-02	
40×40	5.57e-04	3.76	5.57e-03	4.15
80×80	1.67e-04	1.75	2.80e-03	9.95
160×160	2.02e-06	6.36	6.09e-04	2.20
320×320	4.48e-10	5.50	3.99e-06	7.25

Example 3.15. **2D explosive test.** This test, as shown in [84], is an axi-symmetric two-dimensional explosion problem. Initially, the region inside a circle of radius $R=0.4$ is set with high pressure and density while the region out of the circle is of low pressure and density as,

$$(\rho,u,v,p)=\begin{cases}(1.0,0.0,0.0,1.0), & \text{if } \mathrm{r}\leqslant \mathrm{R},\\ (0.125,0.0,0.0,0.1), & \text{if } \mathrm{r}>\mathrm{R},\end{cases} \tag{3.59}$$

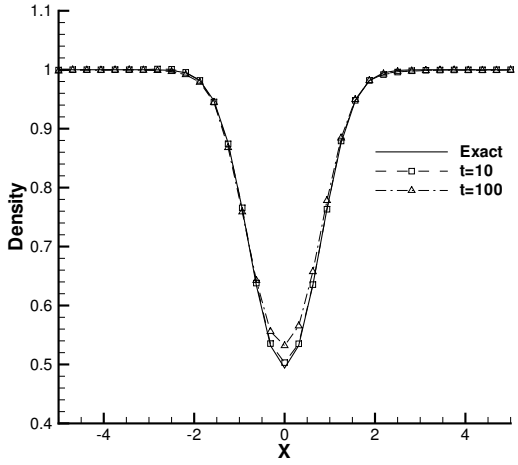

FIGURE 3.15: The density distribution of numerical solutions on $y = 0$ cross section at $t = 10.0$ and $t = 100.0$ with 32×32 cells.

where $r = \sqrt{x^2 + y^2}$ is the radius. So the fluid inside the circle will spread out to form a shock, a contact discontinuity and a rarefaction wave of cylindrical symmetry.

Our computation is run up to $t = 0.25$ on a 200×200 grid. We show the bird's eye view of density and pressure in Fig. 3.16. It is observed that the MCV-WENO4 scheme can well reproduce all the shock wave, contact discontinuity and rarefaction fan with perfect symmetry.

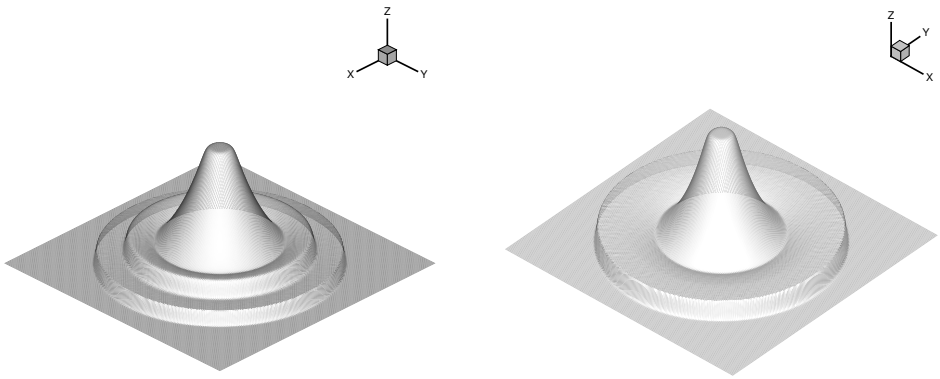

FIGURE 3.16: Numerical results of 2D explosive test at $t = 0.25$ with 200×200 cells. Displayed are density (left) and pressure (right).

Example 3.16. **Double Mach reflection.** This is a widely used test problem [94] to evaluate the ability of a scheme to capture both shock and vortex structures.

As detailed in [94], the computation domain is set to be $[0, 3.2] \times [0, 1]$. A right-moving Mach 10 shock positioned at $(\frac{1}{6}, 0)$ initially makes a 60° angle to the bottom boundary where a reflective boundary is imposed from $x = \frac{1}{6}$ to $x = 3.2$. In the region of $x \in [0, \frac{1}{6}]$ on the bottom boundary, as well as the left boundary, we impose the exact post shock condition. At the right boundary we set all the gradients to be zero. At the top boundary, the values of the flow are set to describe the exact motion of right moving Mach 10 shock. We carried out the computation up to $t = 0.2$. In Fig. 3.17, we give the numerical solutions calculated respectively by 120×384 cells and 250×800 cells. We see that with the refinement of the mesh resolution, the vortex structure between two strong shocks can be resolved adequately, which indicates the good transient performance of the MCV-WENO4 scheme. Also, we show the "blown-up" portion around the double Mach region in Fig. 3.18. It is found that our scheme can clearly recover the structure of the vortex with a reasonable high resolution.

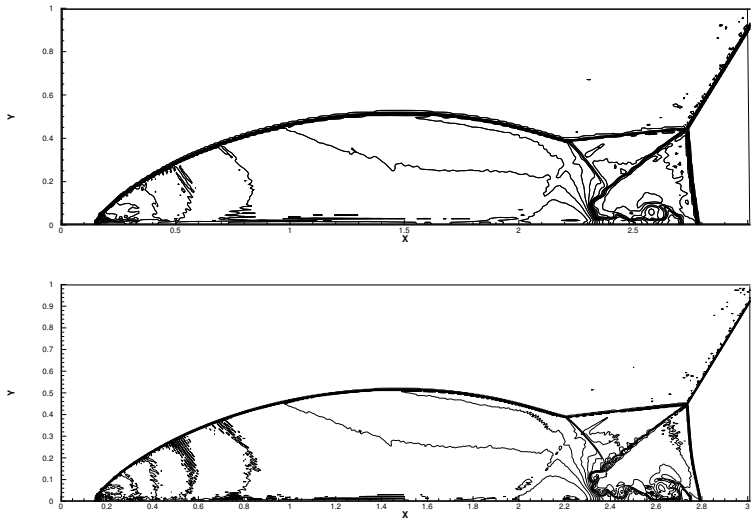

FIGURE 3.17: Numerical results of double Mach reflection at $t = 0.2$ with 120×384 cells (top), 250×800 cells (bottom).

Example 3.17. **Shock-vortex interaction in two dimensions.** This test which was originally presented in [45] describes the interaction between a Mach 1.1 stationary shock and an isentropic vortex. The computational domain is set to be $[0, 2] \times [0, 1]$.

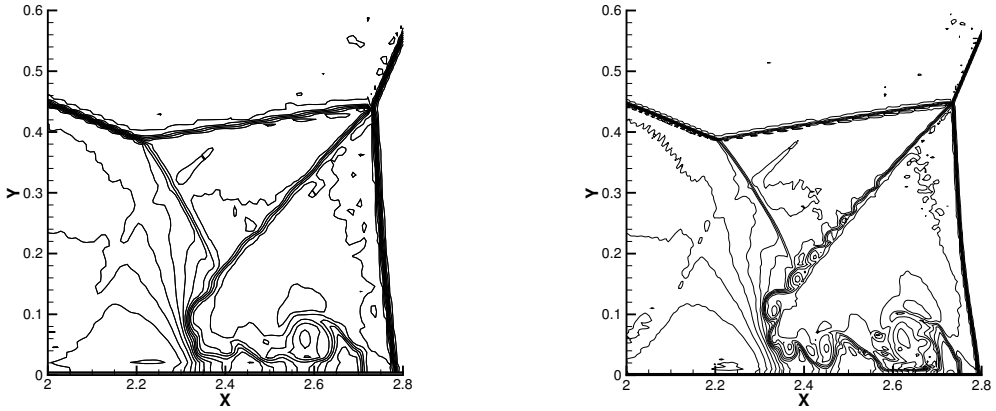

FIGURE 3.18: Numerical results of double Mach reflection at $t = 0.2$ with 120×384 cells(left), 250×800 cells(right).

Initially, a stationary shock is defined along the line $x = 0.5$, with next jump conditions

$$(\rho, u, v, p) = \begin{cases} (1.0, 1.1\sqrt{\gamma}, 0.0, 1.0), & \text{if } \mathrm{x} \leqslant 0.5, \\ (1.169082121, 0.940909094\sqrt{\gamma}, 0.0, 1.244999994), & \text{if } \mathrm{x} > 0.5. \end{cases} \tag{3.60}$$

Given the left side state, the right state of stationary shock is calculated from Rankine-Hugoniot condition.

The vortex is located at the center of the super-sonic area $(x_c, y_c) = (0.25, 0.5)$. The initial structure of the vortex is generated from the following perturbation,

$$(\delta u, \delta v)^T = \epsilon\tau e^{\alpha(1-\tau^2)}(\sin(\theta), -\cos(\theta))^T,\ \delta T = -\frac{(\gamma-1)\epsilon^2}{4\alpha\gamma} e^{2\alpha(1-\tau^2)}, \delta S = 0, \tag{3.61}$$

where $\tau = r/r_c$, $r = \sqrt{(x-x_c)^2 + (y-y_c)^2}$ and $r_c = 0.05$ is the critical radius of the vortex. $\epsilon = 0.3$ is the strength of the vortex, and $\alpha = 0.204$ is related to the decay rate of the vortex. θ represents the angle between the angular velocity and the horizontal axis. The top and bottom boundaries are set to be reflective walls.

We compute this test problem on a grid of 50×100 in order to compare with the results in [45]. We show the pressure contour at $t = 0.05$, 0.2, 0.35 and 0.6 in Fig.3.19. For $t = 0.05$, 0.2 and 0.35, the reflective wall does not significantly affect the flow field, while at $t = 0.6$, the bifurcation of shock is reflected by the top and bottom walls. It

can be observed that our results can well resolve the interaction between the vortex and shock with competitive quality in comparison with the previous works.

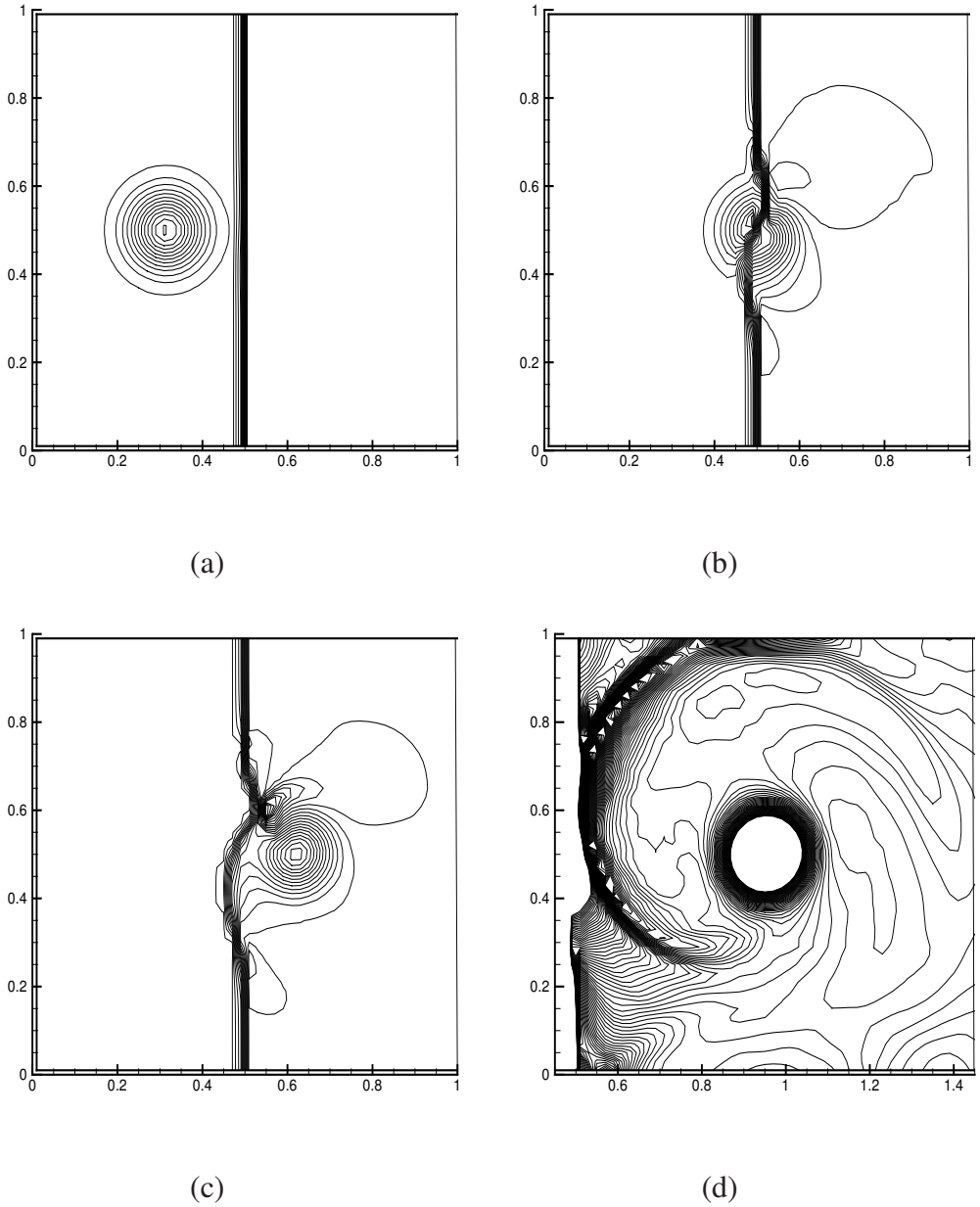

FIGURE 3.19: Numerical results of shock-vortex interaction problem at (a) $t = 0.05$, (b) $t = 0.2$, (c) $t = 0.35$ and (d) $t = 0.6$ on a 50×100 mesh. The number of contours is 30 for (a)-(c) and 90 for (d) respectively.

3.6 Summary

In this chapter, we have presented and tested a new WENO-type limiter for MCV3 scheme under the MMC-FR framework. The basic idea is to reconstruct the first order derivative at the cell center of the MCV-SC scheme using the WENO methodology.

Compared with other existing methods, the MCV-WENO4 scheme presented here has at least following advantages. 1) The WENO reconstruction is based on the sub-grid solution structures from the nodal values at the solution points within the target cell and its immediate neighbors. The stencil for reconstruction is minimized. Thus, the scheme is better suited for the local high-order reconstruction schemes where sub-grid information is available. 2) The present scheme has much less numerical dissipation to the smooth solution, and thus doesn't use the ad hoc TVB criterion (or so-called "trouble cell" indicator) that is needed in nearly all existing schemes. 3) The present scheme is algorithmically simple and computationally efficient.

The numerical results for the widely used benchmark tests show that our scheme can get the 4th-order uniform convergence rate as expected and high quality solutions for both discontinuities and smooth profiles.

Chapter 4

A Semi-Lagrangian Multi-Moment FVM with 4th-order WENO Projection

In this chapter, the PV-based WENO limiter proposed in previous chapter is applied to an conservative CIP semi-Lagrangian method, i.e. CIP-CSL3 scheme, with proper modification. The merit of the semi-Lagrangian approach lies in its larger allowable CFL number and less numerical dissipation. With theoretically infinite CFL restriction, we can acquire better computational efficiency compared with the Eulerian method. Because the semi-Lagrangian method updates the quantity by tracing back the characteristic line, the numerical solutions can be obtained with less numerical dissipation for hyperbolic partial differential equation.

The introduction of new scheme starts from the review of CIP multi-moment finite volume method (CIP/MM FVM) scheme in the following paragraph.

4.1 Review of CIP/MM FVM scheme

In this section, we will introduce the numerical formulation of CIP/MM FVM for both scalar conservation law and Euler equations. For Euler equations, we adapt the method

proposed in [40], which computes the PV using the semi-Lagrangian solution in terms of Riemann invariants along the characteristic curves, while the VIA is updated in a conservative formulation where the numerical flux is evaluated from the quadrature of PVs at Runge-Kutta sub-steps.

4.1.1 Scalar conservation law

We firstly consider the following 1D conservative transport equation

$$\frac{\partial u}{\partial t} + \frac{\partial au}{\partial x} = 0, \tag{4.1}$$

where $u(x,t)$ is the solution function, and $a(x)$ the velocity. The computational domain is divided into I non-overlapping cells or elements $\Omega_i = [x_{i-\frac{1}{2}}, x_{i+\frac{1}{2}}]$, $i = 1, 2, \cdots, I$. Inside each element, we define the following two types of moments respectively

- the volume integrated average (VIA) over each cell element

$$\overline{u}_i = \frac{1}{\Delta x_i} \int_{x_{i-\frac{1}{2}}}^{x_{i+\frac{1}{2}}} u(x,t)dx, \tag{4.2}$$

  where $\Delta x_i = x_{i+\frac{1}{2}} - x_{i-\frac{1}{2}}$, and

- the point value (PV) at the cell boundary

$$u_{i+\frac{1}{2}} = u(x_{i+\frac{1}{2}}, t). \tag{4.3}$$

Here both VIA and PV are simultaneously treated as the model variables, and we can build up the interpolation function inside each element by using both VIA and PV. Several Conservative semi-Lagrangian CIP (CIP-CSL) schemes [83, 96, 99, 107] have been proposed in the literatures. We introduce the interpolation procedure of the CIP-CSL with 3rd order polynomial function (CIP-CSL3) [96] as an example of deriving the CIP-CSL schemes.

4.1.1.1 CIP-CSL3 reconstruction

In each cell element $[x_{i-\frac{1}{2}}, x_{i+\frac{1}{2}}]$, we can construct a cubic interpolation function in a form

$$\tilde{u}(x) = a_3(x - x_i)^3 + a_2(x - x_i)^2 + a_1(x - x_i) + a_0, \tag{4.4}$$

where x_i is the cell central point, and the unknown coefficients are computed by imposing the following constraint conditions

$$\begin{cases} \tilde{u}(x_{i+\frac{1}{2}}) = u_{i+\frac{1}{2}}, \\ \tilde{u}(x_{i-\frac{1}{2}}) = u_{i-\frac{1}{2}}, \\ \dfrac{1}{\Delta x_i}\displaystyle\int_{x_{i-\frac{1}{2}}}^{x_{i+\frac{1}{2}}} \tilde{u}(x)dx = \overline{u}_i, \\ \left(\dfrac{d\tilde{u}(x)}{dx}\right)_i = u_x^{[1]}(x_i), \end{cases} \tag{4.5}$$

where $u_x^{[1]}(x_i)$ is the first order derivative of the interpolation function at the cell center. The coefficients of the interpolation function can be given explicitly by

$$\begin{cases} a_3 = \dfrac{4}{\Delta x_i^3}(u_{i+\frac{1}{2}} - u_{i-\frac{1}{2}} - u_x^{[1]}(x_i)\Delta x_i), \\ a_2 = \dfrac{3}{\Delta x_i^2}(u_{i-\frac{1}{2}} + u_{i+\frac{1}{2}} - 2\overline{u}_i), \\ a_1 = u_x^{[1]}(x_i), \\ a_0 = -\dfrac{1}{4}(u_{i+\frac{1}{2}} + u_{i-\frac{1}{2}}) + \dfrac{3}{2}\overline{u}_i. \end{cases} \tag{4.6}$$

Here the first-order derivative $u_x^{[1]}(x_i)$ can be obtained from an interpolation that involves the VIA and PV from neighboring cells . For example, a fourth-order approximation can be obtained by using the VIAs $\overline{u}_{i+1}, \overline{u}_{i-1}$ and PVs $u_{i+\frac{1}{2}}, u_{i-\frac{1}{2}}$ from two neighboring cells

$$u_x^{[1]}(x_i) = \frac{10u_{i+\frac{1}{2}} - 10u_{i-\frac{1}{2}} + \overline{u}_{i-1} - \overline{u}_{i+1}}{8\Delta x_i}. \tag{4.7}$$

With different choices to approximate the first order derivative $u_x^{[1]}(x_i)$, we can modify

the interpolation function to reach some desired properties for the resulting numerical scheme. It will be shown later that the $u_x^{[1]}(x_i)$ can be reconstructed by WENO methodology to yield the essentially non-oscillatory (ENO) property.

4.1.1.2 Time integration

We have constructed the interpolation function inside each element in the previous subsection. The next problem is how to use the interpolation function to update the solutions $\overline{u}_i^n$ and $u_{i+\frac{1}{2}}^n$ from time t^n to next time step $t^{n+1} = t^n + \Delta t$ with Δt being the time-step increment. We will introduce the time integration procedure of CIP-CSL scheme for moment VIA and PV respectively in the followings.

Update the PV

For CIP-CSL scheme, we compute the semi-Lagrangian solution $u_{i+\frac{1}{2}}$ by firstly finding out the departure point for each cell boundary. The departure point can be obtained by solving the initial value problem

$$\begin{cases} \dfrac{\mathrm{d}X}{\mathrm{d}t} = -a(X,t), \\ X(t_0 = t^n) = X_0 = x_{i+\frac{1}{2}}. \end{cases} \tag{4.8}$$

The ordinary differential equation (ODE) (4.8) can be solved by a third-order Runge-Kutta scheme as

$$\begin{cases} X_1 = X_0 - a(X_0, t_0)\Delta t, \\ X_2 = \dfrac{3}{4}X_0 + \dfrac{1}{4}X_1 - \dfrac{1}{4}a(X_1, t_1)\Delta t, \\ X_3 = \dfrac{1}{3}X_0 + \dfrac{2}{3}X_2 - \dfrac{2}{3}a(X_2, t_2)\Delta t, \end{cases} \tag{4.9}$$

or equivalently

$$\begin{cases} X_1 = X_0 - a(X_0, t_0)\Delta t, \\ X_2 = X_0 - \dfrac{1}{4}(a(X_0, t_0) + a(X_1, t_1))\Delta t, \\ X_3 = X_0 - \dfrac{1}{6}(a(X_0, t_0) + a(X_1, t_1) + 4a(X_2, t_2))\Delta t. \end{cases} \tag{4.10}$$

The governing equation (4.1) can be re-written in a non-conservative as

$$\frac{\partial u}{\partial t} + a\frac{\partial u}{\partial x} + u\frac{\partial a}{\partial x} = 0, \tag{4.11}$$

where the second term $a\frac{\partial u}{\partial x}$ represents the advection part and the third term $u\frac{\partial a}{\partial x}$ represents the divergence correction part. For advection part, we can compute the semi-Lagrangian solution of PV at each substep of Runge-Kutta integration

$$u_{i+\frac{1}{2}}^{\langle l \rangle} = \tilde{u}_i(X_l), \quad l = 1, 2, 3, \tag{4.12}$$

where l represents the lth substep of the third order Runge-Kutta method. $\tilde{u}_i(x)$ is the piece-wise interpolation function in the form of (4.4) constructed at $t = t^n$ over the mesh where the departure point X_l falls in.

For non-advection part, we can obtain the solution u by integrating the equation $\frac{du}{dt} = -u\frac{\partial a}{\partial x}$ along the trajectory. The right-hand side can be approximated by the summation $\hat{D}_{i+\frac{1}{2}} = -\Delta t \sum_{l'=0}^{l-1} \alpha_{l'} \tilde{u}_i(X_{l'}) \frac{\partial a}{\partial x}(X_{l'})$ where $\alpha_{l'}$ represents the Runge-Kutta weight coefficients.

Finally, the PV at cell boundary of time $t = t^{n+1}$ can be given as the sum of the contributions from advection part and non-advection part

$$u_{i+\frac{1}{2}}^{n+1} = u_{i+\frac{1}{2}}^{\langle 3 \rangle} + D_{i+\frac{1}{2}}. \tag{4.13}$$

Update the VIA

To update the VIA to the next time step, we adopt an FVM approach by integrating (4.1) over the interval $[x_{i-\frac{1}{2}}, x_{i+\frac{1}{2}}]$, which yields the following conservative formulation

$$\overline{u}^{n+1} = \overline{u}^n - \frac{\Delta t}{\Delta x_i}(F_{i+\frac{1}{2}}(a,u) - F_{i-\frac{1}{2}}(a,u)), \tag{4.14}$$

where $F(a,u) = au$ for the transport equation (4.1) is the numerical flux which can

be computed either by the exact integration of the interpolation function along the trajectory or through a quadrature from the values sampled at the sub-steps of the Runge-Kutta method. In this work, we use the latter for its simplicity and adequate accuracy. The approximated numerical flux is then given by

$$F_{i+\frac{1}{2}}(a,u) \approx \hat{F}_{i+\frac{1}{2}}(a,u) = \frac{F(a(X_0,t^n),u^{\langle 0\rangle}_{i+\frac{1}{2}}) + F(a(X_1,t^n),u^{\langle 1\rangle}_{i+\frac{1}{2}}) + 4F(a(X_2,t^n),u^{\langle 2\rangle}_{i+\frac{1}{2}})}{6}, \tag{4.15}$$

and the VIA is updated by

$$\overline{u}^{n+1} = \overline{u}^n - \frac{\Delta t}{\Delta x_i}(\hat{F}_{i+\frac{1}{2}}(a,u) - \hat{F}_{i-\frac{1}{2}}(a,u)). \tag{4.16}$$

4.1.2 Euler conservation laws

The implementation of CIP/MM FVM scheme for Euler conservation laws is based on the hyperbolicity of Euler equations by computing the semi-Lagrangian solution in terms of the characteristic variables. The VIA can be updated through a flux-form formulation, while the numerical flux is approximated from the semi-Lagrangian solution of PV at each Runge-Kutta substep. Here, we also use the TVD third-order Runge-Kutta time integration method to update the semi-Lagrangian solutions.

4.1.2.1 The characteristic equations for 1D Euler equations

The conservative form of 1D Euler equations for ideal gas is given by

$$\mathbf{U}_t + \mathbf{F}(\mathbf{U})_x = 0, \tag{4.17}$$

where

$$\mathbf{U} = \begin{pmatrix} u^{(1)} \\ u^{(2)} \\ u^{(3)} \end{pmatrix} = \begin{pmatrix} \rho \\ \rho v \\ E \end{pmatrix}, \quad \mathbf{F}(\mathbf{U}) = \begin{pmatrix} f^{(1)} \\ f^{(2)} \\ f^{(3)} \end{pmatrix} = \begin{pmatrix} \rho v \\ \rho v^2 + p \\ v(E+p) \end{pmatrix}. \tag{4.18}$$

Here ρ is the density, v the velocity, p the pressure and E the total energy. We use the equation of state (EOS) of ideal gas in our calculation, i.e.

$$E = \frac{p}{\gamma - 1} + \frac{1}{2}\rho v^2, \tag{4.19}$$

where $\gamma = 1.4$.

The 1D Euler equations can also be formulated in terms of primitive variables in a quasi-linear form

$$\mathbf{W}_t + \mathbf{A}\mathbf{W}_x = 0, \tag{4.20}$$

where

$$\mathbf{W} = \begin{pmatrix} \rho \\ v \\ p \end{pmatrix}, \quad \mathbf{A} = \begin{bmatrix} v & \rho & 0 \\ 0 & v & 1/\rho \\ 0 & \rho c^2 & v \end{bmatrix}, \tag{4.21}$$

and $c = \sqrt{\frac{\gamma p}{\rho}}$ is the sound speed. The Jacobian matrix $\mathbf{A}$ can be diagonalized by using the left and right eigenvectors

$$\mathbf{A} = \mathbf{R}\Lambda\mathbf{L}. \tag{4.22}$$

Here Λ is the diagonal matrix of eigenvalues which are the propagation speeds of the characteristic variables. $\mathbf{L}$ and $\mathbf{R}$ denote the matrices of left and right eigenvectors respectively, which satisfy $\mathbf{R} = \mathbf{L}^{-1}$.

Then, the equations (4.20) can be recast into the characteristic form

$$\mathbf{L}\mathbf{W}_t + \Lambda\mathbf{L}\mathbf{W}_x = 0, \quad \Lambda = \begin{bmatrix} v & 0 & 0 \\ 0 & v+c & 0 \\ 0 & 0 & v-c \end{bmatrix}, \quad \mathbf{L} = \begin{bmatrix} 1 & 0 & \frac{-1}{c^2} \\ 0 & 1 & \frac{1}{\rho c} \\ 0 & 1 & \frac{-1}{\rho c} \end{bmatrix}. \tag{4.23}$$

For each characteristic direction $\frac{\mathrm{d}X}{\mathrm{d}t} = \lambda_m$, we have the following characteristic equation

$$\mathbf{L}^m \mathrm{d}\mathbf{W} = 0,\ m = 1, 2, 3. \tag{4.24}$$

$\mathbf{L}^m$ is the mth row vector of matrix $\mathbf{L}$. By expanding (4.24) for each left eigenvector $\mathbf{L}^1$, $\mathbf{L}^2$ and $\mathbf{L}^3$, we can get the following characteristic equations

$$\mathrm{d}\rho - \frac{1}{c^2}\mathrm{d}p = 0 \quad \text{along} \quad \theta_1 : \frac{\mathrm{d}X}{\mathrm{d}t} = \lambda_1 = v,\ \ X(t=0) = X_0, \tag{4.25a}$$

$$\mathrm{d}v + \frac{1}{\rho c}\mathrm{d}p = 0 \quad \text{along} \quad \theta_2 : \frac{\mathrm{d}X}{\mathrm{d}t} = \lambda_2 = v + c,\ \ X(t=0) = X_0, \tag{4.25b}$$

$$\mathrm{d}v - \frac{1}{\rho c}\mathrm{d}p = 0 \quad \text{along} \quad \theta_3 : \frac{\mathrm{d}X}{\mathrm{d}t} = \lambda_3 = v - c,\ \ X(t=0) = X_0, \tag{4.25c}$$

where $\theta_m,\ m = 1, 2, 3$ represents each characteristic curve. Then the primitive variables at $t = t^{n+1}$ can be found through the following coupled equations

$$\rho(X_0)^{n+1} - \rho(X(\theta_1)) - \frac{1}{c^2}\{p(X_0)^{n+1} - p(X(\theta_1))\} = 0, \tag{4.26a}$$

$$v(X_0)^{n+1} - v(X(\theta_2)) + \frac{1}{\rho c}\{p(X_0)^{n+1} - p(X(\theta_2)\} = 0, \tag{4.26b}$$

$$v(X_0)^{n+1} - v(X(\theta_3)) - \frac{1}{\rho c}\{p(X_0)^{n+1} - p(X(\theta_3)\} = 0, \tag{4.26c}$$

where $X(\theta_m), m = 1, 2, 3$ indicates the solution point computed from the interpolation function on each characteristic curve.

4.1.2.2 The update of the multi-moments for 1D Euler equations

As mentioned in the previous sub-section, we have defined two types of moments inside each cell element, i.e.

$$\begin{aligned} &\text{PV}: \quad \mathbf{W}_{i+\frac{1}{2}} = \mathbf{W}(x_{i+\frac{1}{2}}, t), \\ &\text{VIA}: \quad \overline{\mathbf{W}}_i = \frac{1}{\Delta x_i}\int_{x_{i-\frac{1}{2}}}^{x_{i+\frac{1}{2}}} \mathbf{W}(x,t)dx. \end{aligned} \tag{4.27}$$

The departure point can be found by solving the following trajectory equations along the characteristic curves

$$\begin{cases} \dfrac{\mathrm{d}X}{\mathrm{d}t} = -\lambda_m(X,t), \\ X(t=0) = X_0 = x_{i+\frac{1}{2}}, \end{cases} \quad m = 1,2,3. \tag{4.28}$$

Here $\lambda_m(X,t)$ is the characteristic speed of each characteristic curve. Same as in the scalar case, we solve the above ODE by the third-order Runge-Kutta method

$$\begin{cases} X_1(\theta_m) = X_0 - \lambda_m(X_0,t_0)\Delta t, \\ X_2(\theta_m) = \dfrac{3}{4}X_0 + \dfrac{1}{4}X_1(\theta_m) - \dfrac{1}{4}\lambda_m(X_0,t_1)\Delta t, \ m = 1,2,3, \\ X_3(\theta_m) = \dfrac{1}{3}X_0 + \dfrac{2}{3}X_2(\theta_m) - \dfrac{2}{3}\lambda_m(X_0,t_2)\Delta t, \end{cases} \tag{4.29}$$

where θ_m denotes the mth characteristic curve. By solving the linear system (4.26), we have the semi-Lagrangian solution of the primitive variables at each Runge-Kutta substep as follows,

$$\begin{aligned} p_{i+\frac{1}{2}}^{\langle l\rangle} &= \frac{1}{2}\left(p(X_l(\theta_2)) + p(X_l(\theta_3)) + p_{i+\frac{1}{2}}^{\langle l-1\rangle} c_{i+\frac{1}{2}}^{\langle l-1\rangle}\left(v(X_l(\theta_2)) - v(X_l(\theta_3))\right)\right), \\ v_{i+\frac{1}{2}}^{\langle l\rangle} &= \frac{1}{2}\left(v(X_l(\theta_2)) + v(X_l(\theta_3)) + \frac{1}{\rho_{i+\frac{1}{2}}^{\langle l-1\rangle} c_{i+\frac{1}{2}}^{\langle l-1\rangle}}\left(v(X_l(\theta_2)) - v(X_l(\theta_3))\right)\right), \\ \rho_{i+\frac{1}{2}}^{\langle l\rangle} &= \rho(X_l(\theta_1)) + \frac{1}{(c_{i+\frac{1}{2}}^{\langle l-1\rangle})^2}\left(p_{i+\frac{1}{2}}^{\langle l\rangle} - p(X_l(\theta_3))\right), \end{aligned} \tag{4.30}$$

where $\rho(x), v(x)$ and $p(x)$ denote the interpolation functions for the primitive variables ρ, v and p respectively. $\rho(X_l(\theta_m)), v(X_l(\theta_m))$ and $p(X_l(\theta_m)),\ m = 1,2,3;\ l = 1,2,3,$ are the semi-Lagrangian solutions to the primitive variables along characteristic curve θ_m at the lth Runge-Kutta sub-step.

Consequently, we can update the PVs of the primitive variables at cell boundary $x = x_{i+\frac{1}{2}}$ to the next time step t^{n+1} directly by

$$\begin{aligned} p_{i+\frac{1}{2}}^{n+1} &= p_{i+\frac{1}{2}}^{\langle 3\rangle}, \\ v_{i+\frac{1}{2}}^{n+1} &= v_{i+\frac{1}{2}}^{\langle 3\rangle}, \\ \rho_{i+\frac{1}{2}}^{n+1} &= \rho_{i+\frac{1}{2}}^{\langle 3\rangle}. \end{aligned} \tag{4.31}$$

The update of the VIA for the conservative variables $\mathbf{U}$ simply follows the traditional FVM method as

$$\overline{\mathbf{U}}_i^{n+1} = \overline{\mathbf{U}}_i^n - \frac{\Delta t}{\Delta x_i}(\hat{\mathbf{F}}_{i+\frac{1}{2}} - \hat{\mathbf{F}}_{i-\frac{1}{2}}). \tag{4.32}$$

Here the numerical flux $\hat{\mathbf{F}}_{i+\frac{1}{2}}$ can be obtained by the numerical integration of the PVs from the Runge-Kutta substeps as

$$\hat{\mathbf{F}}_{i+\frac{1}{2}} = \frac{\mathbf{F}(\mathbf{W}_{i+\frac{1}{2}}^{\langle 0\rangle}) + \mathbf{F}(\mathbf{W}_{i+\frac{1}{2}}^{\langle 1\rangle}) + 4\mathbf{F}(\mathbf{W}_{i+\frac{1}{2}}^{\langle 2\rangle})}{6}. \tag{4.33}$$

4.2 WENO limiter

In this section, we will introduce the WENO limiter built from the local information available in the CIP-CSL3 scheme. The basic idea of our WENO limiter is to reconstruct the first order derivative at the cell center for the interpolation function of CIP-CSL3 scheme. As the local information of both PV and VIA is used in the WENO interpolation, our WENO limiter is more suitable for multi-moment reconstruction of CIP/MM FVM. Moreover, the limiting projection of the present WENO limiter can be applied to all cells without causing excessive numerical dissipation, unlike other existing WENO limiters which work only for the so-called "trouble-cells" identified by an ad hoc TVB criterion.

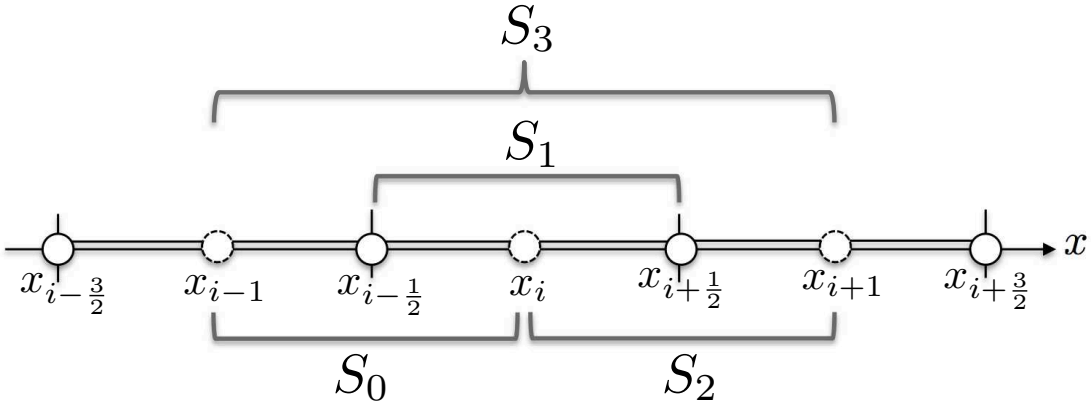

FIGURE 4.1: Reconstruction stencils for the WENO limiter.

4.2.1 WENO limiter for scalar conservation law

The present WENO reconstruction uses the information of both PV and VIA. For the sake of simplicity, instead of direct use of the VIA we use the PV at the center of cell Ω_i for interpolation, which is computed by

$$\hat{u}_i = \frac{3}{2}\overline{u}_i - \frac{1}{4}(u_{i-\frac{1}{2}} + u_{i+\frac{1}{2}}). \tag{4.34}$$

Given the PVs at the cell center $\hat{u}_i$ and the cell boundaries $u_{i\pm\frac{1}{2}}$, we can set the WENO interpolation stencils as shown in Fig. 4.1. Here we have three small stencils $S_j = \left\{x_{i-1+\frac{j}{2}}, x_{i-\frac{1}{2}+\frac{j}{2}}, x_{i+\frac{j}{2}}\right\},\ j = 0, 1, 2$, and one large stencil $S_3 = \left\{x_{i-1}, x_{i-\frac{1}{2}}, x_i, x_{i+\frac{1}{2}}, x_{i+1}\right\}$. Over each small stencil, we can construct a 2nd-degree polynomial with three PVs. The polynomial obtained from each stencil, S_j, is denoted by $q_j(x),\ j = 0, 1, 2$. Then, we can compute the first order derivatives at the cell center with second order accuracy respectively from the derivatives of polynomials $q_j(x),\ j = 0, 1, 2$ as

$$\begin{aligned} q_0^{[1]}(x_i) &= \frac{3\hat{u}_i + \hat{u}_{i-1} - 4u_{i-\frac{1}{2}}}{\Delta x_i}, \\ q_1^{[1]}(x_i) &= \frac{u_{i+\frac{1}{2}} - u_{i-\frac{1}{2}}}{\Delta x_i}, \\ q_2^{[1]}(x_i) &= -\frac{3\hat{u}_i + \hat{u}_{i+1} - 4u_{i+\frac{1}{2}}}{\Delta x_i}. \end{aligned} \tag{4.35}$$

Similarly, we can construct a fourth degree polynomial in the large stencil S_3, denoted by $Q_i(x)$, and approximate the first order derivative at the cell center with 4th order accuracy by

$$Q_i^{[1]}(x_i) = \frac{8u_{i+\frac{1}{2}} + \hat{u}_{i-1} - 8u_{i-\frac{1}{2}} - \hat{u}_{i+1}}{6\Delta x_i}, \tag{4.36}$$

which can be expressed as a linear combination of the 2nd order approximations from the three small stencils

$$Q_i^{[1]}(x_i) = \sum_{j=0}^{2} \gamma_j q_j^{[1]}(x_i), \tag{4.37}$$

where

$$\gamma_0 = \frac{1}{6}, \quad \gamma_1 = \frac{2}{3}, \quad \gamma_2 = \frac{1}{6}. \tag{4.38}$$

By replacing the linear weights γ_j by nonlinear weights ω_j using the WENO methodology, we can achieve the essentially non-oscillatory property for the numerical scheme.

For the WENO reconstruction, we define the smoothness indicator by

$$\beta_j = \sum_{l=1}^{2} \int_{x_{i-\frac{1}{8}}}^{x_{i+\frac{1}{8}}} \Delta x_i^{2l-1} \left(\frac{\partial^l q_j(x)}{\partial x^l} \right)^2 dx, \quad j = 0, 1, 2. \tag{4.39}$$

The smoothness indicator measures the smoothness of the reconstructed polynomials in the target cell Ω_i. In order to match the compact WENO reconstruction stencil of the present scheme, we adjust the upper and lower bound of integration from $x_{i-\frac{1}{2}}$ and $x_{i+\frac{1}{2}}$ as used in the conventional WENO scheme to $x_{i-\frac{1}{8}}$ and $x_{i+\frac{1}{8}}$ in this work.

In the literature, there are several variants proposed to compute the WENO nonlinear weights following the classical WENO scheme of Jiang and Shu [45], such as WENO-Z scheme [6], WENO-M scheme [32] and the WENO procedure of Shen and Zha [69, 70]. According to the analysis in [6], the classical WENO has accuracy loss in the smooth area near the discontinuity. The WENO-Z and WENO-M scheme are proposed to improve the accuracy of the classic WENO by using different nonlinear weights and smoothness measurements in the reconstruction. Especially, WENO-Z scheme shows good balance between numerical accuracy and algorithmic simplicity. Thus, we adopt the WENO-Z scheme in our WENO reconstruction and calculate the nonlinear weight

ω_j by

$$\omega_j = \frac{\alpha_j}{\sum_{k=0}^{2} \alpha_k}, \quad \alpha_j = \gamma_j \left(1 + \left(\frac{\tau_5}{\beta_j + \epsilon}\right)^p\right), \quad j = 0, 1, 2, \tag{4.40}$$

where ϵ equals to 10^{-40} and $\tau_5 = |\beta_2 - \beta_0|$. The value of p can be chosen flexibly to optimize the numerical property of the scheme. According to [6], increasing the value of p can make the scheme closer to the optimal central scheme for smooth function, but cause larger numerical dissipation near the discontinuities due to the less weighting of the discontinuous sub-stencil. In our numerical experiments, we use $p = 1.0$ in the computation unless stated explicitly. Finally, we can get the WENO reconstructed first order derivative $\tilde{Q}^{[1]}(x_i)$ by

$$\tilde{Q}_i^{[1]}(x_i) = \sum_{j=0}^{2} \omega_j q_j^{[1]}(x_i). \tag{4.41}$$

Remarks: As discussed above, the present WENO reconstruction is implemented in terms of the first-order derivative, and only projects the gradient at the cell center, which is substantially different from other existing limiting projections. Shown in our previous works [40, 95, 95, 96], the CIP-CSL3 formulation [96] provides a general framework to design new schemes by modifying the first-order derivative at the cell center. Desired numerical properties, such as oscillation-less and diffusion-less, can be easily obtained by projecting the first-order derivative with existing approximations, like the WENO in the present study as the most updated variant. We have explored to use this convenience in other approaches, such as the finite volume method and the standard DG method, but not reached a conclusion yet. In spite of the success of the CSL3 formulation, limiting projection for high-order local reconstructions still remains an unsolved issue.

It should be also noted that even though the present WENO scheme can effectively suppress numerical oscillations, it does not guarantee the positivity of the solution. Thus, slight under- or over-shoots may be observed in the numerical solutions. We examined the global maximum and minimum values in the numerical results of the following two advection tests.

Case 1: Advection of a square wave: The initial profile is given by

$$u(x,0) = \begin{cases} 1, & |x| \leqslant 0.4, \\ 0, & \text{otherwise}, \end{cases} \qquad x \in [-1,1]; \tag{4.42}$$

over a 100-cell mesh.

Case 2: Advection of a triangle wave [82]: In this test, an initial cone-shaped disturbance with a half-width of 10 cells is defined by

$$u(x,0) = \begin{cases} 1 - 20|x - 0.35|, & 0.3 \leqslant x \leqslant 0.4, \\ 0, & \text{otherwise}, \end{cases} \qquad x \in [0, 0.7]; \tag{4.43}$$

over a 70-cell mesh.

We carried out computation for one period advection, and show the global maximum and minimum values in Table 4.1. It can been seen that there is no overshoot for both cases even with discontinuities, whereas small undershoots are observed.

TABLE 4.1: Global min/max values in the numerical tests for CIP-CSL-WENO4 scheme.

Scheme	case 1		case 2	
	Max value	Min value	Max value	Min value
CIP-CSL-WENO4	1.0	-1.74e-22	1.0	-1.48e-16

In some applications, the positivity-preserving property becomes crucial [60], which should be able to be applied to CIP-CSL-WENO4 scheme as well.

As discussed above, the implementation of the present WENO limiter is efficient because the WENO limiter only needs to compute the first-order derivative at the cell center. To give a quantitative comparison, we measured the computational time of case 1 on a 1000-cell mesh for 10 periods by using the CIP-CSL-WENO4 scheme and the CIP-CSL3 scheme respectively. The elapse time on a PC with an Intel core-i5 processor (4 cores) for CIP-CSL-WENO4 scheme is 7.43s, while that for CIP-CSL3 scheme is 5.42s. It shows that the WENO limiter projection causes about a 27% overhead in the computational cost.

4.2.2 WENO limiter for 1D Euler equations

For the Euler system, the WENO reconstruction is carried out in terms of the characteristic variables. Firstly, we recover the PV of the primitive variables (ρ, v, p) at the cell center through equation (4.34). Then, the primitive variables $\mathbf{W} = (\rho, v, p)^T$ at the solution points used for the WENO reconstruction is mapped to the characteristic variables $\mathbf{C} = (c^{(1)}, c^{(2)}, c^{(3)})^T$ using the left eigenvectors of the Jacobian matrix $\overline{\mathbf{A}}_i$ computed from the VIA of the target cell Ω_i by

$$\mathbf{C}_j = \overline{\mathbf{L}}_i \mathbf{W}_j, \quad j = i-1,\ i-\frac{1}{2},\ i,\ i+\frac{1}{2},\ i+1, \tag{4.44}$$

and $\overline{\mathbf{L}}_i$ is a 3×3 matrix whose rows are the left eigenvectors of Jacobian matrix $\overline{\mathbf{A}}_i$. The explicit form of $\overline{\mathbf{L}}_i$ has been given in (4.23). The WENO reconstruction procedure introduced in previous subsection is then applied component-wisely to compute the 1st-order derivative $c_i^{(m)[1]}$, $m = 1, 2, 3$, of the characteristic variables $\mathbf{C}_i$ at the center of the target cell. The WENO-limited 1st-order derivatives of the characteristic variables are remapped back to the primitive variables using

$$\mathbf{W}_i^{[1]} = \overline{\mathbf{R}}_i \mathbf{C}_i^{[1]}, \tag{4.45}$$

where $\overline{\mathbf{R}}_i$ is a 3×3 matrix whose columns are the right eigenvectors of Jacobian matrix $\overline{\mathbf{A}}_i$.

Having obtained $\mathbf{W}_i^{[1]}$, we can construct the CIP-CSL3 interpolation function for each primitive variable by using the WENO-limited 1st-order derivatives as the constraint conditions. Finally, the moments are updated using the same procedure as given in section 4.1.2.2.

4.3 Comparison between Eulerian and semi-Lagrangian schemes

It is known that the semi-Lagrangian method has some advantages in comparison with the Eulerian method [76, 80], such as less restrictive CFL condition and superior numerical dissipation. Different from the conventional semi-Lagrangian schemes, the present scheme has rigorous numerical conservation. With both the trajectory and numerical flux being evaluated with the third-order Runge-Kutta method, we expect that the present scheme has a numerical accuracy comparable to the Eulerian variant in [95]. To demonstrate this, we compare the total errors, dissipation errors and dispersion errors between Eulerian MCV-WENO4 scheme [95] and the present CIP-CSL-WENO4 scheme through some benchmark tests for linear advection equation (4.1). The calculation of total errors, dissipation errors and dispersion errors are given in section 2.3 of Chapter 2

We compared three error measurements between MCV-WENO4 scheme and CIP-CSL-WENO4 scheme by the following benchmark tests for linear advection equation.

1. Advection of a square wave (case 1): This initial profile of this test is given in (4.42). The three measurements of errors are computed after one period ($t = 2.0$) on a mesh of 100 cells.

2. Advection of a triangle wave (case 2): We have introduced the initial structure of this test in (4.43). The numerical errors are computed up to $t = 0.7$.

3. Extrema of various smoothness (case 3): This test problem was proposed in [31]. The initial profile is given by

$$u(x+0.5,0) = \begin{cases} -x\sin(\frac{3}{2}\pi x^2), & -1 \leqslant x \leqslant -\frac{1}{3}, \\ |\sin(2\pi x)|, & |\frac{1}{3}| \leqslant x, \\ 2x - 1 - \sin(3\pi x)/6, & \text{otherwise}, \end{cases} \qquad x \in [-1,1]. \tag{4.46}$$

   The errors E_{TOT}, E_{DISS} and E_{DISP} are computed at $t = 2.0$ on a 100-cell mesh.

4. Jiang and Shu's test [45] (case 4): This test for linear advection equation has been widely used to verify the scheme's ability to capture the jump discontinuity while keeping the smooth profile with high accuracy. Initially, we have a profile defined by

$$u(x,0) = \begin{cases} \frac{1}{6}\left(G(x,\beta,z-\delta) + G(x,\beta,z+\delta) + 4G(x,\beta,z)\right), & -0.8 \leqslant x \leqslant -0.6, \\ 1, & -0.4 \leqslant x \leqslant -0.2, \\ 1 - |10(x-1)|, & 0.0 \leqslant x \leqslant 0.2, \\ \frac{1}{6}\left(F(x,\alpha,a-\delta) + F(x,\alpha,a+\delta) + 4F(x,\alpha,a)\right), & 0.4 \leqslant x \leqslant 0.6, \\ 0, & \text{otherwise}, \end{cases} \tag{4.47}$$

where the computation domain is $[-1,1]$. The function F and G is defined by

$$G(x,\beta,z) = \exp\left(-\beta(x-z)^2\right),\ F(x,\alpha,a) = \sqrt{\max(1-\alpha^2(x-a)^2, 0)}, \tag{4.48}$$

and the coefficients to determine the initial profile are given by

$$a = 0.5,\ z = 0.7,\ \delta = 0.005,\ \alpha = 10.0,\ \beta = \log 2/(36\delta^2). \tag{4.49}$$

We compute this test for one period ($t = 2.0$) on a 100-cell mesh.

In all these tests , we use the $CFL = 0.4$ for both MCV-WENO4 scheme and CIP-CSL-WENO4 scheme. We show all the error measurements E_{TOT}, E_{DISS} and E_{DISP} of advection tests from case 1 to case 4 in Table 4.2 and 4.3. All the results show that the CIP-CSL-WENO4 scheme of Semi-Lagrangian type is more accurate in comparison with the Eulerian MCV-WENO4 scheme.

TABLE 4.2: Comparison of E_{TOT},E_{DISS} and E_{DISP} between MCV-WENO4 scheme and CIP-CSL-WENO4 scheme for case 1 and case 2.

Scheme	case 1			case 2		
	E_{TOT}	E_{DISS}	E_{DISP}	E_{TOT}	E_{DISS}	E_{DISP}
MCV-WENO4	2.97e-03	1.37e-04	2.83e-03	1.32e-04	2.70e-06	1.30e-04
CIP-CSL-WENO4	1.85e-03	6.59e-05	1.78e-03	3.33e-05	5.06e-07	3.28e-05

TABLE 4.3: Same Table 4.2, but for case 3 and case 4.

Scheme	case 3			case 4		
	E_{TOT}	E_{DISS}	E_{DISP}	E_{TOT}	E_{DISS}	E_{DISP}
MCV-WENO4	8.52e-03	9.54e-04	7.57e-03	3.62e-03	4.88e-04	3.13e-03
CIP-CSL-WENO4	6.23e-03	7.51e-04	5.48e-03	2.14e-03	1.78e-04	1.95e-03

In order to compare the computational efficiency of the two schemes, we measured the elapse times using the same case as in (4.42) on a 1000-cell mesh by both CIP-CSL-WENO4 scheme and MCV-WENO4 scheme on a PC with with an Intel core-i5 processor of four cores. The elapse time of CIP-CSL-WENO4 scheme for 10-period computation is $7.43s$, while that of MCV-WENO4 is $10.63s$. It is seen that the load for semi-Lagrangian approach is smaller than Eulerian approach. We may owe this in part to the fact that even though the three-step Runge-Kutta time stepping is used in both schemes, the WENO reconstruction is conducted for only once in CIP-CSL-WENO4 but three times in MCV-WENO4. More importantly, the CIP-CSL-WENO4 can use larger CFL number. Theoretically, the maximum CFL number of CIP-CSL-WENO4 scheme can be infinite. In our computation, the maximum allowable CFL number for CIP-CSL-WENO4 scheme is 1.0, while for MCV-WENO4 scheme, it is 0.6. It reveals the significant advantage of CIP-CSL-WENO4 in computational efficiency.

It is noted that even though the present CIP-CSL-WENO4 scheme uses only the neighboring cells as the stencil to build the spatial discretization, which limits the CFL number being less than one for computational stability, a scheme that allows CFL$>$1.0 can be devised straightforwardly in the spirit of semi-Lagrangian scheme. Meanwhile, attention must be paid when the characteristic speeds are variable. In this case, new stability condition has to be built in terms of the so-called Lipschitz number or deformational CFL number [76].

4.4 Numerical experiments

To illustrate the robustness and accuracy of the CIP-CSL-WENO4 method, we compute the numerical results for some widely used benchmark tests in this section.

4.4.1 1D linear advection equation

The linear advection equation has been given in (4.1). We set $a = 1$ in all our numerical examples. The numerical tests with different initial profiles to verify the convergence rate and oscillation-suppressing property of CIP-CSL-WENO4 scheme are given in this subsection. The CFL number equals to 0.8 in all our examples. In some cases, we have tested the numerical scheme on both uniform and nonuniform meshes. The nonuniform meshes are created in the same way as introduced in [112], i.e. a random variation d was specified to the size of each mesh cell by adjusting the cell boundaries as $x_{i+\frac{1}{2}} + d(r_{i+\frac{1}{2}} - 0.5)\Delta x$, where $x_{i+\frac{1}{2}}$ and Δx are the cell boundaries and spacing of the uniform grid. $r_{i+\frac{1}{2}}$ is a random number of uniform distribution ranging from 0 to 1.

Example 4.1. **Accuracy test for 1D advection equation.** In this test problem, we examine the convergence rate of our scheme by using the grid refinement. Initially, the smooth profile is set to be $u(x, 0) = \sin(\pi x),\ x \in [-1, 1]$. The L_1 and L_∞ errors of VIA at $t = 2.0$ (after one period) are calculated with different grid resolution. The mesh number is doubly increased from 20 to 320.

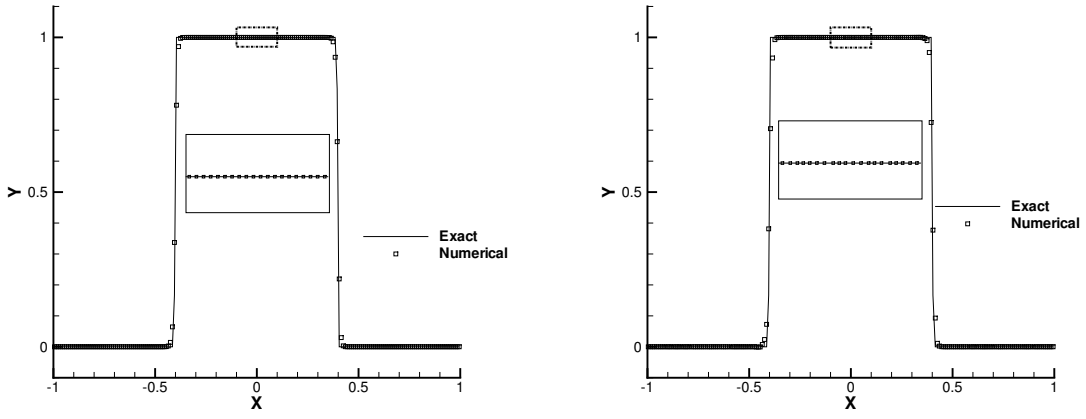

(a) Uniform meshes (b) Nonuniform meshes

FIGURE 4.2: Numerical results of the advection of a square wave on a uniform (a) and nonuniform (b) meshes. Part of the region is enlarged to clarify the difference in two meshes.

In Table 4.4, we show the numerical errors and convergence rates of CIP-CSL-WENO4 scheme and Eulerian MCV-WENO4 scheme. Also, we give the numerical results with

and without WENO limiter in Table 4.5. It can be clearly observed that our scheme perfectly converges up to 4th order accuracy, and the use of WENO limiter can maintain both the convergence rate and magnitude of numerical errors. Moreover, the magnitude of both L_1 and L_∞ errors for CIP-CSL-WENO4 scheme are less than 10% of the MCV-WENO4 scheme which uses a smaller CFL number of 0.4.

TABLE 4.4: Numerical errors and convergence rates for 1D advection equation, $t = 2.0$.

N	CIP-CSL-WENO4 scheme				MCV-WENO4 scheme			
	L_1 error	Order	L_∞	Order	L_1 error	Order	L_∞	Order
20	4.39e-06		6.65e-06		4.95e-05		7.72e-05	
40	2.74e-07	4.00	4.29e-07	3.95	3.12e-06	3.98	4.88e-06	3.98
80	1.72e-08	4.00	2.69e-08	3.99	1.96e-07	3.99	3.07e-07	3.99
160	1.07e-09	4.00	1.69e-09	4.00	1.23e-08	4.00	1.92e-08	4.00
320	6.73e-11	4.00	1.06e-10	4.00	7.67e-10	4.00	1.20e-09	4.00

TABLE 4.5: Numerical errors and convergence rate for 1D advection equation at $t = 2.0$.

N	CIP-CSL-WENO4 scheme				CIP-CSL3 scheme			
	L_1 error	Order	L_∞	Order	L_1 error	Order	L_∞	Order
20	4.39e-06		6.65e-06		4.43e-06		6.93e-06	
40	2.74e-07	4.00	4.29e-07	3.95	2.74e-07	4.02	4.31e-07	4.01
80	1.72e-08	4.00	2.69e-08	3.99	1.72e-08	3.99	2.69e-08	4.00
160	1.07e-09	4.00	1.69e-09	4.00	1.07e-09	4.00	1.69e-09	4.00
320	6.73e-11	4.00	1.06e-10	4.00	6.73e-11	4.00	1.06e-10	4.00

The results for nonuniform meshes are shown in Table 4.6. Here the random variation d is set to be 0.2. We can see even though the magnitude of numerical error is sightly larger than that on uniform meshes, the convergence rate can be maintained.

TABLE 4.6: Numerical errors and convergence rates of CIP-CSL-WENO4 scheme for 1D advection equation on nonuniform meshes at $t = 2.0$.

N	L_1 error	Order of Accuracy	L_∞ error	Order of Accuracy
20	4.45e-06		6.93e-06	
40	2.83e-07	4.00	4.45e-07	3.96
80	1.77e-08	4.00	2.80e-08	3.99
160	1.11e-09	3.99	1.75e-09	4.00
320	6.92e-11	4.00	1.10e-10	4.00

To demonstrate the impact of CFL number, we give the numerical errors computed with CFL $= 0.2$ and CFL $= 0.4$ in Table 4.7. We can clearly see that even though the

magnitude of the numerical errors are different, the 4th order accuracy can be achieved for these two cases.

TABLE 4.7: Numerical errors and convergence rates for 1D advection equation of CIP-CSL-WENO4 scheme with different CFL numbers.

N	CFL = 0.2				CFL = 0.4			
	L_1 error	Order	L_∞	Order	L_1 error	Order	L_∞	Order
20	1.79e-05		2.72e-05		6.02e-06		1.03e-05	
40	1.11e-06	4.01	1.73e-06	3.97	2.57e-07	4.55	3.97e-07	4.69
80	6.90e-08	4.00	1.08e-07	4.00	1.39e-08	4.20	2.19e-08	4.18
160	4.31e-09	4.00	6.77e-09	4.00	8.36e-10	4.06	1.31e-09	4.18

Example 4.2. **Advection of a square wave.** As the test to examine the capability to capture jump discontinuities, we computed the advection of a square wave. The initial profile is given by

$$u(x,0) = \begin{cases} 1, & |x-1| \leqslant 0.4, \\ 0, & \text{otherwise}. \end{cases} \tag{4.50}$$

The computational domain is set to be $[0,2]$. The numerical results computed on both uniform and nonuniform meshes of 200 cells at $t = 2.0$ are shown in Fig. 4.2. The random variation is set to be 0.5 in this example. We can see that our scheme is able to accurately resolve the jump discontinuities.

Example 4.3. **Jiang and Shu's test [45].** The set-up of this benchmark test has been defined in (4.47). The numerical results after one period are given in Fig. 4.3. Here the mesh number is 200. It can be observed that our numerical solutions are free of spurious oscillations near discontinuities and preserve the high accuracy for smooth profile.

In this tests, we also give the numerical solutions computed with CFL $= 0.2$ and CFL $= 0.4$ to verify the CFL-independent property of our scheme. The numerical results are given in Fig.4.4. We learn from our numerical solutions given here that the value of the CFL number only has minor influence on the resolution of the computational results.

Example 4.4. **Extrema of various smoothness.** The initial profile of this test has been given in (4.46).

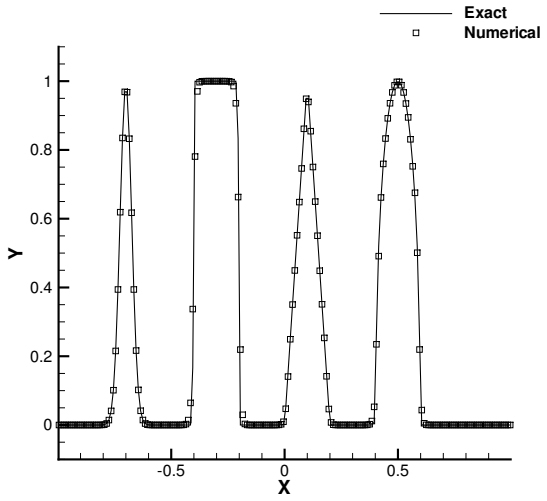

FIGURE 4.3: Numerical results of Jiang and Shu's test at $t = 2.0$ on a 200 cell-mesh.

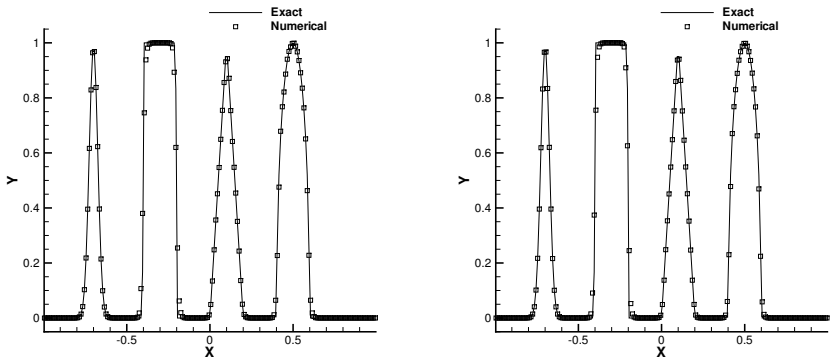

FIGURE 4.4: Numerical results of Jiang and Shu's test computed with CFL $= 0.2$ (left) and CFL $= 0.4$ (right).

We transport the initial irregular profile until $t = 8.0$ (after 4 periods) on a 100-cell mesh. Compared with the numerical results in [40], our results in Fig. 4.5 show well-resolved extrema without numerical oscillations near the discontinuities.

4.4.2 2D implementation

The implementation of semi-Lagrangian schemes in multi-dimensions can be carried out by the Strang splitting for simplicity and computational efficiency using the 1D scheme as the building block. We show the numerical results of transporting a complex distribution by the 2D linear advection equation with a solid-rotating velocity field.

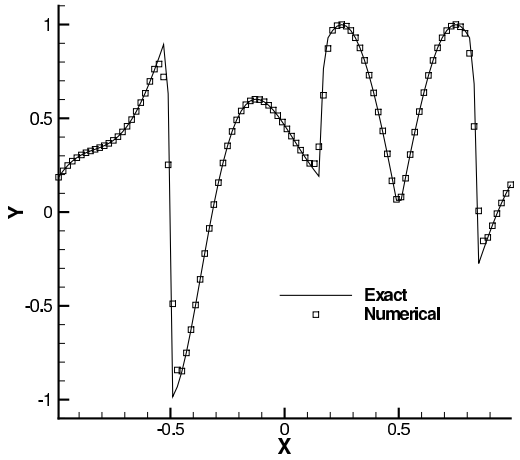

FIGURE 4.5: Numerical results of the extrema of various smoothness at $t = 8.0$ on a 100-cell mesh.

Example 4.5. **2D Rotation test.** In this test, the 2D complex initial profile is given by

$$u(x,y,0) = \begin{cases} \dfrac{1}{6}\left(G(r_1+\delta,\beta)+G(r_1-\delta,\beta)+4G(r_1,\beta)\right), & |r_1| \leqslant 0.2, \\ 1, & |x| \leqslant 0.2, \ \ -0.7 \leqslant y \leqslant -0.3, \\ 1-|5r_2|, & |r_2| \leqslant 0.2, \\ \dfrac{1}{6}\left(F(r_3+\delta,\alpha)+F(r_3-\delta,\alpha)+4F(r_3,\alpha)\right), & |r_3| \leqslant 0.2, \\ 0, & \text{otherwise}, \end{cases} \tag{4.51}$$

where

$$r_1 = \sqrt{(x+0.6)^2+y^2},\ r_2 = \sqrt{(x-0.6)^2+y^2},\ r_3 = \sqrt{x^2+(y-0.6)^2},$$

and $G(r,\beta) = \exp(-\beta r^2)$, $F(r,\alpha) = \sqrt{\max(1-\alpha^2 r^2, 0)}$. As in [41], the coefficients are set to be $\delta = 0.01$, $\alpha = 5$ and $\beta = \log 2/(36\delta^2)$. The velocity field is defined by $(v_1, v_2) = (-2\pi y, 2\pi x)$ on a computation domain of $[-1,1]^2$. Our computation was executed up to $t = 1.0$ on a grid of 100×100 cells. The numerical results are shown in Fig. 4.6.

It can be observed that the shape of the solid body is well resolved, and there are no

visible oscillations near the jump discontinuities. The geometric shapes of the distribution have been faithfully preserved as a result of the superior dispersion property of the CIP-CSL-WENO4 scheme.

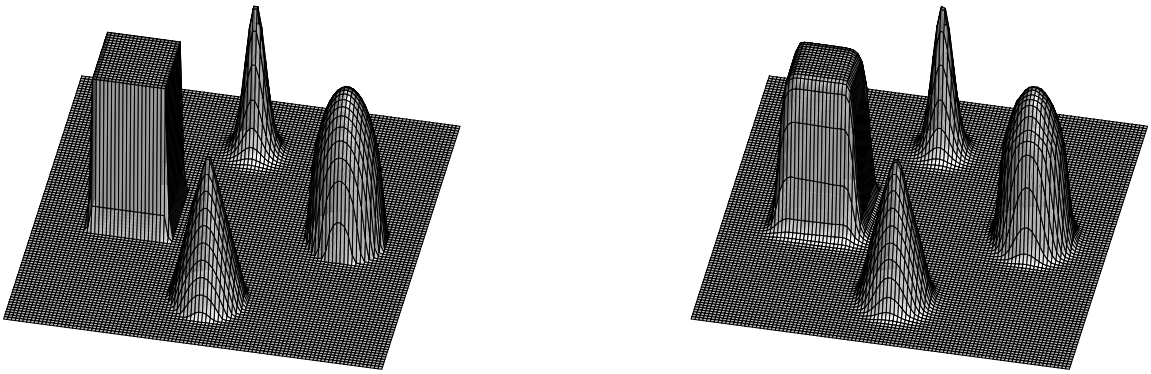

(a) Initial profile (b) Numerical results

FIGURE 4.6: Numerical results of the solid-rotation of a complex profile on a mesh of 100×100 cells.

It should be notified that semi-Lagrangian scheme which relies on the dimensional splitting for multi-dimensional implementation has substantial difficulty for unstructured grids. Moreover, implementing a semi-Lagrangian scheme for the full Euler equations in multi-dimensions meets other complexities, such as the computation of Mach cone. Nevertheless, the strength of semi-Lagrangian method in numerical accuracy and CFL stability makes it attractive in some particular applications.

4.4.3 1D inviscid Burgers equation

The 1D inviscid Burgers equation is defined as

$$u_t + \left(\frac{u^2}{2}\right)_x = 0, \tag{4.52}$$

which can be written in an advection form

$$u_t + a(u)u_x = 0, \tag{4.53}$$

where $a(u) = u$ is the characteristic speed. In order to avoid the "entropy problem" at the sonic point, we modify the characteristic speed at the cell boundary $x_{i+\frac{1}{2}}$ by

$$a(u)_{i+\frac{1}{2}} = \begin{cases} \text{sgn}(\max)\max(|u_{i+\frac{1}{2}}|, |\frac{1}{2}(u_{i+1}+u_i)|), & \text{for sonic point,} \\ u_{i+\frac{1}{2}}, & \text{otherwise.} \end{cases} \tag{4.54}$$

We tested the performance of our scheme to solve Burgers equation for benchmark tests with different initial conditions. *Example 4.6.* **Burgers equation with a sine wave**

TABLE 4.8: Numerical errors and convergence rates for 1D Burgers equation at $t = 1/(2\pi)$.

N	L_1 error	Order of Accuracy	L_∞ error	Order of Accuracy
10	3.91e-04		2.62e-03	
20	4.28e-05	3.19	2.70e-04	3.28
40	3.44e-06	3.63	3.03e-05	3.15
80	2.53e-07	3.77	2.25e-06	3.75
160	2.01e-08	3.66	2.27e-07	3.31

initial condition. The initial smooth profile is given by $u(x,0) = 0.5 + \sin(\pi x)$. The solution remains smooth up to $t = 1.0/\pi$, and then the shock wave starts to develop and becomes a full discontinuity at $t = 1.5/\pi$. Firstly, we carried out the computation up to $t = 0.5/\pi$ with different grid resolutions. The L_1 and L_∞ errors of VIA are shown in Table 4.8, along with the convergence rate. It is clear that for 1D Burgers equation, our scheme can achieve 4th order accuracy as expected, which can demonstrate the time-depending accuracy of our scheme. We also give the numerical solutions on a 100-cell mesh at $t = 1.5/\pi$ in Fig. 4.7. We can see that our scheme can resolve the whole solution with high quality, and there is no oscillation near the shock, which verifies the effectiveness of the presented WENO limiter.

Example 4.7. **Burgers equation with shock and rarefaction waves.** This benchmark test for 1D inviscid Burgers equation contains both shock and rarefaction waves. The initial profile is a square wave given by

$$u(x,0) = \begin{cases} 1, & 0.3 \leqslant x \leqslant 0.75, \\ 0.5, & \text{otherwise,} \end{cases} \tag{4.55}$$

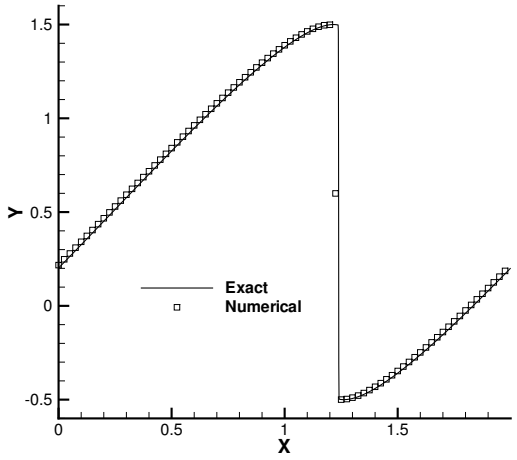

FIGURE 4.7: Numerical results of Burgers equation at $t = 1.5/\pi$ on a 100-cell mesh.

on computational domain $[0, 1]$. The numerical results at $t = 0.2$ computed on a mesh of 80 cells are shown in Fig. 4.8. Our numerical solutions can well resolve the shock wave without generating any spurious oscillation, and for the expansion wave there is no significant dissipation.

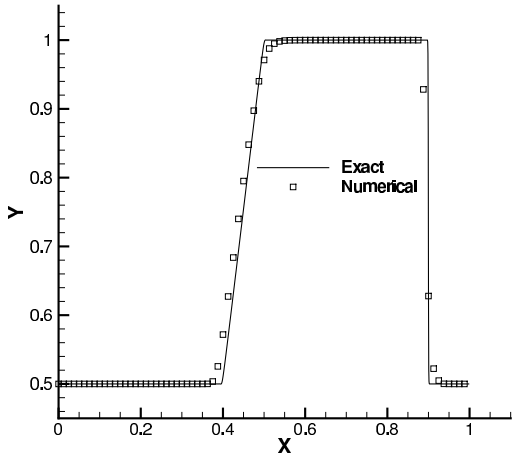

FIGURE 4.8: Numerical results of Burgers equation with a shock and rarefaction wave at $t = 0.2$ on a 80-cell mesh.

4.4.4 1D Euler equations

In this section, we report the benchmark tests to verify the performance (convergence rate, stability and oscillation-suppressing property) of our scheme for 1D Euler equations.

Example 4.8. **Accuracy test for 1D Euler equations.** Firstly, we check the convergence rate of the scheme for 1D Euler equations through the propagation of a smooth density perturbation. The initial condition is given by

$$\rho(x,0) = 1 + 0.2\sin(\pi x),\ v(x,0) = 1.0,\ p(x,0) = 1.0, \quad x \in [0,2]. \tag{4.56}$$

Here we impose the periodic boundary condition. We show the L_1 and L_∞ errors of VIA of density with the grid resolution refined from 20 to 320 in Table 4.9. As expected, our scheme is uniformly converged to $4th$ order accuracy for the Euler equations with variable characteristic velocities.

TABLE 4.9: Numerical errors and convergence rate for 1D Euler equations, $t = 2.0$

N	L_1 error	Order of Accuracy	L_∞ error	Order of Accuracy
20	3.14e-04		5.41e-04	
40	1.94e-05	4.02	3.04e-05	4.16
80	1.10e-07	4.14	1.72e-06	4.14
160	5.57e-08	4.30	8.74e-08	4.30
320	2.21e-08	4.66	3.47e-09	4.66

Example 4.9. **Sod's and Lax's problem.** Here we show the numerical results for two shock tube problems originally proposed in [49, 74, 77]. For Sod's problem, the initial distribution is given by

$$(\rho_0, v_0, p_0) = \begin{cases} (1,0,1), & 0 \leqslant x \leqslant 0.5, \\ (0.125,0,0.1), & \text{otherwise.} \end{cases} \tag{4.57}$$

For Lax's problem, the initial profile is given by

$$(\rho_0, v_0, p_0) = \begin{cases} (0.445, 0.698, 3.528), & 0 \leqslant x \leqslant 0.5, \\ (0.5,0,0.571), & \text{otherwise.} \end{cases} \tag{4.58}$$

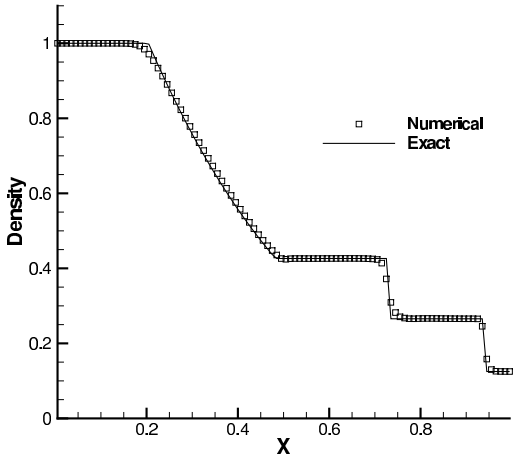

FIGURE 4.9: Numerical results of Sod's problem at $t = 0.25$ with 100 cells.

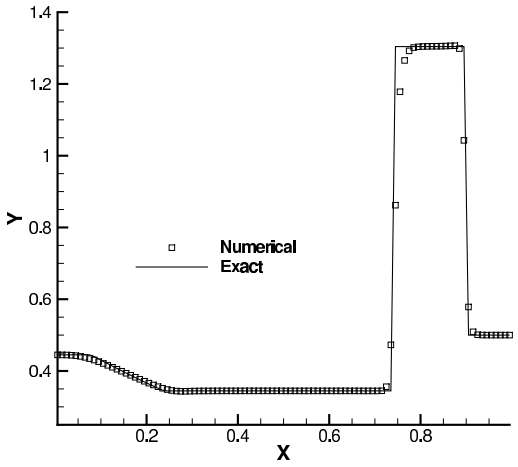

FIGURE 4.10: Numerical results of Lax's problem at $t = 0.16$ with 100 cells.

For both tests we use a mesh of 100 cells. In Sod's problem, the computation is carried out up to $t = 0.25$. The numerical results shown in Fig. 4.9 reveal that our scheme can capture the contact discontinuity and shock wave with correct position and satisfactory sharpness. In Lax's problem, we conducted the computation until $t = 0.16$. Similar to Sod's problem, our numerical results in Fig. 4.10 can resolve the contact discontinuity with high resolution, while the oscillations near the shock wave and discontinuity are effectively eliminated.

Example 4.10. **Symmetry expansion wave.** This test problem describes an isentropic process where the flow field is split by a divergent velocity field [84]. Initially, we have the following state condition

$$(\rho_0, v_0, p_0) = \begin{cases} (1, -2, 0.4), & 0 \leqslant x \leqslant 0.5, \\ (1, 2, 0.4), & \text{otherwise.} \end{cases} \tag{4.59}$$

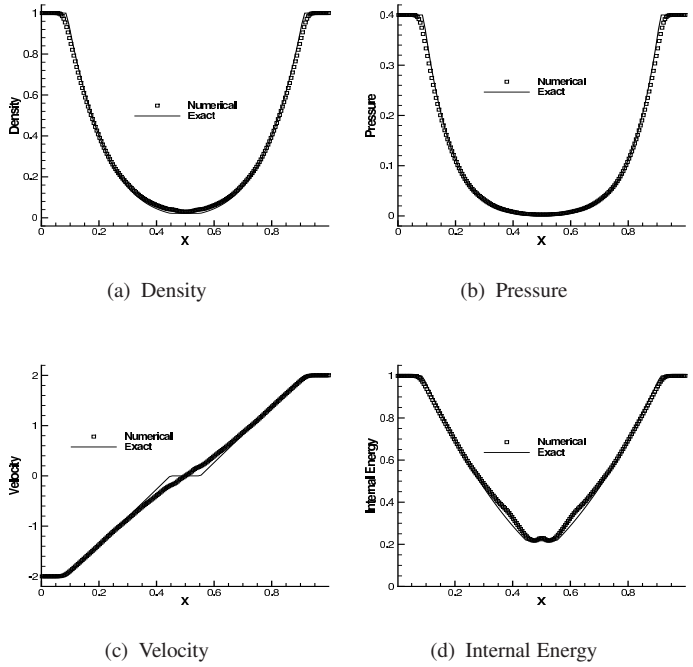

(a) Density (b) Pressure

(c) Velocity (d) Internal Energy

FIGURE 4.11: Numerical results of symmetrical expansion wave at $t = 0.15$ with 200 cells.

The numerical solutions of density, velocity, pressure and internal energy at $t = 0.15$ with 200 cells are shown in Fig. 4.11. For such a test with very low density and pressure, our scheme successfully reproduces all the physical fields with high quality.

Example 4.11. **Shock-turbulence interaction.** This benchmark test proposed in [73] includes the interaction of a Mach 3 shock with a density perturbation. The initial profile is given by

$$(\rho_0, v_0, p_0) = \begin{cases} (3.857143, 2.629369, 10.333333), & 0 \leqslant x \leqslant 0.1, \\ (1.0 + 0.2\sin(50x - 25), 0, 1.0), & \text{otherwise.} \end{cases} \tag{4.60}$$

For this test, a shock wave initially located at $x = 0.1$ moves right and interacts with the density perturbation superimposed by a sine wave. The numerical results at $t = 0.18$ are shown in Fig. 4.12. The mesh number for this test problem is 200. The density disturbance in the numerical solution has been resolved correctly without obvious diffusion. For the shock wave near $x = 0.75$, there are no visible spurious oscillations thanks to the WENO limiter.

Example 4.12. **Stationary contact discontinuity.** The initial condition of this test is given by

$$(\rho_0, v_0, p_0) = \begin{cases} (1.4, 0, 1), & 0 \leqslant x \leqslant 0.1, \\ (1, 0, 1), & \text{otherwise.} \end{cases} \tag{4.61}$$

The contact discontinuity defined at the initial condition will remain stationary during the whole computational time. For some high resolution schemes, it is not a trivial issue to keep the sharpness of the discontinuity for this benchmark test [84]. Here we carried out the computation up to $t = 2.0$. The mesh number is 100. The numerical results are shown in Fig. 4.13. We can see that our scheme is able to keep the density jump with the initial sharpness.

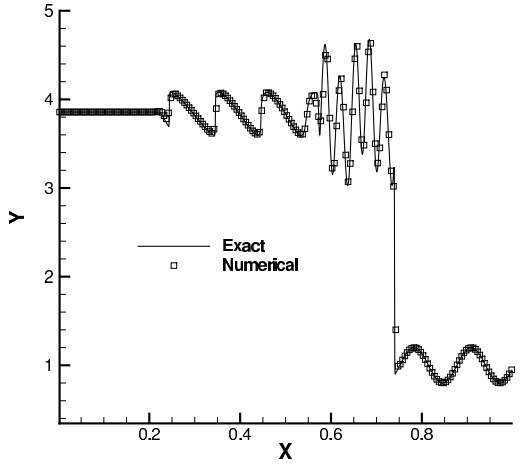

FIGURE 4.12: Numerical results of shock-turbulence interaction at $t = 0.18$ with 200 cells.

Example 4.13. **Two interacting blast waves.** This test was originally proposed by Wooward and Colella in [94]. The initial profile is given by

$$(\rho_0, v_0, p_0) = \begin{cases} (1, 0, 1000), & 0 \leqslant x \leqslant 0.1, \\ (1, 0, 0.01), & 0.1 < x < 0.9, \\ (1, 0, 100), & \text{otherwise}. \end{cases} \tag{4.62}$$

Reflection boundary conditions are imposed on the two ends of the computational domain to generate multiple interactions of different waves, which result in complex structures in the solution.

As in [40], we modified the characteristic velocities at the cell boundary by a weighted averaging between the values of the PVs $\lambda_m(x_{i+\frac{1}{2}})$ and the values computed by the Roe's average [67] based on the VIAs of two neighboring cells, i.e.

$$\hat{\lambda}_m(x_{i+\frac{1}{2}}) = \beta\lambda_m(x_{i+\frac{1}{2}}) + (1-\beta)\overline{\lambda}_m^{Roe}(\overline{u_i}, \overline{u_{i+1}}). \tag{4.63}$$

We set the weight parameter β to be 0.5 for current example as recommended in [40]. The value of p in (4.40) is set to be 1.5 to introduce more numerical dissipations around the strong discontinuities. The numerical results of density at $t = 0.038$ on a 400-cell mesh are plotted in Fig.4.14 against the reference solution computed by an FVM with MUSCL reconstruction on a grid of 4000 cells.

The numerical results shown in Fig.4.14 accurately capture the shock wave and contact discontinuity with correct positions. The numerical solutions look superior to most existing finite volume WENO schemes on 400-cell mesh and other high-order local reconstruction-based schemes of equivalent DOFs. More importantly, there is no any TVB switching in the present computation to control the numerical dissipation.

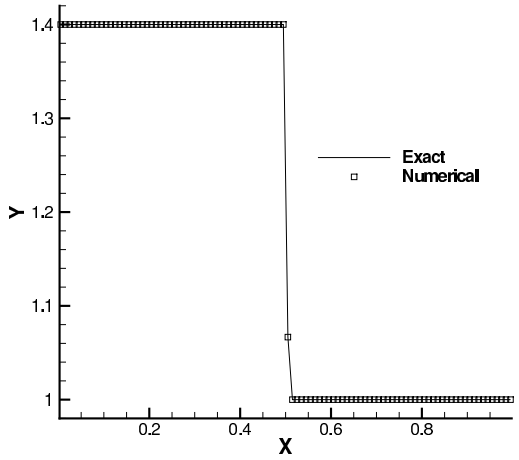

FIGURE 4.13: Numerical results of stationary contact discontinuity at $t = 2.0$ with 100 cells.

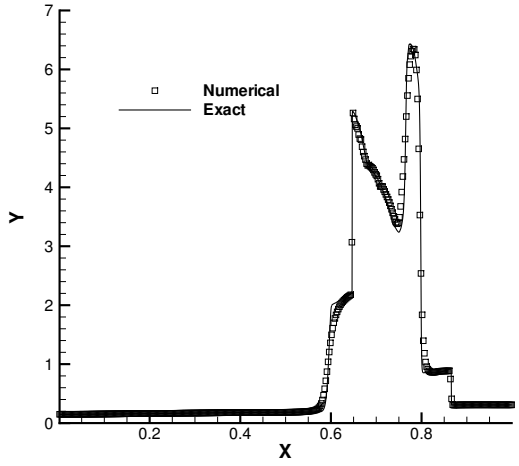

FIGURE 4.14: Numerical results of two interacting blast waves at $t = 0.038$ with 400 cells.

4.5 Summary

In this chapter, we present a nodal value based WENO limiter for CIP/MM FVM scheme. The WENO limiter uses local DOFs available in the target cell and its immediate neighboring cells, which minimizes the WENO interpolation stencil. The present method is substantially different from other existing implementations of WENO projection to local high-order reconstructions that only use the VIA in WENO reconstruction, while ignoring other available sub-cell information, and thus result in wider stencils.

The proposed scheme, which is called CIP-SCL-WENO4 scheme, is free of the ad hoc TVB criterion which is needed in nearly all existing schemes to control the excessive numerical dissipation. Moreover, the present scheme is algorithmically simple and computationally efficient.

As substantiated in the chapter, the semi-Lagrangian formulation is more accurate in terms of both dissipation and dispersion errors in comparison with the Eulerian scheme. Of more practical significance in applications, the presented scheme allows a large CFL number in principle for the computational stability.

The $4th$ order convergence rate has been verified for both scalar and Euler conservation laws. Furthermore, the numerical results of some widely used benchmark tests show that the present method is able to get the high-quality solutions among the best ever reported of the numerical schemes with similar number of DOFs.

The present scheme can been seen as a more consistent formulation that well balances different requirements for a high resolution scheme, such as local high-order reconstruction and limiting projection, numerical accuracy and computational efficiency.

Chapter 5

BVD algorithm for MCV-WENO4 method

In this chapter, we combine the BVD reconstruction with the MCV-WENO4 scheme of MMC-FR formulation presented in Chapter 3 as a trial to employ the BVD concept to the HLR method. The modified version of BVD algorithm for MCV-WENO4 scheme will be discussed at first, followed by the building-block schemes for new scheme, which is called the BVD-MCV-WENO4 scheme in this Chapter. Finally, we will give some preliminary numerical results and end the chapter with the summary of this work.

5.1 Numerical algorithm

We start from the following scalar conservation law

$$\frac{\partial u}{\partial t} + \frac{\partial f}{\partial x} = 0. \tag{5.1}$$

Here $u(x)$ is the solution function, and $f(u)$ is the flux function. We divide the computational domain into I non-overlapping cells $\Omega_i = [x_{i-\frac{1}{2}}, x_{i+\frac{1}{2}}]$ and 3 solution points $x_{ik},\ k = 1, 2, 3$ are equidistantly located inside cell Ω_i, i.e $x_{i1} = x_{i-\frac{1}{2}},\ x_{i2} = (x_{i-\frac{1}{2}} + x_{i+\frac{1}{2}})/2,\ x_{i3} = x_{i+\frac{1}{2}}$. As introduced in Chapter 3, the solution points can be updated

by the following semi-discretized equation

$$\frac{du_{ik}}{dt} = -\left(\frac{d\hat{f}_i(x)}{dx}\right)_{ik}, \quad k = 1, 2, 3. \tag{5.2}$$

By using the quadratic Lagrangian interpolation in primary reconstruction of flux function, we can get the MCV3 scheme. Additionally, the first order derivative at the cell center $f_x^{[1]}(x_i)$ can be added as another constraint condition in primary reconstruction, which is referred as the MCV-SC scheme in Chapter 3. The $f_x^{[1]}(x_i)$ can be also reconstructed using a PV-based WENO limiter originally presented in Chapter 3 , which leads to the the MCV-WENO4 scheme.

The flux reconstruction of MCV-WENO4 scheme is implemented by imposing the following constraint conditions, just as introduced in Chapter 3

$$\begin{cases} \hat{f}_i(x_{i\pm\frac{1}{2}}) = f_i(u_{i\pm\frac{1}{2}}), \\ \hat{f}_{xi}^{[1]}(x_{i\pm\frac{1}{2}}) = f_{xi}^{[1]B}(x_{i\pm\frac{1}{2}}) \end{cases} \tag{5.3}$$

As the primary reconstructed flux function is continuous at the cell boundary, we only need to approximate the first order derivative value at the cell boundary, which is the solution of the Derivative Riemann problem. Because continuity of PV at cell boundary is naturally satisfied for MCV-WENO4 scheme, i.e. $BV \equiv 0$ during the computation, the original FVM-type BVD reconstruction is not applicable for MCV-type method. As a result, we want to develop a new version of BVD method that is suitable for MCV-type method. The algorithm of BVD reconstruction will be discussed in the following paragraph.

5.1.1 BVD algorithm for MCV-WENO4 scheme

In order to apply the BVD algorithm for MCV-WENO4 scheme, firstly we extend the the definition of BV by including the high-order derivatives as

$$BV(u)_{i+\frac{1}{2}}^{[m]} = |u_{i+\frac{1}{2}}^{R[m]} - u_{i+\frac{1}{2}}^{L[m]}|, m = 0, 1, \cdots, n. \tag{5.4}$$

Here the superscript refers to the mth derivative of solution function at the cell boundary. When m equals to zero, we can get the original definition of BV used in FVM.

Then the BVD algorithm for MCV-WENO4 scheme can be proceeded as follows

i) Initially, we have two interpolation function $\Phi_i^{<1>}(x)$ and $\Phi_i^{<2>}(x)$, of solution function $u(x)$ which is reconstructed from the solution points u_{ik} inside cell i Suppose $\Phi_i^{<1>}(x)$ to be MCV-WENO4 method that uses high-order polynomial reconstruction, while $\Phi_i^{<2>}(x)$ should be the reconstruction that can better represent the step-like solutions. The building-block scheme for BVD algorithm will be discussed in the next section.

ii) Select from $\Phi_i^{<p>}(x)$ and $\Phi_{i+1}^{<q>}(x)$ with p and q being 1 and 2, to make sure that the boundary variation of first order derivative

$$BV(u)_{i+\frac{1}{2}}^{[1]} = |\Phi_i^{<p>[1]}(x_{i+\frac{1}{2}}) - \Phi_{i+1}^{<q>[1]}(x_{i+\frac{1}{2}})| \tag{5.5}$$

is minimized.

iii) The same selection procedure is also applied to the neighboring interface $x_{i-\frac{1}{2}}$, that is, $q^{'}$ and $p^{'}$ is found to minimize

$$BV(u)_{i-\frac{1}{2}}^{[1]} = |\Phi_i^{<p^{'}>[1]}(x_{i-\frac{1}{2}}) - \Phi_{i-1}^{<q^{'}>[1]}(x_{i-\frac{1}{2}})| \tag{5.6}$$

If the choice for left and right side of cell i is different when applying step ii), i.e. for $\Phi_i^{<p>[1]}(x_{i+\frac{1}{2}})$ and $\Phi_i^{<p^{'}>[1]}(x_{i-\frac{1}{2}})$, $p \neq p^{'}$, then the following monotonicity criterion is needed to uniquely determine the reconstructed $1st$ order derivative as

$$\Phi_i^{<p>}(x) = \begin{cases} \Phi_i^{<1>[1]}(x), \text{ if } \left(\Phi_i^{<p>}(x_{i+\frac{1}{2}}) - \Phi_{i+1}^{<q>[1]}(x_{i+\frac{1}{2}})\right)\left(\Phi_{i-1}^{<p'>[1]}(x_{i-\frac{1}{2}}) - \Phi_i^{<q'>[1]}(x_{i-\frac{1}{2}}\right) < 0, \\ \\ \Phi_i^{<2>}(x), \text{ otherwise.} \end{cases} \tag{5.7}$$

iv) The left- and right-side value for each cell i can be given by

$$u_{i+\frac{1}{2}}^{L[1]} = \Phi_i^{<p>[1]}(x_{i+\frac{1}{2}}) \text{ and } u_{i-\frac{1}{2}}^{R[1]} = \Phi_i^{<p>[1]}(x_{i-\frac{1}{2}}). \tag{5.8}$$

Remark 1. The derivative of flux function at the cell boundary can be expressed in terms of the derivative of solution function through the linearizion procedure as follows

$$f^{[1]} = Au^{[1]} \tag{5.9}$$

where A is the Jacobian matrix obtained by $A = \frac{\partial f}{\partial u}$.

Remark 2. The numerical approximation of flux function at the cell boundary $x_{i+\frac{1}{2}}$ can be calculated by

$$\tilde{f}^{[1]}_{i+\frac{1}{2}} = \frac{1}{2}\left(f^{[1]L}_{i+\frac{1}{2}} + f^{[1]R}_{i+\frac{1}{2}} - R_{i+\frac{1}{2}}|\Lambda|L_{i+\frac{1}{2}}(u^{[1]R}_{i+\frac{1}{2}} - u^{[1]L}_{i+\frac{1}{2}})\right) \tag{5.10}$$

From above equation we can see that the minimization of $BV^{[1]}$ can effectively reduce the numerical dissipation term $R_{i+\frac{1}{2}}|\Lambda|L_{i+\frac{1}{2}}(u^{[1]R}_{i+\frac{1}{2}} - u^{[1]L}_{i+\frac{1}{2}})$, which means the numerical viscosity of the scheme can be minimized.

5.1.2 The Buiding-block reconstruction schemes

For BVD reconstruction algorithm, we need two reconstruction methods $\Phi_i^{<1>}(x)$ and $\Phi_i^{<2>}(x)$. In this study, we use the MCV-WENO4 scheme developed in Chapter 3 to recover the smooth solution, while the THINC reconstruction is used as the candidate reconstruction method $\Phi_i^{<2>}(x)$ to resolve the sharp discontinuity.

5.1.2.1 The MCV-WENO4 reconstruction for $\Phi_i^{<1>}(x)$

The reconstruction of MCV-WENO4 scheme follows what has been described in Chapter 3. The primary reconstruction is performed inside each side by using PVs at three solution points and $1st$ order derivative at the cell center, where the $1st$ order derivative is reconstructed by using the PV-based WENO limiter presented in the same Chapter. Then, the $1st$ order derivative at the cell boundary can be obtained from the derivative of the primary reconstruction function, which will be used in step ii) of BVD algorithm for MCV-WENO4 scheme as one candidate reconstruction $\Phi_i^{<1>}(x)$ that is of high order accuracy for smooth solutions.

5.1.2.2 The THINC reconstruction for $\Phi_i^{<2>}(x)$

For the reconstruction of $\Phi_i^{<2>}(x)$, the use of THINC reconstruction is slight different from the one presented for FVM-type BVD scheme. Here the THINC reconstruction is not used to get the value at the cell boundary directly, instead, the THINC reconstruction is used to calculate the first order derivative at the cell center as

$$\Phi_i^{[1]}(x_i) = \frac{\gamma\beta u_{max}}{2}\left(1.0 - \tanh\left(\beta\left(0.5 - \tilde{x}_i\right)\right)^2\right)/(x_{i+\frac{1}{2}} - x_{i-\frac{1}{2}}), \tag{5.11}$$

where $u_{max} = \max(\bar{u}_{i-1}, \bar{u}_{i+1}) - \min(\bar{u}_{i-1}, \bar{u}_{i+1})$ and $\gamma = \mathrm{sgn}(\bar{u}_{i+1} - \bar{u}_{i-1})$. The parameter β is used to control the jump thickness. In numerical experiments of this Chapter, we use a constant $\beta = 1.3$ in our computation. The center position $\tilde{x}_i$ of tangent hyperbolic function can be given by

$$\tilde{x}_i = \frac{1}{2}\log(\frac{1-A}{1+A})/\beta, \tag{5.12}$$

where

$$A = (\frac{B}{\cosh(\beta)} - 1)/\tanh\beta, \quad B = \exp(\gamma\beta(\frac{2(\bar{u}_i - \min(\bar{u}_{i-1}, \bar{u}_{i+1}))}{u_{max}} - 1)). \tag{5.13}$$

Then the reconstructed first order derivative is treated as an constraint condition that is used in primary reconstruction of MCV-SC method, i.e. we use three PV values at solution points and $1st$ order derivative at the cell center to build up the primary interpolation as a cubic polynomial, i.e.

$$\begin{cases} \Phi_i^{<2>}(x_{i-\frac{1}{2}}) = u_{i1}; \\ \Phi_i^{<2>}(x_i) = u_{i2}; \\ \Phi_i^{<2>}(x_{i+\frac{1}{2}}) = u_{i3}; \\ \Phi_i^{<2>[1]}(x_i) = \dfrac{\gamma\beta u_{max}}{2}\left(1.0 - \tanh\left(\beta\left(0.5 - \tilde{x}_i\right)\right)^2\right)/(x_{i+\frac{1}{2}} - x_{i-\frac{1}{2}}). \end{cases} \tag{5.14}$$

The first order derivative at the cell boundary can be deduced from the primary reconstructed function $\Phi_i^{<2>}(x)$, which will be used in the selection procedure described in

subsection 5.1.

Remark 3. For Euler equations, the THINC reconstruction for $1st$ order derivative at the cell center is implemented to the characteristic variables, while the selection procedure in the BVD algorithm is also conducted in terms of characteristic variables. In addition, the BVD reconstruction can be conducted on primitive variables, i.e. density, velocity and pressure. We haven't noticed significant difference between above two ways in terms of numerical results.

Remark 4. We use the five stage fourth order SSP Runge-Kutta method [79], the same method used for MCV-WENO4 scheme, for time integration.

5.2 Numerical experiments

In this section, we will give some preliminary results of our presented scheme, BVD-MCV-WENO4 scheme. In our numerical experiments, we use $CFL = 0.2$ throughout our computation.

5.2.1 1D scalar conservation law

Example 5.1. **Accuracy test.** We test the convergence rate of our new scheme in this example. The initial condition is given by a sine wave distribution as

$$u(x, 0) = \sin(\pi x), \quad x \in [-1, 1]. \tag{5.15}$$

We show the numerical results at $t = 2.0$ under growing mesh resolution in Table 5.1. In the same table, we also give the results computed by MCV-WENO4 scheme. In can be observed that the results computed by BVD-MCV-WENO4 reconstruction is exactly same to the ones of MCV-WENO4 scheme, which means BVD-MCV-WENO4 scheme will return to MCV-WENO4 scheme for the smooth solution.

TABLE 5.1: Numerical errors and convergence rate for 1D advection equation, $t = 2.0$.

N	BVD-MCV-WENO4 scheme				MCV-WENO4 scheme			
	L_1 error	Order	L_∞	Order	L_1 error	Order	L_∞	Order
20	4.95e-05		7.72e-05		4.95e-05		7.72e-05	
40	3.12e-06	3.98	4.88e-06	3.98	3.12e-06	3.98	4.88e-06	3.98
80	1.96e-07	3.99	3.07e-07	3.99	1.96e-07	3.99	3.07e-07	3.99
160	1.23e-08	4.00	1.92e-08	4.00	1.23e-08	4.00	1.92e-08	4.00

Example 5.2. **Advection of a square wave.** The initial profile of this test is as follows

$$u(x,0) = \begin{cases} 1, & \text{when}|\text{x}| \leqslant 0.4, \\ 0, & \text{otherwise.} \end{cases} \tag{5.16}$$

The numerical results on a 200-cell mesh after one period are given in Fig.5.1. From the presented numerical results, it can be noticed that the BVD-MCV-WENO4 scheme can get better resolution for discontinuous area near $x = \pm 0.4$. This numerical test can numerically prove that our new BVD-MCV-WENO4 method is able to reduce the numerical dissipation for the jump discontinuity.

Example 5.3. **Jiang and Shu's test.** The initial condition of this test is set to be

$$u(x,0) = \begin{cases} \frac{1}{6}\left(G(x,\beta,z-\delta) + G(x,\beta,z+\delta) + 4G(x,\beta,z)\right), & -0.8 \leqslant x \leqslant -0.6, \\ 1, & -0.4 \leqslant x \leqslant -0.2, \\ 1 - |10(x-0.1)|, & 0.0 \leqslant x \leqslant 0.2, \\ \frac{1}{6}\left(F(x,\alpha,a-\delta) + F(x,\alpha,a+\delta) + 4F(x,\alpha,a)\right), & 0.4 \leqslant x \leqslant 0.6, \\ 0, & \text{otherwise,} \end{cases} \tag{5.17}$$

where the computation domain is $[-1, 1]$. The function F and G is defined by

$$G(x,\beta,z) = \exp\left(-\beta(x-z)^2\right), F(x,\alpha,a) = \sqrt{\max(1-\alpha^2(x-a)^2, 0)}, \tag{5.18}$$

and the coefficients to determine the initial profile are given by

$$a = 0.5,\ z = 0.7,\ \delta = 0.005,\ \alpha = 10.0,\ \beta = \log 2/(36\delta^2). \tag{5.19}$$

We carry out our computation until $t = 2.0$, i.e. one period on a 200-cell mesh. The numerical results computed by both BVD-MCV-WENO4 scheme and MCV-WENO4 scheme are given in Fig.5.2. We can see that by using the BVD reconstruction, the resolution for the jump discontinuity is improved compared with original MCV-WENO4 scheme. Even though the vertex of the cone near $x = 0.5$ is slighted distorted when using BVD-MCV-WENO4 scheme, the deformation is limited to an acceptable level.

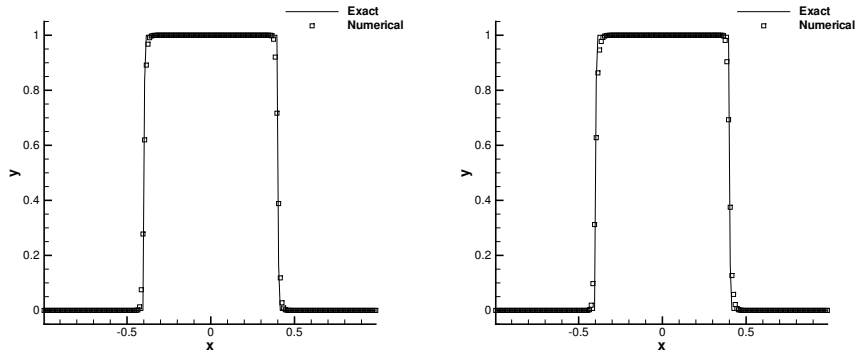

FIGURE 5.1: The numerical results of the advection of a square wave after one period ($t = 2.0$) with 200 grid cells. Here we show the numerical solutions computed by BVD-MCV-WENO4 (left) and MCV-WENO4 (right) schemes.

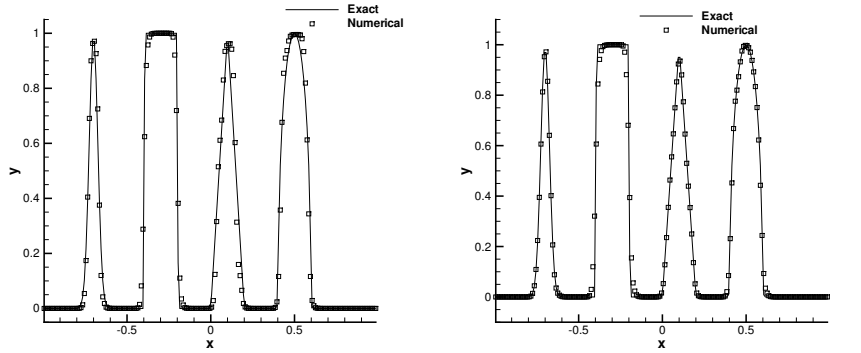

FIGURE 5.2: Numerical results of Jiang and Shu's test at $t = 2.0$ with 200 grid cells computed by BVD-MCV-WENO4 (left) and MCV-WENO4 (right) schemes

5.2.2 1D Euler equations

Example 5.4. **Lax's problem.** This shock-tube test was originally presented in [49]. The initial profile is given by

$$(\rho_0, v_0, p_0) = \begin{cases} (0.445, 0.698, 3.528), & 0 \leqslant x \leqslant 0.5, \\ (0.5, 0, 0.571), & \text{otherwise.} \end{cases} \tag{5.20}$$

The numerical results computed by both BVD-MCV-WENO4 and MCV-WENO4 scheme are given in Fig.5.3 . We can see that the BVD-MCV-WENO4 scheme can reproduce sharp contact discontinuity and shock wave, while still keeping the high accuracy for smooth profile.

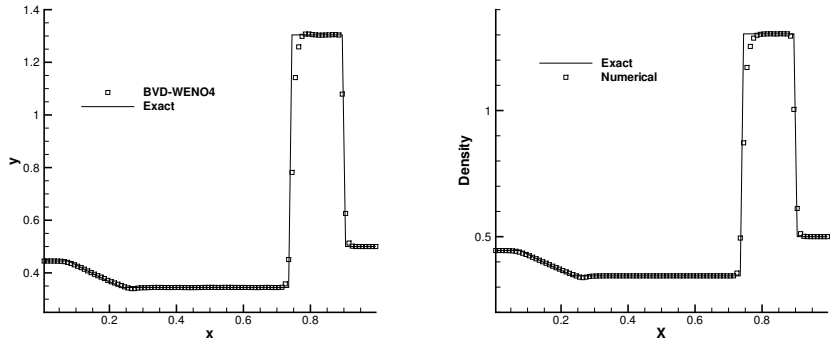

FIGURE 5.3: The numerical solutions of Lax's test at $t = 0.16$ with 100 grid cells. The numerical results shown here are separately computed by BVD-MCV-WENO4 (left) and MCV-WENO4 (right) schemes.

Example 5.5. **A shock-tube test with high Mach number.** This is another shock-tube test. The initial profile is given by

$$(\rho_0, v_0, p_0) = \begin{cases} (1000, 0, 10000), & 0 \leqslant x \leqslant 0.5, \\ (1, 0, 1), & \text{otherwise.} \end{cases} \tag{5.21}$$

The computation is carried out up to $t = 0.05$. We use a mesh of 400 cells to capture the accurate position of shock wave. The numerical results of both BVD-MCV-WENO4 and MCV-WENO4 scheme are shown in Fig.5.4. It is obvious that the BVD reconstruction can significantly improve the solution quality near the contact discontinuity. The

results validate the effectiveness of BVD-MCV-WENO4 scheme in the reduction of numerical dissipation.

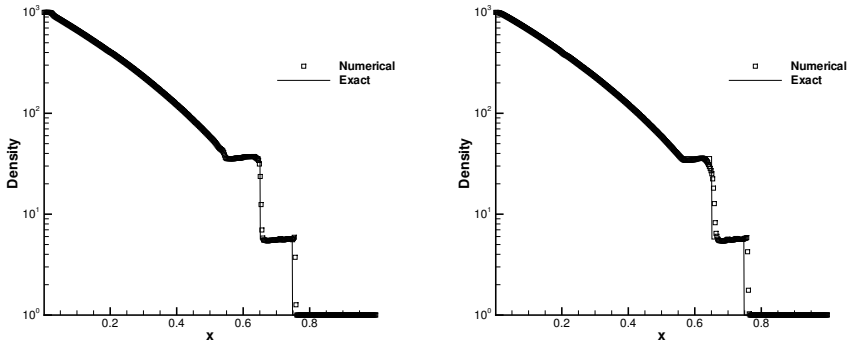

FIGURE 5.4: The numerical results of the high Mach number test on a domain of 400 grid cells. Here we show the numerical solutions computed by BVD-MCV-WENO4 (left) and MCV-WENO4 (right) schemes.

Example 5.6. **Two interacting blast waves.** This test [94] describes the multiple interaction between strong shock wave and rarefaction wave. The initial condition for this test can be described by the following equations

$$(\rho_0, v_0, p_0) = \begin{cases} (1, 0, 1000), & \text{if } 0 \leqslant \mathrm{x} \leqslant 0.1, \\ (1, 0, 0.01), & \text{if } 0.1 < \mathrm{x} < 0.9, \\ (1, 0, 100), & \text{otherwise.} \end{cases} \tag{5.22}$$

We execute the computation up to $t = 0.038$ on a mesh of 400 cells. The numerical results are plotted in Fig.5.5. It can be noticed that the contact discontinuity around $x = 0.6$ can be resolved within 5 cells, which is better than the MCV-WENO4 scheme that needs about ten cells. This test provides sufficient evidences that the BVD algorithm presented here can efficiently reduce the numerical dissipation near the discontinuous solutions.

5.3 Summary

In this Chapter, we develop a new version of BVD algorithm that can use HLR methods as building-block schemes. As the HLR method includes more than one DOF inside

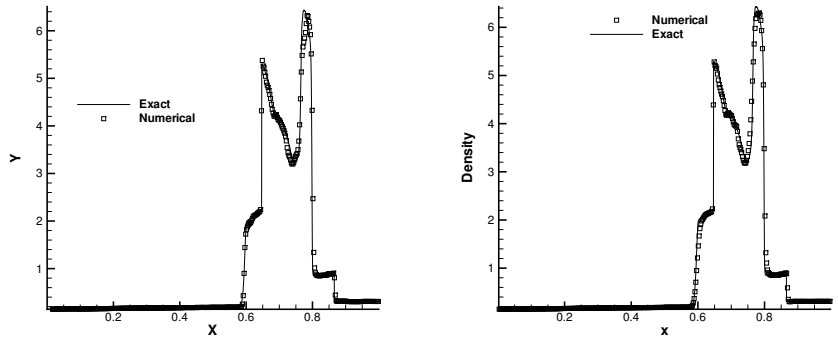

FIGURE 5.5: The numerical results of the two interacting blast wave a 400-cell mesh. Here we show the numerical solutions computed by BVD-MCV-WENO4 scheme (left) and MCV-WENO4 scheme (right).

each cell, we extend the definition of BV to the difference of derivative values at the cell interface, and BVD reconstruction minimizes not only the BV of the PV but also the derivative values, which is compatible with MCV-type method that always keeps the C^0 continuity at the cell boundary while assumeing jumps of high order derivatives.

In order to provide a building-block scheme for BVD reconstruction that can better represent the discontinuity as well as make full use of the local DOFs, we develop a new THINC-implemented reconstruction in this Chapter, which uses THINC reconstruction to obtain the $1st$ order derivative at the cell center, and the solution function is reconstructed by the constraint conditions of MCV-SC scheme introduced in Chapter 3. Then, our new version of BVD method equips MCV-WENO4 scheme developed in Chapter 3 as one building-block scheme and THINC-implemented MCV-SC scheme as the other one. The resulting scheme, i.e. BVD-MCV-WENO4 scheme, is treat as a trial to the full implementation of BVD reconstruction in HLR method.

The numerical results presented in this chapter demonstrate that the new BVD algorithm is capable of minimizing the numerical dissipation near the discontinuous solutions, especially for jump discontinuities, at the same time, the smooth solutions can be resolved with high accuracy.

Chapter 6

Conclusions and future work

6.1 Full picture of this thesis

In the numerical simulation of Euler equations, the numerical dissipations and numerical oscillations are two critical problems that highly limit the development of high resolution scheme. To reduce the numerical dissipation for Godonuv-type method, we present a new direction to devise the high resolution scheme, which is called BVD method. On the other hand, in order to suppress the numerical oscillations around the jump discontinuity caused by Gibbs phenomenon for high resolution method with local reconstructions, we design a new WENO-type limiter that creatively uses PV instead of the VIA in the WENO reconstruction, resulting a scheme of better geometrical compactness and computational efficiency. The new WENO limiter is applied to MCV3 scheme of MMC-FR method, and the resulting scheme is named MCV-WENO4 scheme in this thesis. Also, the new WENO limiter is successfully applied to the semi-Lagrangian type method, CIP-CSL3 scheme, which gives the CIP-CSL-WENO4 scheme proposed in this thesis. Finally, we extend BVD algorithm to HLR method by using MCV-WENO4 scheme and THINC reconstruction as building-block schemes, which leads to the BVD-MCV-WENO4 scheme that is treat as the preliminary research to apply the BVD principle on a HLR scheme.

The BVD reconstruction is developed based on the observation that the numerical dissipation of numerical scheme is controlled by BV (i.e., the absolute difference of reconstructed quantities) at the cell boundary, and the increase of the order of reconstruction polynomial can not guarantee the reduction of BV when the solutions contain jump discontinuities. Inspired by the this observation, we put aside the idea of using high order polynomial reconstruction throughout our computation but introduce a selection procedure that can switch to the reconstruction method with better monotonicity based on the principle of the minimization of the BV. In this study, we use WENO-Z scheme as one building-block scheme of high resolution polynomial reconstruction while THINC reconstruction as another building-block scheme that can better represent the discontinuous solutions. The numerical results presented in this thesis strongly validate the numerical dissipation minimization property of BVD algorithm. Some of the numerical results are among the best in the literature.

The MCV-WENO4 scheme presented in this thesis focuses on eliminating the numerical oscillations for the high order numerical method with local reconstructions. The traditional WENO limiter for DG follows the original FVM-type WENO method by using the VIA in WENO reconstruction, which ignores the locally defined DOFs of HLR method. As a result, we present a new WENO limiter that can effectively use the local information inside the cells, which can maintain the geometrical adaptability of HLR method. The new WENO limiter is developed based on MCV3 method, and the polynomial interpolation of WENO limiter uses only three solution points at the target cell and two center points from neighboring cells. We use Shen's WENO reconstruction in our new WENO limiter. The new WENO limiter also distinguishes itself from the traditional WENO limiter by discarding the TVB criterion that was used to control the excessive numerical dissipation. In other words, the WENO reconstruction of MCV-WENO4 scheme has much less numerical dissipation to the smooth solutions. The numerical results of MCV-WENO4 scheme show our new limiter can efficiently diminish the numerical oscillations, while keeping the high order accuracy for smooth solution.

We also develop a new oscillation-free semi-Lagrangian type method, CIP-CSL-WENO4 scheme, where numerical oscillations are suppressed by our original nodal value based

WENO limiter . Because the space discretization of CIP-CSL3 scheme includes both PV and VIA, we firstly map the cell VIA into the PV at the cell center, then the WENO reconstruction follows the idea of the WENO limiter in MCV-WENO4 scheme developed in Chapter 3, i.e. using three solution points of the target cell and the cell center points from the neighboring cells to construct the WENO reconstruction stencil. In order to highlight the merit of semi-Lagrangian method, we compare the numerical dissipation and numerical dispersion errors between MCV-WENO4 scheme of Eulerian and CIP-CSL-WENO4 scheme of semi-Lagrangian. The numerical results of CIP-CSL-WENO4 scheme indicate that our scheme is capable of resolving the sharp jump discontinuity while essentially eliminateing numerical oscillations.

Finally, we present a new type of BVD algorithm specifically for HLR method. The new BVD reconstruction realizes not only the minimization of BV for PV but also for high order derivatives at the cell interface. We also present a new instance, the so-called BVD-MCV-WENO4 scheme, for the new version of BVD reconstruction that uses MCV-WENO4 scheme as one building-block scheme. For the other building-block scheme of better monotonicity, we develop a new reconstruction that is based on the primary interpolation procedure of MCV-SC scheme while the first order derivative at the cell center which is needed as a constraint condition is reconstructed by THINC reconstruction. The numerical results of both 1D scalar conservation law and Euler equations is consistent with our expectation of BVD algorithm in the minimization of the numerical dissipation.

6.2 Major contributions of current study

The novelty of our scheme can be categorized into the following two parts.

1. We totally innovate the traditional Godunov-type method that always assumes a discontinuity at the cell interface while pursuing the high order reconstruction inside cell. This can work well for smooth solution because of the Weierstrass Theorem, which indicates that high order polynomial reconstruction can simulate a continuous equation with high accuracy. However, for the discontinuous

solutions where Weierstrass Theorem is not applicable, the circumstances will be totally different. In fact, from the numerical experiments in section 2.1 of Chapter 2, we notice that the increase of the polynomial order can not reduce BV, i.e. reconstructed difference at the cell boundary for discontinous solutions. This observation has not been paid enough attention in the literature. However, we notice this phenomenon, and in order to solve this problem, we develop the BVD algorithm which can be seen as a generalized principle that totally reforms the traditional Godunov-type method by introducing more than one reconstruction method for each cell, and a selection procedure is introduced to switch between different methods based on the criterion of the minimization of the BV at the cell interface.

To our opinion, the BVD reconstruction has overturned the traditional way to build up the numerical schemes. Excellent numerical results validate its possibility in the development of new scheme with superior property.

2. We provide a trial in the development of WENO limiter under HLR formulation. The new WENO limiter can make full use the sub-grid information by introducing the solution points within the cell in the WENO reconstruction, which is superior to the traditional WENO limiter for DG that uses only one VIA for each cell. Compared with traditional WENO limiter, our original WENO limiter is of better geometrical adaptability and algorithmical simplicity. We also give up using the ad hoc TVD criterion, or so-called the "trouble cell" indicator in our WENO limiter and still obtain ideal solutions, which overturns the traditional procedure in performing the WENO limiting procedure.

   With the booming development of HLR method, especially nodal value based HLR method such as FR method [37–39], MMC-FR method [102] or Nodal DG method [33], the WENO limiter that can make full use of sub-grid information is necessary for applying the HLR method in the computation of Euler equations. We believe that our work leads a new direction in constructing the WENO limiter that is much more suitable for HLR method.

6.3 Future work

We will introduce our future work from the following two aspects.

1. We hope to extend our BVD principle to other HLR methods, such as DG method and FR method, to make it a true generalized platform that is available for high order methods of not only FVM-type but also HLR formulation. However, For most schemes of HLR-type, there are more than one DOFs inside each cell. The only minimization of the BV may not be able to reduce the numerical dissipation. A possible way to apply BVD reconstruction for HLR method is to perform the BVD reconstruction locally inside each cell. Following the work of Dumbser in [21], each control volume can be divided into several subcell piece-wise constants. Then the BVD reconstruction can be imposed for each sub-cell just as being done for FVM.

   Also, it is important to prove the effectiveness of BVD algorithm in the reduction of the numerical dissipation mathematically, which can provide some theoretical fundamentals for our scheme.

   We also hope to apply the BVD reconstruction in solving the Navier-Stokes equations to resolve the incompressible flow. In the computation of the Navier-Stokes equations, for high-Reynolds-number flow with small real viscosity, the presence of excessive numerical viscosity will cast doubt on accuracy of the numerical solution. By using the BVD reconstruction, the numerical viscosity can be minimized, thus the physical viscosity will dominate the viscous effect, which could give the much more accurate results when applied with turbulence model.

2. To demonstrate the geometrical flexibility of our scheme, we hope to extend MCV-WENO4 scheme to unstructured meshes. As our 4th order WENO limiter only uses the PVs from the target cell and its nearest neighboring cells in WENO reconstruction, for unstructured meshes, the stencil can be minimized, which can yield a scheme with high geometrical adaptability. Also, we believe that the principle of using PV in the WENO reconstruction is possible to be applied to other nodal value based HLR method such as FR and nodal DG method. However, the

location of the solution points for other HLR methods is not the same as MCV-type method, which means that our WENO limiter needs necessary modification when applied to other HLR methods.

Appendix A

Eigenstructures of 1D and 2D Euler equations

A.1 1D Euler equations

As mentioned in Chapter 3, the 1D Euler equations is defined by

$$\mathbf{U}_t + \mathbf{F}(\mathbf{U})_x = 0, \tag{A.1}$$

where

$$\mathbf{U} = \begin{pmatrix} \rho \\ \rho v \\ E \end{pmatrix}, \quad \mathbf{F}(\mathbf{U}) = \begin{pmatrix} \rho v \\ \rho v^2 + p \\ v(E+p) \end{pmatrix}. \tag{A.2}$$

Here ρ is the density,v is the velocity, p is the pressure and E is the total energy. For the ideal gas, the total energy is given by

$$E = \frac{p}{\gamma - 1} + \frac{1}{2}\rho v^2, \tag{A.3}$$

where γ is heat capacity ratio. The equations A.1 can also be written in quasi-linear form

$$\mathbf{U}_t + \mathbf{A}(\mathbf{U})\mathbf{U}_x = 0, \tag{A.4}$$

where $\mathbf{A}(\mathbf{U})$ is the Jacobian Matrix defined by

$$\mathbf{A}(\mathbf{U}) = \begin{bmatrix} 0 & 1 & 0 \\ \frac{1}{2}(\gamma-3)v^2 & (3-\gamma)v & \gamma-1 \\ \frac{1}{2}(\gamma-1)v^3 - vH & H-(\gamma-1)v^2 & \gamma v \end{bmatrix}, \tag{A.5}$$

Here H is the total specific enthalpy defined by

$$H = \frac{(E+p)}{\rho}. \tag{A.6}$$

The eigenvalues of Jacobian matrix $\mathbf{A}(\mathbf{U})$ are given by,

$$\lambda_1 = v - a,\ \lambda_2 = v,\ \lambda_3 = v + a, \tag{A.7}$$

where a is the sound speed, $a = \sqrt{\left(\frac{\partial p}{\partial \rho}\right)_s}$. By using the the EOS of ideal gases, the sound speed a can be given by

$$a = \sqrt{\frac{\gamma p}{\rho}}. \tag{A.8}$$

The corresponding right eigenvectors of Jacobian matrix $\mathbf{A}(\mathbf{U})$ are

$$\mathbf{R} = \begin{bmatrix} 1 & 1 & 1 \\ v-a & v & v+a \\ H-va & V & H+va \end{bmatrix}, \tag{A.9}$$

where each eigenvector is the column of the matrix $\mathbf{R}$. The left eigenvectors of Jacobian matrix $\mathbf{A}(\mathbf{U})$ are

$$\mathbf{L} = \begin{bmatrix} \frac{1}{2}\left(\frac{V(\gamma-1)}{a^2} + \frac{v}{a}\right) & -\frac{1}{2}\left(\frac{v(\gamma-1)}{a^2} + \frac{1}{a}\right) & \frac{(\gamma-1)}{2a^2} \\ 1 - \frac{V(\gamma-1)}{a^2} & \frac{v(\gamma-1)}{a^2} & -\frac{\gamma-1}{a^2} \\ \frac{1}{2}\left(\frac{V(\gamma-1)}{a^2} - \frac{v}{a}\right) & -\frac{1}{2}\left(\frac{v(\gamma-1)}{a^2} - \frac{1}{a}\right) & \frac{(\gamma-1)}{2a^2} \end{bmatrix}, \tag{A.10}$$

where each row of matrix $\mathbf{L}$ corresponds to each left eigenvector. Here $V = \frac{1}{2}v^2$.

A.2 2D Euler equations

The 2D Euler systems is defined by

$$\mathbf{U}_t + \mathbf{F}(\mathbf{U})_x + \mathbf{G}(\mathbf{U})_y = 0, \tag{A.11}$$

where,

$$\mathbf{U} = \begin{pmatrix} \rho \\ \rho u \\ \rho v \\ E \end{pmatrix}, \quad \mathbf{F}(\mathbf{U}) == \begin{pmatrix} \rho u \\ \rho u^2 + p \\ \rho uv \\ u(E+p) \end{pmatrix}, \quad \mathbf{G}(\mathbf{U}) = \begin{pmatrix} \rho v \\ \rho uv \\ \rho v^2 + p \\ v(E+p) \end{pmatrix}, \tag{A.12}$$

where ρ is the density, p the pressure, (u, v) the velocity component in x and y direction and E the total energy. The equations (A.11) can also be written via a quasi-linear form as

$$\mathbf{U}_t + \mathbf{A}(\mathbf{U})\mathbf{U}_x + \mathbf{B}(\mathbf{U})\mathbf{U}_y = 0. \tag{A.13}$$

The Jacobian matrix $\mathbf{A}(\mathbf{U})$ corresponding to flux $\mathbf{F}(\mathbf{U})$ is defined by

$$\mathbf{A}(\mathbf{U}) = \begin{pmatrix} 0 & 1 & 0 & 0 \\ -u^2 + (\gamma-1)\mathbf{V} & -(\gamma-3)u & -(\gamma-1)v & (\gamma-1) \\ -uv & v & u & 0 \\ u\left(\mathbf{V}(\gamma-1) - H\right) & H - u^2(\gamma-1) & -(\gamma-1)uv & \gamma u \end{pmatrix}, \tag{A.14}$$

where

$$\begin{aligned} \mathbf{V} &= \frac{1}{2}(u^2 + v^2), \\ H &= \frac{P+E}{\rho}. \end{aligned} \tag{A.15}$$

The eigenvalues of Jacobian matrix $\mathbf{A}(\mathbf{U})$ are

$$\lambda_1 = u - a,\ \lambda_2 = u,\ \lambda_3 = u,\ \lambda_4 = u + a, \tag{A.16}$$

where a is the sound speed. For ideal gases EOS, the sound speed a and total enthalpy H can be calculated by

$$\begin{aligned} a &= \sqrt{\frac{\gamma p}{\rho}}, \\ H &= \frac{a^2}{\gamma - 1} + \mathbf{V}. \end{aligned} \tag{A.17}$$

The corresponding right eigenvectors are given by

$$\mathbf{R}^x = \begin{pmatrix} 1 & 0 & 1 & 1 \\ u-a & 0 & u & u+a \\ v & 1 & v & v \\ H - ua & v & \mathbf{V} & H + ua \end{pmatrix}, \tag{A.18}$$

where each column of the matrix $\mathbf{R}^x$ is corresponding to each right eigenvector. And the left eigenvectors are given by

$$\mathbf{L}^x = \begin{pmatrix} \frac{1}{2}(\gamma-1)\frac{\mathbf{V}}{a^2} + \frac{u}{2a} & -\frac{1}{2}\left(\frac{u(\gamma-1)}{a^2} + \frac{1}{a}\right) & -\frac{v(\gamma-1)}{2a^2} & \frac{(\gamma-1)}{2a^2} \\ -v & 0 & 1 & 0 \\ 1 - (\gamma-1)\frac{\mathbf{V}}{a^2} & (\gamma-1)\frac{u}{a^2} & (\gamma-1)\frac{v}{a^2} & -\frac{(\gamma-1)}{a^2} \\ \frac{1}{2}(\gamma-1)\frac{\mathbf{V}}{a^2} - \frac{u}{2a} & -\frac{1}{2}\left(\frac{u(\gamma-1)}{a^2} - \frac{1}{a}\right) & -\frac{v(\gamma-1)}{2a^2} & \frac{(\gamma-1)}{2a^2} \end{pmatrix}, \tag{A.19}$$

where each row of the matrix $\mathbf{L}^x$ is corresponding to each left eigenvector.

The Jacobian matrix of $\mathbf{B}(\mathbf{U})$ corresponding to flux $\mathbf{G}(\mathbf{U})$ is defined by

$$\mathbf{B}(\mathbf{U}) = \begin{pmatrix} 0 & 0 & 1 & 0 \\ -uv & v & u & 0 \\ -v^2 + (\gamma-1)\mathbf{V} & -(\gamma-1)u & -(\gamma-3)v & (\gamma-1) \\ v(\mathbf{V}(\gamma-1) - H) & -(\gamma-1)uv & H - v^2(\gamma-1) & \gamma v \end{pmatrix}. \quad \text{(A.20)}$$

The eigenvalues of Jacobian matrix $\mathbf{B}(\mathbf{U})$ are

$$\lambda_1 = v - a,\ \lambda_2 = v,\ \lambda_3 = v,\ \lambda_4 = v + a, \quad \text{(A.21)}$$

The corresponding right eigenvectors are given by

$$\mathbf{R}^y = \begin{pmatrix} 1 & 0 & 1 & 1 \\ u & 1 & u & u \\ v - a & 0 & v & v + a \\ H - va & u & \mathbf{V} & H + va \end{pmatrix}. \quad \text{(A.22)}$$

Here the column of the matrix $\mathbf{R}^y$ is corresponding to each eigenvector of $\mathbf{B}(\mathbf{U})$. The left eigenvectors of $\mathbf{B}(\mathbf{U})$ are given by

$$\mathbf{L}^y = \begin{pmatrix} \frac{1}{2}(\gamma-1)\frac{\mathbf{V}}{a^2} + \frac{v}{2a} & -\frac{u(\gamma-1)}{2a^2} & -\frac{1}{2}\left(\frac{v(\gamma-1)}{a^2} + \frac{1}{a}\right) & \frac{(\gamma-1)}{2a^2} \\ -u & 1 & 0 & 0 \\ 1 - (\gamma-1)\frac{\mathbf{V}}{a^2} & (\gamma-1)\frac{u}{a^2} & (\gamma-1)\frac{v}{a^2} & -\frac{(\gamma-1)}{a^2} \\ \frac{1}{2}(\gamma-1)\frac{\mathbf{V}}{a^2} - \frac{v}{2a} & -\frac{u(\gamma-1)}{2a^2} & -\frac{1}{2}\left(\frac{v(\gamma-1)}{a^2} - \frac{1}{a}\right) & \frac{(\gamma-1)}{2a^2} \end{pmatrix}, \quad \text{(A.23)}$$

where each row of the matrix $\mathbf{L}^y$ is corresponding to each left eigenvector.

Appendix B

Definition of Roe average for 1D and 2D Euler equations

B.1 1D Euler equations

For the 1D Euler equations, As mentioned in Chapter 3, the 1D Euler equations are defined by

$$\mathbf{U}_t + \mathbf{F}(\mathbf{U})_x = 0, \tag{B.1}$$

where

$$\mathbf{U} = \begin{pmatrix} \rho \\ \rho v \\ E \end{pmatrix}, \quad \mathbf{F}(\mathbf{U}) = \begin{pmatrix} \rho v \\ \rho v^2 + p \\ v(E+p) \end{pmatrix}. \tag{B.2}$$

Here ρ is the density, v is the velocity, p is the pressure and E is the total energy. We use the ideal gases EOS, and the total energy is defined by $E = \dfrac{p}{\gamma - 1} + \dfrac{1}{2}\rho v^2$. Initially we have a jump of conservative variable

$$\Delta \mathbf{U} = \mathbf{U}^R - \mathbf{U}^L. \tag{B.3}$$

The Roe average[84] for velocity v, total enthalpy $H = \dfrac{(E+p)}{\rho}$ and sound speed a is given by

$$\begin{aligned}
\tilde{v} &= \frac{\sqrt{\rho_L}v_L + \sqrt{\rho_R}v_R}{\sqrt{\rho_L} + \sqrt{\rho_R}} \\
\tilde{H} &= \frac{\sqrt{\rho_L}H_L + \sqrt{\rho_R}H_R}{\sqrt{\rho_L} + \sqrt{\rho_R}} \\
\tilde{a} &= \left((\gamma-1)(\tilde{H} - \frac{1}{2}\tilde{v}^2)\right)^{\frac{1}{2}},
\end{aligned} \tag{B.4}$$

where the $\tilde{v}$, $\tilde{H}$ and $\tilde{a}$ is the Roe averaged value of v, H and a. v_L, H_L and ρ_L is given from the left side conservative variables $\mathbf{U}^L$ and v_R, H_R and ρ_R is given from right side conservative variables $\mathbf{U}^R$. The Roe averaged Jacobian matrix $\mathbf{A}(\mathbf{U})$ of (A.5) is given by

$$\overline{\mathbf{A}}(\mathbf{U}) = \begin{bmatrix} 0 & 1 & 0 \\ \frac{1}{2}(\gamma-3)\tilde{v}^2 & (3-\gamma)\tilde{v} & \gamma-1 \\ \frac{1}{2}(\gamma-1)\tilde{v}^3 - \tilde{v}\tilde{H} & \tilde{H} - (\gamma-1)\tilde{v}^2 & \gamma\tilde{v} \end{bmatrix}, \tag{B.5}$$

with the eigenvalues are defined by

$$\lambda_1 = \tilde{v} - \tilde{a},\ \lambda_2 = \tilde{v},\ \lambda_3 = \tilde{v} + \tilde{a}, \tag{B.6}$$

The Roe averaged right eigenvectors are defined by

$$\overline{\mathbf{R}} = \begin{bmatrix} 1 & 1 & 1 \\ \tilde{v} - \tilde{a} & \tilde{v} & \tilde{v} + \tilde{a} \\ \tilde{H} - \tilde{v}\tilde{a} & \frac{1}{2}\tilde{v}^2 & \tilde{H} + \tilde{v}\tilde{a} \end{bmatrix}, \tag{B.7}$$

and the left eigenvectors are given by

$$\overline{\mathbf{L}} = \begin{bmatrix} \frac{1}{2}\left(\frac{\tilde{V}(\gamma-1)}{\tilde{a}^2} + \frac{\tilde{v}}{\tilde{a}}\right) & -\frac{1}{2}\left(\frac{\tilde{v}(\gamma-1)}{\tilde{a}^2} + \frac{1}{\tilde{a}}\right) & \frac{(\gamma-1)}{2\tilde{a}^2} \\ 1 - \frac{\tilde{V}(\gamma-1)}{\tilde{a}^2} & \frac{\tilde{v}(\gamma-1)}{\tilde{a}^2} & -\frac{\gamma-1}{\tilde{a}^2} \\ \frac{1}{2}\left(\frac{\tilde{V}(\gamma-1)}{\tilde{a}^2} - \frac{\tilde{v}}{\tilde{a}}\right) & -\frac{1}{2}\left(\frac{\tilde{v}(\gamma-1)}{\tilde{a}^2} - \frac{1}{\tilde{a}}\right) & \frac{(\gamma-1)}{2\tilde{a}^2} \end{bmatrix}, \tag{B.8}$$

where $\tilde{V} = \frac{1}{2}\tilde{v}^2$. We can see that with only the Roe averaged variable v, H and a, the whole Roe averaged eigenstructures of 1D Euler equations can be recovered.

B.2 2D Euler equations

For the 2D Euler equations

$$\mathbf{U}_t + \mathbf{F}(\mathbf{U})_x + \mathbf{G}(\mathbf{U})_y = 0, \tag{B.9}$$

where

$$\mathbf{U} = \begin{pmatrix} \rho \\ \rho u \\ \rho v \\ E \end{pmatrix}, \quad \mathbf{F}(\mathbf{U}) == \begin{pmatrix} \rho u \\ \rho u^2 + p \\ \rho uv \\ u(E+p) \end{pmatrix}, \quad \mathbf{G}(\mathbf{U}) = \begin{pmatrix} \rho v \\ \rho uv \\ \rho v^2 + p \\ v(E+p) \end{pmatrix}, \tag{B.10}$$

where ρ is the density, p the pressure, (u, v) the velocity component in x and y direction and E the total energy. The Roe averaged velocity (u, v), total enthalpy H and sound speed a is given by,

$$\begin{aligned} \tilde{u} &= \frac{\sqrt{\rho_L}u_L + \sqrt{\rho_R}u_R}{\sqrt{\rho_L} + \sqrt{\rho_R}} \\ \tilde{v} &= \frac{\sqrt{\rho_L}v_L + \sqrt{\rho_R}v_R}{\sqrt{\rho_L} + \sqrt{\rho_R}} \\ \tilde{H} &= \frac{\sqrt{\rho_L}H_L + \sqrt{\rho_R}H_R}{\sqrt{\rho_L} + \sqrt{\rho_R}} \\ \tilde{a} &= \left((\gamma - 1)(\tilde{H} - \frac{1}{2}\tilde{\mathbf{V}}^2)\right)^{\frac{1}{2}}, \end{aligned} \tag{B.11}$$

for the initial jump

$$\Delta\mathbf{U} = \mathbf{U}^R - \mathbf{U}^L. \tag{B.12}$$

where $\tilde{\mathbf{V}} = \frac{1}{2}(\tilde{v}^2 + \tilde{u}^2)$. Then we can get the Roe averaged Jacobian matrix and its eigenvalues and eigenvectors by replacing the variable u, v, H and a by the Roe averaged value $\tilde{u}$, $\tilde{v}$, $\tilde{H}$ and $\tilde{a}$. For example, the Roe average of Jacobian matrix $\mathbf{A}(\mathbf{U})$ in

(A.14) can be deduced by

$$\overline{\mathbf{A}}(\mathbf{U}) = \begin{pmatrix} 0 & 1 & 0 & 0 \\ -\tilde{u}^2 + (\gamma-1)\mathbf{V} & -(\gamma-3)\tilde{u} & -(\gamma-1)\tilde{v} & (\gamma-1) \\ -\tilde{u}\tilde{v} & \tilde{v} & \tilde{u} & 0 \\ \tilde{u}\left(\tilde{\mathbf{V}}(\gamma-1) - \tilde{H}\right) & \tilde{H} - \tilde{u}^2(\gamma-1) & -(\gamma-1)\tilde{u}\tilde{v} & \gamma\tilde{u} \end{pmatrix}. \tag{B.13}$$

The eigenvalues of $\overline{\mathbf{A}}(\mathbf{U})$ are given by

$$\lambda_1 = \tilde{u} - \tilde{a},\ \lambda_2 = \tilde{u},\ \lambda_3 = \tilde{u},\ \lambda_4 = \tilde{u} + \tilde{a}, \tag{B.14}$$

and the right eigenvectors are given by

$$\overline{\mathbf{R}^x} = \begin{pmatrix} 1 & 0 & 1 & 1 \\ \tilde{u} - \tilde{a} & 0 & \tilde{u} & \tilde{u} + \tilde{a} \\ \tilde{v} & 1 & \tilde{v} & \tilde{v} \\ H - \tilde{u}\tilde{a} & \tilde{v} & \tilde{\mathbf{V}} & H + \tilde{a}\tilde{u} \end{pmatrix}, \tag{B.15}$$

while the left eigenvectors are defined by

$$\overline{\mathbf{L}}^x = \begin{pmatrix} \frac{1}{2}(\gamma-1)\frac{\tilde{\mathbf{V}}}{\tilde{a}^2} + 1\frac{\tilde{u}}{2\tilde{a}} & -\frac{1}{2}\left(\frac{\tilde{u}(\gamma-1)}{\tilde{a}^2} + \frac{1}{\tilde{a}}\right) & -\frac{\tilde{v}(\gamma-1)}{2\tilde{a}^2} & \frac{(\gamma-1)}{2\tilde{a}^2} \\ -\tilde{v} & 0 & 1 & 0 \\ 1 - (\gamma-1)\frac{\tilde{\mathbf{V}}}{\tilde{a}^2} & (\gamma-1)\frac{\tilde{u}}{\tilde{a}^2} & (\gamma-1)\frac{\tilde{v}}{\tilde{a}^2} & -\frac{(\gamma-1)}{\tilde{a}^2} \\ \frac{1}{2}(\gamma-1)\frac{\tilde{\mathbf{V}}}{\tilde{a}^2} - \frac{\tilde{u}}{2\tilde{a}} & -\frac{1}{2}\left(\frac{\tilde{u}(\gamma-1)}{\tilde{a}^2} - \frac{1}{\tilde{a}}\right) & -\frac{\tilde{v}(\gamma-1)}{2\tilde{a}^2} & \frac{(\gamma-1)}{2\tilde{a}^2} \end{pmatrix}. \tag{B.16}$$

Similarly, we can get the Roe averaged Jacobian matrix $\mathbf{A}(\mathbf{U})$ in (A.20) and its eigenvectors and eigenvalues in a similar way.

Bibliography

[1] Y. Abe, Z.Y. Sun, and F. Xiao. A note on implementation of boundary variation diminishing algorithm to high-order local polynomial-based schemes. *arXiv preprint*, arXiv:1605.08332.

[2] J.D. Anderson and J. Wendt. *Computational fluid dynamics*. McGraw-Hill, 1995.

[3] T. Aoki. Interpolated differential operator (IDO) scheme for solving partial differential equations. *Computer physics communications*, 102(1):132–146, 1997.

[4] A. Aprovitola and F.M. Denaro. On the application of congruent upwind discretizations for large eddy simulations. *Journal of Computational Physics*, 194 (1):329–343, 2004.

[5] G.M. Arshed and K.A. Hoffmann. Minimizing errors from linear and nonlinear weights of WENO scheme for broadband applications with shock waves. *Journal of Computational Physics*, 246:58–77, 2013.

[6] R. Borges, M. Carmona, B. Costa, and W.S. Don. An improved weighted essentially non-oscillatory scheme for hyperbolic conservation laws. *Journal of Computational Physics*, 227(6):3191–3211, 2008.

[7] J.P. Boris and D.L. Book. Flux-corrected transport. I. SHASTA, a fluid transport algorithm that works. *Journal of computational physics*, 11(1):38–69, 1973.

[8] S.E. Buckley, M.C. Leverett, and Members A.I.M.E. Mechanism of fluid displacement in sands. *Transactions of the AIME*, 146(01):107–116, 1942.

[9] D.A. Cassidy, J.R. Edwards, and M. Tian. An investigation of interface-sharpening schemes for multi-phase mixture flows. *Journal of Computational Physics*, 228(16):5628–5649, 2009.

[10] C.G. Chen and F. Xiao. Shallow water model on cubed-sphere by multi-moment finite volume method. *Journal of Computational Physics*, 227(10):5019–5044, 2008.

[11] C.G. Chen, X.L. Li, X.S. Shen, and F. Xiao. Global shallow water models based on multi-moment constrained finite volume method and three quasi-uniform spherical grids. *Journal of Computational Physics*, 271:191–223, 2014.

[12] B. Cockburn and C.W. Shu. TVB Runge-Kutta local projection discontinuous Galerkin finite element method for conservation laws. II. General framework. *Mathematics of Computation*, 52(186):411–435, 1989.

[13] B. Cockburn and C.W. Shu. The Runge-Kutta discontinuous Galerkin method for conservation laws V: multidimensional systems. *Journal of Computational Physics*, 141(2):199–224, 1998.

[14] B. Cockburn and C.W. Shu. The Runge-Kutta discontinuous Galerkin method for conservation laws V: multidimensional systems. *Journal of Computational Physics*, 141(2):199–224, 1998.

[15] B. Cockburn and C.W. Shu. Runge-Kutta discontinuous Galerkin methods for convection-dominated problems. *Journal of scientific computing*, 16(3):173–261, 2001.

[16] B. Cockburn, S.Y. Lin, and C.W. Shu. TVB Runge-Kutta local projection discontinuous Galerkin finite element method for conservation laws III: one-dimensional systems. *Journal of Computational Physics*, 84(1):90–113, 1989.

[17] B. Cockburn, S.H. Hou, and C.W. Shu. The Runge-Kutta local projection discontinuous Galerkin finite element method for conservation laws. IV. The multidimensional case. *Mathematics of Computation*, 54(190):545–581, 1990.

[18] P. Colella and P.R. Woodward. The piecewise parabolic method (PPM) for gas-dynamical simulations. *Journal of computational physics*, 54(1):174–201, 1984.

[19] X.G. Deng and H.X. Zhang. Developing high-order weighted compact nonlinear schemes. *Journal of Computational Physics*, 165(1):22–44, 2000.

[20] J. Du, C.W. Shu, and M.P. Zhang. A simple weighted essentially non-oscillatory limiter for the correction procedure via reconstruction (CPR) framework. *Applied Numerical Mathematics*, 95:173–198, 2015.

[21] M. Dumbser, O. Zanotti, R. Loubère, and S. Diot. A posteriori subcell limiting of the discontinuous Galerkin finite element method for hyperbolic conservation laws. *Journal of Computational Physics*, 278:47–75, 2014.

[22] J.A. Ekaterinaris. High-order accurate, low numerical diffusion methods for aerodynamics. *Progress in Aerospace Sciences*, 41(3):192–300, 2005.

[23] L. Fu, X.Y. Hu, and N.A. Adams. A family of high-order targeted ENO schemes for compressible-fluid simulations. *Journal of Computational Physics*, 305:333–359, 2016.

[24] F.X. Giraldo. The Lagrange–Galerkin spectral element method on unstructured quadrilateral grids. *Journal of Computational Physics*, 147(1):114–146, 1998.

[25] S.K. Godunov. A difference method for numerical calculation of discontinuous solutions of the equations of hydrodynamics. *Matematicheskii Sbornik*, 89(3): 271–306, 1959.

[26] D. Gottlieb and C.W. Shu. On the Gibbs phenomenon and its resolution. *SIAM review*, 39(4):644–668, 1997.

[27] S. Gottlieb. On high order strong stability preserving Runge–Kutta and multi step time discretizations. *Journal of Scientific Computing*, 25(1):105–128, 2005.

[28] S. Gottlieb and C.W. Shu. Total variation diminishing Runge-Kutta schemes. *Mathematics of Computation of the American Mathematical Society*, 67(221): 73–85, 1998.

[29] L.M. Harris, P.H. Lauritzen, and R. Mittal. A flux-form version of the conservative semi-Lagrangian multi-tracer transport scheme (CSLAM) on the cubed sphere grid. *Journal of Computational Physics*, 230(4):1215–1237, 2011.

[30] A. Harten. High resolution schemes for hyperbolic conservation laws. *Journal of computational physics*, 49(3):357–393, 1983.

[31] A. Harten, B. Engquist, S. Osher, and S.R. Chakravarthy. Uniformly high order accurate essentially non-oscillatory schemes, III. *Journal of computational physics*, 71(2):231–303, 1987.

[32] A.K. Henrick, T.D. Aslam, and J.M. Powers. Mapped weighted essentially non-oscillatory schemes: achieving optimal order near critical points. *Journal of Computational Physics*, 207(2):542–567, 2005.

[33] J.S. Hesthaven and T. Warburton. *Nodal discontinuous Galerkin methods: algorithms, analysis, and applications*. Springer-Verlag, New York, 2007.

[34] C.Q. Hu and C.W. Shu. Weighted essentially non-oscillatory schemes on triangular meshes. *Journal of Computational Physics*, 150(1):97–127, 1999.

[35] X.Y. Hu, B. Wang, and N.A. Adams. An efficient low-dissipation hybrid weighted essentially non-oscillatory scheme. *Journal of Computational Physics*, 301:415–424, 2015.

[36] C.S. Huang, F. Xiao, and T. Arbogast. Fifth order multi-moment WENO schemes for hyperbolic conservation laws. *Journal of Scientific Computing*, 64(2):477–507, 2015.

[37] H.T. Huynh. A flux reconstruction approach to high-order schemes including discontinuous Galerkin methods. *AIAA paper*, (4079), 2007.

[38] H.T. Huynh. A reconstruction approach to high-order schemes including discontinuous Galerkin for diffusion. *AIAA paper*, 403:2009, 2009.

[39] H.T. Huynh, Z.J. Wang, and P.E. Vincent. High-order methods for computational fluid dynamics: A brief review of compact differential formulations on unstructured grids. *Computers & Fluids*, 98:209–220, 2014.

[40] S. Ii and F. Xiao. CIP/multi-moment finite volume method for Euler equations: A semi-Lagrangian characteristic formulation. *Journal of Computational Physics*, 222(2):849–871, 2007.

[41] S. Ii and F. Xiao. High order multi-moment constrained finite volume method. Part I: Basic formulation. *Journal of Computational Physics*, 228(10):3669–3707, 2009.

[42] S. Ii, B. Xie, and F. Xiao. An interface capturing method with a continuous function: The THINC method on unstructured triangular and tetrahedral meshes. *Journal of Computational Physics*, 259:260–269, 2014.

[43] Y. Imai, T. Aoki, and K. Takizawa. Conservative form of interpolated differential operator scheme for compressible and incompressible fluid dynamics. *Journal of Computational Physics*, 227(4):2263–2285, 2008.

[44] G.S. Jiang and D.P. Peng. Weighted ENO schemes for Hamilton–Jacobi equations. *SIAM Journal on Scientific computing*, 21(6):2126–2143, 2000.

[45] G.S. Jiang and C.W. Shu. Efficient implementation of weighted ENO schemes. *Journal of computational physics*, 126(1):202–228, 1996.

[46] G.S. Jiang and C.C. Wu. A high-order WENO finite difference scheme for the equations of ideal magnetohydrodynamics. *Journal of Computational Physics*, 150(2):561–594, 1999.

[47] D.A. Kopriva and J.H. Kolias. A conservative Staggered-Grid Chebyshev multidomain method for compressible flow. Technical report, DTIC Document, 1995.

[48] P.H. Lauritzen, C. Jablonowski, M. Taylor, and R. Nair. Numerical techniques for global atmospheric models. 80:251–307, 2011.

[49] P.D. Lax. Weak solutions of nonlinear hyperbolic equations and their numerical computation. *Communications on pure and applied mathematics*, 7(1):159–193, 1954.

[50] X.L. Li, D.H. Chen, X.D. Peng, K. Takahashi, and F. Xiao. A multimoment finite-volume shallow-water model on the Yin-Yang overset spherical grid. *Monthly Weather Review*, 136(8):3066–3086, 2008.

[51] X.L. Li, C.G. Chen, X.S. Shen, and F. Xiao. A multimoment constrained finite-volume model for nonhydrostatic atmospheric dynamics. *Monthly Weather Review*, 141(4):1216–1240, 2013.

[52] S.J. Lin and R.B. Rood. Multidimensional flux-form semi-lagrangian transport schemes. *Monthly Weather Review*, 124(9):2046–2070, 1996.

[53] X.D. Liu, S. Osher, and T. Chan. Weighted essentially non-oscillatory schemes. *Journal of computational physics*, 115(1):200–212, 1994.

[54] X.L. Liu, S.H. Zhang, H.X. Zhang, and C.W. Shu. A new class of central compact schemes with spectral-like resolution II: Hybrid weighted nonlinear schemes. *Journal of Computational Physics*, 284:133–154, 2015.

[55] S.A. Moe, J.A. Rossmanith, and D.C. Seal. A simple and effective high-order shock-capturing limiter for discontinuous Galerkin methods. *arXiv preprint arXiv:1507.03024*, 2015.

[56] T. Nonomura, K. Kitamura, and K. Fujii. A simple interface sharpening technique with a hyperbolic tangent function applied to compressible two-fluid modeling. *Journal of Computational Physics*, 258:95–117, 2014.

[57] P.H. Oosthuizen and W.E. Carscallen. *Compressible fluid flow*. McGraw-Hill, 1997.

[58] A.T. Patera. A spectral element method for fluid dynamics: laminar flow in a channel expansion. *Journal of computational Physics*, 54(3):468–488, 1984.

[59] S. Pirozzoli. Conservative hybrid compact-WENO schemes for shock-turbulence interaction. *Journal of Computational Physics*, 178(1):81–117, 2002.

[60] J.M. Qiu and C.W. Shu. Positivity preserving semi-Lagrangian discontinuous Galerkin formulation: theoretical analysis and application to the Vlasov–Poisson system. *Journal of Computational Physics*, 230(23):8386–8409, 2011.

[61] J.X. Qiu and C.W. Shu. Hermite WENO schemes and their application as limiters for Runge–Kutta discontinuous Galerkin method: one-dimensional case. *Journal of Computational Physics*, 193(1):115–135, 2004.

[62] J.X. Qiu and C.W. Shu. A comparison of troubled-cell indicators for Runge-Kutta discontinuous Galerkin methods using weighted essentially nonoscillatory limiters. *SIAM Journal on Scientific Computing*, 27(3):995–1013, 2005.

[63] J.X. Qiu and C.W. Shu. Hermite WENO schemes and their application as limiters for Runge–Kutta discontinuous Galerkin method II: Two dimensional case. *Computers & Fluids*, 34(6):642–663, 2005.

[64] J.X. Qiu and C.W. Shu. Runge-Kutta discontinuous Galerkin method using WENO limiters. *SIAM Journal on Scientific Computing*, 26(3):907–929, 2005.

[65] W.H. Reed and T.R. Hill. Triangularmesh methodsfor the neutrontransportequation. *Los Alamos Report LA-UR-73-479*, 1973.

[66] Y.X. Ren, M.E. Liu, and H.X. Zhang. A characteristic-wise hybrid compact-weno scheme for solving hyperbolic conservation laws. *Journal of Computational Physics*, 192(2):365–386, 2003.

[67] P.L. Roe. Approximate riemann solvers, parameter vectors, and difference schemes. *Journal of computational physics*, 43(2):357–372, 1981.

[68] P.L. Roe. Characteristic-based schemes for the Euler equations. *Annual review of fluid mechanics*, 18(1):337–365, 1986.

[69] Y.Q. Shen and G.C. Zha. Improvement of weighted essentially non-oscillatory schemes near discontinuities. *Computers & Fluids*, 96:1–9, 2014.

[70] Y.Q. Shen, L. Liu, and Y. Yang. Multistep weighted essentially non-oscillatory scheme. *International Journal for Numerical Methods in Fluids*, 75(4):231–249, 2014.

[71] C.W. Shu. TVB uniformly high-order schemes for conservation laws. *Mathematics of Computation*, 49(179):105–121, 1987.

[72] C.W. Shu. High order weighted essentially nonoscillatory schemes for convection dominated problems. *SIAM review*, 51(1):82–126, 2009.

[73] C.W. Shu and S. Osher. Efficient implementation of essentially non-oscillatory shock-capturing schemes. *Journal of Computational Physics*, 77(2):439–471, 1988.

[74] C.W. Shu and S. Osher. Efficient implementation of essentially non-oscillatory shock-capturing schemes, II. *Upwind and High-Resolution Schemes*, 1:328–374, 1989.

[75] K.M. Shyue and F. Xiao. An Eulerian interface sharpening algorithm for compressible two-phase flow: The algebraic THINC approach. *Journal of Computational Physics*, 268:326–354, 2014.

[76] P.K. Smolarkiewicz and J.A. Pudykiewicz. A class of semi-Lagrangian approximations for fluids. *Journal of the Atmospheric Sciences*, 49(22):2082–2096, 1992.

[77] G.A. Sod. A survey of several finite difference methods for systems of nonlinear hyperbolic conservation laws. *Journal of computational physics*, 27(1):1–31, 1978.

[78] K. Spayd and M. Shearer. The Buckley–Leverett equation with dynamic capillary pressure. *SIAM Journal on Applied Mathematics*, 71(4):1088–1108, 2011.

[79] R.J. Spiteri and S. J. Ruuth. A new class of optimal high-order strong-stability-preserving time discretization methods. *SIAM Journal on Numerical Analysis*, 40(2):469–491, 2002.

[80] A. Staniforth and J. Côté. Semi-Lagrangian integration schemes for atmospheric models-a review. *Monthly weather review*, 119(9):2206–2223, 1991.

[81] P.K. Sweby. High resolution schemes using flux limiters for hyperbolic conservation laws. *SIAM journal on numerical analysis*, 21(5):995–1011, 1984.

[82] L.L. Takacs. A two-step scheme for the advection equation with minimized dissipation and dispersion errors. *Monthly Weather Review*, 113(6):1050–1065, 1985.

[83] R. Tanaka, T. Nakamura, and T. Yabe. Constructing exactly conservative scheme in a non-conservative form. *Computer physics communications*, 126(3):232–243, 2000.

[84] E.F. Toro. *Riemann solvers and numerical methods for fluid dynamics*. Springer-Verlag, Berlin, Third edition, 2009.

[85] E.F. Toro and V. A. Titarev. Derivative Riemann solvers for systems of conservation laws and ADER methods. *Journal of Computational Physics*, 212(1): 150–165, 2006.

[86] P.A. Ullrich and M.R. Norman. The Flux-Form Semi-Lagrangian Spectral Element (FF-SLSE) method for tracer transport. *Quarterly Journal of the Royal Meteorological Society*, 140(680):1069–1085, 2014.

[87] B. Van Leer. Towards the ultimate conservative difference scheme. IV. A new approach to numerical convection. *Journal of computational physics*, 23(3):276–299, 1977.

[88] B. Van Leer. Towards the ultimate conservative difference scheme. V. A second-order sequel to Godunov's method. *Journal of computational Physics*, 32(1): 101–136, 1979.

[89] Z.J. Wang. Spectral (finite) volume method for conservation laws on unstructured grids. basic formulation: Basic formulation. *Journal of Computational Physics*, 178(1):210–251, 2002.

[90] Z.J. Wang. High-order methods for the Euler and Navier–Stokes equations on unstructured grids. *Progress in Aerospace Sciences*, 43(1):1–41, 2007.

[91] Z.J. Wang and H.Y. Gao. A unifying lifting collocation penalty formulation including the discontinuous Galerkin, spectral volume/difference methods for conservation laws on mixed grids. *Journal of Computational Physics*, 228(21):8161–8186, 2009.

[92] Z.J. Wang and Y. Liu. Spectral (finite) volume method for conservation laws on unstructured grids: II. Extension to two-dimensional scalar equation. *Journal of Computational Physics*, 179(2):665–697, 2002.

[93] Z.J. Wang and Y. Liu. Spectral (finite) volume method for conservation laws on unstructured grids III: One dimensional systems and partition optimization. *Journal of Scientific Computing*, 20(1):137–157, 2004.

[94] P. Woodward and P. Colella. The numerical simulation of two-dimensional fluid flow with strong shocks. *Journal of Computational Physics*, 54(1):115–173, 1984.

[95] F. Xiao and A. Ikebata. An efficient method for capturing free boundaries in multi-fluid simulations. *International journal for numerical methods in fluids*, 42(2):187–210, 2003.

[96] F. Xiao and T. Yabe. Completely conservative and oscillationless semi-Lagrangian schemes for advection transportation. *Journal of computational physics*, 170(2):498–522, 2001.

[97] F. Xiao, T. Yabe, and T. Ito. Constructing oscillation preventing scheme for advection equation by rational function. *Computer Physics Communications*, 93 (1):1–12, 1996.

[98] F. Xiao, T. Yabe, G. Nizam, and T. Ito. Constructing a multi-dimensional oscillation preventing scheme for the advection equation by a rational function. *Computer Physics Communications*, 94(2):103–118, 1996.

[99] F. Xiao, T. Yabe, X. Peng, and H. Kobayashi. Conservative and oscillation-less atmospheric transport schemes based on rational functions. *Journal of Geophysical Research: Atmospheres*, 107(D22), 2002.

[100] F. Xiao, Y. Honma, and T/ Kono. A simple algebraic interface capturing scheme using hyperbolic tangent function. *International Journal for Numerical Methods in Fluids*, 48(9):1023–1040, 2005.

[101] F. Xiao, S. Ii, and C.G. Chen. Revisit to the THINC scheme: a simple algebraic VOF algorithm. *Journal of Computational Physics*, 230(19):7086–7092, 2011.

[102] F. Xiao, S. Ii, C.G. Chen, and X.L. Li. A note on the general multi-moment constrained flux reconstruction formulation for high order schemes. *Applied Mathematical Modelling*, 37(7):5092–5108, 2013.

[103] B. Xie and F. Xiao. Two and three dimensional multi-moment finite volume solver for incompressible Navier–Stokes equations on unstructured grids with arbitrary quadrilateral and hexahedral elements. *Computers & Fluids*, 104:40–54, 2014.

[104] B. Xie, S. Ii, A. Ikebata, and F. Xiao. A multi-moment finite volume method for incompressible Navier–Stokes equations on unstructured grids: Volume-average/point-value formulation. *Journal of Computational Physics*, 277:138–162, 2014.

[105] B. Xie, X. Deng, Z.Y. Sun, and F. Xiao. A hybrid pressure-density-based Mach uniform algorithm for 2D Euler equations on unstructured grids by using multi-moment finite volume method. *Journal of Computational Physics*, 2017.

[106] T. Yabe and T. Aoki. A universal solver for hyperbolic equations by cubic-polynomial interpolation I. One-dimensional solver. *Computer Physics Communications*, 66(2):219–232, 1991.

[107] T. Yabe, R. Tanaka, T. Nakamura, and F. Xiao. An exactly conservative semi-Lagrangian scheme (CIP-CSL) in one dimension. *Monthly weather review*, 129 (2):332–344, 2001.

[108] T. Yabe, F. Xiao, and T. Utsumi. The constrained interpolation profile method for multiphase analysis. *Journal of Computational Physics*, 169(2):556–593, 2001.

[109] H.C. Yee, N.D. Sandham, and M.J. Djomehri. Low-dissipative high-order shock-capturing methods using characteristic-based filters. *Journal of Computational Physics*, 150(1):199–238, 1999.

[110] K. Yokoi. Efficient implementation of THINC scheme: a simple and practical smoothed VOF algorithm. *Journal of Computational Physics*, 226(2):1985–2002, 2007.

[111] S.T. Zalesak. Fully multidimensional flux-corrected transport algorithms for fluids. *Journal of computational physics*, 31(3):335–362, 1979.

[112] X.H. Zhong and C.W. Shu. A simple weighted essentially nonoscillatory limiter for Runge–Kutta discontinuous Galerkin methods. *Journal of Computational Physics*, 232(1):397–415, 2013.